XVI Fluid Dynamics of Floating Particles

This chapter takes up a new problem for direct numerical simulation which includes the topics of fluid dynamics of heavier-than-liquid floating particles driven to self-assembled aggregates by capillary forces. This is a problem of three-phase flow; liquid/gas/solid. The material in this chapter is taken from the two papers listed below. Prior literature is found locally at the end of the two subsections corresponding to the two papers.

D.D. Joseph, J. Wang, R. Bai, and B.H. Yang, 2003. Particle motion in a liquid film rimming the inside of a partially filled rotating cylinder. *J. Fluid. Mech.*, **496**, 139-163.

P. Singh and D.D. Joseph, 2005. Fluid dynamics of floating particles. *J. Fluid Mech.*, accepted for publication.

• Self-aggregation, clustering and bonding of particles in a liquid film rimming the inside of a partially filled rotating cylinder

Abstract

Both lighter- and hydrophobic heavier-than-liquid particles will float on liquid-air surfaces. Capillary forces cause the particles to cluster in typical situations identified here. This kind of clustering causes particles to segregate into islands and bands of high concentrations in thin liquid films rimming the inside of a slowly rotating cylinder partially filled with liquid. A second regime of particle segregation, driven by secondary motions induced by off-center gas bubbles in a more rapidly rotating cylinder at higher filling levels, is identified. A third regime of segregation of bi-disperse suspensions is found in which two layers of heavier-than-liquid particles that stratify when there is no rotation, segregate into alternate bands of particles when there is rotation[*].

I. Capillary forces

The deformation of the air-liquid interface due to floating light particles or due to trapped heavy small particles gives rise to capillary forces on the particles. These forces may be

---

[*] Movies of the experiments reported in this paper can be viewed at the web address *http://www.aem.umn.edu/research/particles/rtcylinderpaper/* .

qualitatively understood from simple arguments. Two kinds of forces act on particles: forces due to gravity and forces due to the action of contact angles. These two kinds of forces are at play in the vertical force balance but require a somewhat more elaborate explanation for horizontal force balance. The effects of gravity are usually paramount for heavier-than-liquid floating particles in which one particle will fall into the depression of the second. A heavier-than-liquid particle will fall down a downward sloping meniscus while an upward buoyant particle will rise. Capillary forces cause particles to cluster, as shown in figure 4.

In this section, we shall review the nature of capillary forces which cause the particles to cluster; in section II we show how these forces produce islands and bands of segregated particles in a thin liquid film rimming the inside of a slowly rotating cylinder.

I-1. Vertical forces

The simplest analysis relevant to understanding the forces on small particles is the vertical force balance on a sphere floating on the interface between fluids which, for convenience, is here called water and air. This analysis was given first by Princen (1969), then by Rapacchietta and Neumann (1977) and by Kotah, Fujita and Imazu (1992), who used the floating ball to measure contact angles.

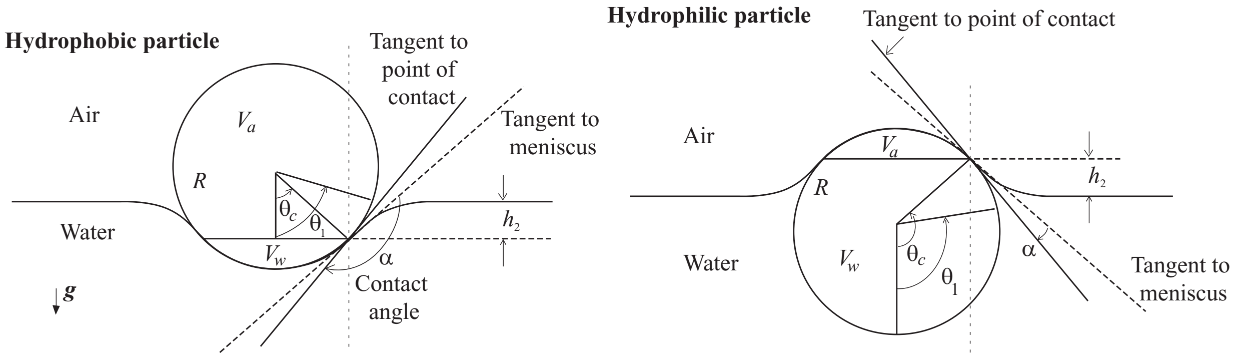

Figure 1. Hydrophobic and hydrophilic particles at equilibrium.

The capillary force F_c, is a function of the radius of particle R, the surface tension coefficient γ, the filling angle (position of the contact ring) θ_c and the contact angle α (see figure 1), given by,

$$F_c = 2\pi(R\sin\theta_c)\gamma\sin[\theta_c-(\pi-\alpha)] = -2\pi R\gamma\sin\theta_c\sin(\theta_c+\alpha) \qquad (1)$$

for both the hydrophobic and hydrophilic cases.

To have mechanical equilibrium, the capillary force plus the vertical resultant of pressure around the sphere must balance the gravity vertical component,

$$F_c + F_p = G \tag{2}$$

where $G = \frac{4}{3}\rho_p \pi R^3 g$ is the weight of the particle, and the vertical resultant of pressure around the sphere can be written as

$$F_p = \rho_l g V_w + \rho_a g(V - V_w) - (\rho_l - \rho_a) g h_2 A\,. \tag{3}$$

where ρ_l and ρ_a are densities of the liquid and the air, respectively; h_2 is the depression generated by the particle, with positive value in the case shown in figure 1(a) and negative value shown in figure 1(b); $V = \frac{4}{3}\pi R^3$ is the volume of the sphere, $V_w = \pi R^3\left(\frac{2}{3} - \cos\theta_c + \frac{1}{3}\cos^3\theta_c\right)$ is the volume of the sphere immersed in the water and $A = \pi(R\sin\theta_c)^2$ is the area of the ring of contact. The first two terms at the right hand side of (3) are in agreement with Archimedes' principle, while the last term accounts for the meniscus effect. When a meniscus is present, the buoyancy calculated by Archimedes' principle $\rho_l g V_w + \rho_a g(V - V_w)$ not only lifts the sphere, but also the fluid in the meniscus.

Inserting (1) and (3) into (2), we get the vertical force balance,

$$\sin\theta_c \sin(\theta_c + \alpha) = -\frac{B}{2}\left[\begin{array}{l} \frac{4}{3}\psi_1 - \left(\frac{2}{3} - \cos\theta_c + \frac{1}{3}\cos^3\theta_c\right) - \psi_2\left(\frac{2}{3} + \cos\theta_c - \frac{1}{3}\cos^3\theta_c\right) \\ + (1 - \psi_2)(\cos\theta_c - \cos\theta_1)\sin^2\theta_c \end{array}\right] \tag{4}$$

where $\cos\theta_c - \cos\theta_1 = h_2/R$□□□ θ_1 is measured from the point of extension of the flat meniscus as indicated in figure 1. $B = \rho_l R^2 g/\gamma$ is the bond number and $\psi_1 = \rho_p/\rho_l$ and $\psi_2 = \rho_a/\rho_l$ are the dimensionless control parameters.

It can be inferred from (4) that the left side of the equation, consequently, the right side, lies in the range $-1 \le \sin\theta_C \sin(\theta_C + \alpha) \le 1$. Obviously this equation cannot be solved if the particles are too large or too heavy. However, it can be concluded that small hydrophobic particles can always be suspended in fluid surfaces no matter how heavy they may be, as long as $\rho_p R^2 g/\gamma$ is small enough. Moreover, in the limit of $\rho_p R^2 g/\gamma \to 0$, $\sin\theta_c \sin(\alpha + \theta_c) = 0$ and the particles sit on the top of the fluid or are held in place by capillarity.

If the particle is irregular with sharp corners the capillarity argument fails. Liquid-air surfaces bind at razor sharp corners; the physics associated with this strong bond are not understood. Razor blades and straight pins can float on water-air surfaces pinned at the sharp surface.

Equation (4) suggests that hydrophobic nanoparticles can float on the surface no matter how heavy they are. However, even though the formula does not predict that hydrophilic particles will sink, they will sink because of a not-understood wetting instability. If heavy nanoparticles are put into the liquid, they will not rise. The surface layer on a liquid which gives rise to surface tension is very small, but not zero; likewise, the concept of contact angles on nanoparticles may lose meaning.

I-2. Horizontal forces

The deformation of a liquid-fluid interface due to trapped small particles gives rise to lateral capillary forces exerted on the particle. A simple explanation is shown in figure 2. For a heavier-than-liquid particle, the meniscus is below the undisturbed level. The particles will tilt causing an imbalance of the horizontal component of capillary forces pulling the spheres together. Lighter-than-water hydrophilic particles will rise into the elevated section of the meniscus and come together.

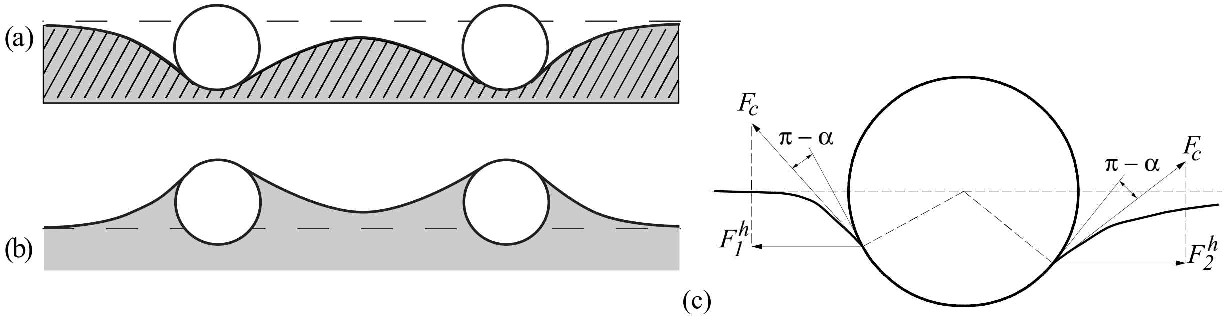

Figure 2. Spherical particles in water, (a) heavier-than-water hydrophobic particles. (b) Lighter-than-water hydrophilic particles. (c) If for any reason, the particle tilts with the two contact angles equal, a horizontal force imbalance will result. In the figure, the vector Fc indicates the magnitude of the capillary force and F_1^h *and* F_2^h *are horizontal components,* $F_2^h > F_1^h$.

There are several ways to isolate the effects of capillarity uninfluenced by gravity. Poynting and Thompson (1913) investigated the capillary effect by considering two vertical plates immersed in a liquid, the space between the plates is a two dimensional capillary tube. If the plates are hydrophobic, the level in the capillary gap sinks below the liquid outside; if the plates are hydrophilic the levels will rise. Their argument about the nature of horizontal forces on the plates is given in the caption of figure 3. Repulsion between plates with different wetting properties is rather short range because it stops when the meniscus between plates gets flat.

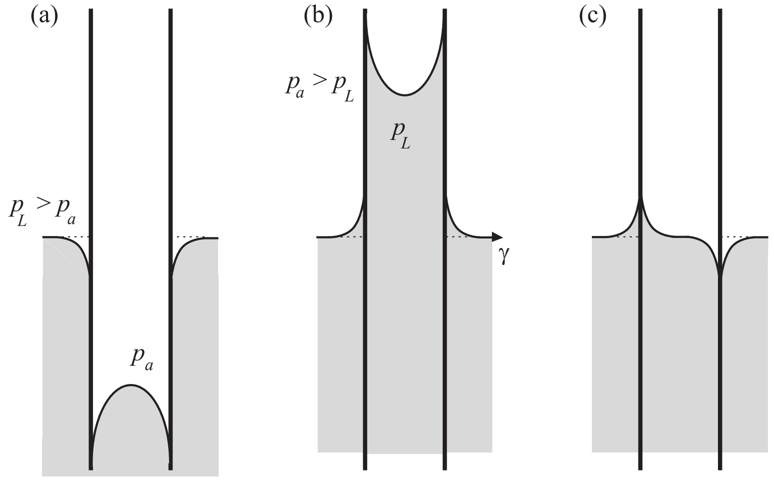

Figure 3. (After Poynting and Thompson 1913). Horizontal forces associated with the fall (a) of liquid between hydrophobic plates and the rise (b) of liquid between hydrophilic plates. In (c) one plate is hydrophilic and the other hydrophobic. The contacts on both sides of a plate are the same and the tension γ *is constant. They argue that the net horizontal force due to* γ *can be calculated at flat places; so that there is no net horizontal component of the tension. In (a) and (b) the pressures are such that they push the plates together; there is no net attractive force in (c). If the plates (c) are so close that there is no flat place, then the horizontal projection* $\gamma \sin \alpha$ *of the interface midway between the plates is smaller than the horizontal component outside the plates and the plates are pulled apart; they repel. They note that "…small bodies, such as straw or pieces of cork, floating on the surface of a liquid often attract each other in clusters; this occurs when the bodies are all wet by the liquid and also when none of them is wet; if one body is wet and one is not wet, they repel each other." (It may help here to note that if one face of the plate is hydrophobic and the other hydrophilic, the contact angles will put the plates in tension, tending to pull them apart.)*

Another way to take away the effects of gravity is to support the particles on a substrate. In this case the horizontal forces are due to capillary effects alone. Katoh, Fujita and Imazu (1992) studied the motion of a particle floating on a liquid meniscus which could be interpreted as motion on a substrate because the foaming phlystyrol particles used by them are an order of magnitude lighter than water, and minimize the effects of gravity compared to capillarity. Their experimental results are completely consistent with the predictions of Poynting and Thompson (1913): when the sphere and the wall are alike with respect to wetting; say both are hydrophobic or hydrophilic, the wall and sphere attracts; when they are unlike the sphere and wall repel.

Despite the well-established importance of the capillary meniscus forces there are only a few theoretical works devoted to them. Nicolson (1949) was the first to derive an analytical expression for the capillary force between two floating bubbles by using the superposition of approximation to solve the Laplace equation of capillarity. A similar approximate method was applied by Chan, Henry and White (1981) to floating spheres and horizontal cylinders. For horizontal cylinders the alternative approaches were proposed by Gifford and Scriven (1971) and by Fortes (1982). The theoretical works are based on solutions of the Laplace equations for capillary menisci of translational or rotational symmetry, where the Laplace equation reduces to an ordinary differential equation.

An analytical solution of the Laplace partial differential equation in bipolar coordinates was proposed by Kralchevsky, Paunov, Ivanov and Nagayama (1992), and Kralchevsky, Paunov, Denkov, Ivanov and Nagayama (1993) for the case of small particles and small meniscus slope. This solution provides expressions for calculating the capillary meniscus force between two vertical cylinders, between two spheres partially immersed in a liquid layer and between a vertical cylinder and a sphere. A review is recently presented by Kralchevsky and K. Nagayama (2000).

Their theory (see Kralchevsky and Nagayama, 2000), which has been validated in experiments, provides the following asymptotic expression for calculating the lateral capillary force between two particles of radii R_1 and R_2 separated by a center-to-center distance L,

$$F = -2\pi\gamma Q_1 Q_2\, qK_1(qL)\left[1 + O\left(q^2R_k^2\right)\right] \text{ when } L >> r_k \tag{5}$$

where $r_k = R_k \sin\theta_c$ (k=1 and 2) are the radii of the two contact lines (see figure 1);

$$Q_k = r_k \sin\psi_k \quad (k = 1 \text{ and } 2) \tag{6}$$

with ψ_k being the meniscus slope angles with respected to the horizontal plane at the contact point ($\psi > 0$ for floating light particles, and $\psi < 0$ for heavy particles);

$$q = \sqrt{(\rho_l - \rho_a)g/\gamma} \qquad (7)_1$$

is the inverse of the capillary length; in addition $K_1(x)$ is the modified Bessel function of the first order. Therefore, the lateral capillary force between two identical particles is

$$F = -2\pi\gamma Q_1 Q_2/L, \qquad (7)_2$$

when the distance between them is much smaller than the capillary length ($q^{-1} = 2.7mm$ for water-air interface).

I-3. Particle clustering

Due to the attractive lateral capillary forces between similar particles floating on a liquid surface, particles tend to cluster. The dynamic behavior of clustering is not well characterized. Gifford and Scriven (1971) noted that “casual observations… show that floating needles and many other sorts of particles do indeed come together with astonishing acceleration. The unsteady flow fields that are generated challenge analysis by both experiment and theory. They will have to be understood before the common-place ‘capillary attraction’ can be more than a mere label, so far as dynamic processes are concerned.”

There are a small number of theoretical studies of the drag and diffusion coefficient of a spherical particle attached to a fluid interface (Brenner and Leal 1978, 1982; Goldman, Cox and Brenner 1967; Schneider, O’Neill and Brenner 1973; Majumdar, O’Neill and Brenner 1974—which may be collectively designated as Brenner *et al*—and Wakiya 1957; Redoev, Nedjalkov and Djakovich 1992; Danov, Aust, Durst and Lange 1995). A recent study of Saif (2002) develops a theory of capillary interactions between solid plates forming menisci on the surface of a liquid.

The only experimental determination of drag coefficients for particles of any size were performed by Petkov, Denkov, Danov, Velev, Aust and Durst (1995) for particles of sub-millimeter radius by measuring the particle velocity under the action of well defined external force. They showed that the capillary interactions are quite strong and very long range. Accelerations, which are very great under many conditions of interest, have not been studied before.

We found that the initially randomly distributed particles floating on a liquid surface tend to cluster due to the attractive lateral capillary forces between the particles. It is generally observed that the particles initially form small clusters, then the small clusters slowly merge into bigger ones; and eventually the bigger ones are assembled into a giant cluster. This self-assembly process is shown in the pictures of figure 4. The procedure by which we obtain dispersions like those shown at 3 min in figure 4 is noteworthy. We create such dispersions by pouring particles on the liquid, nothing complicated, just like a salt shaker. As soon as the particles hit the liquid surface they disperse rapidly leading to dispersions like that at 3 min in figure 4. The dispersions then attract. This initial repulsion, followed by attraction, is more or less universal and we have not seen it mentioned in the literature.

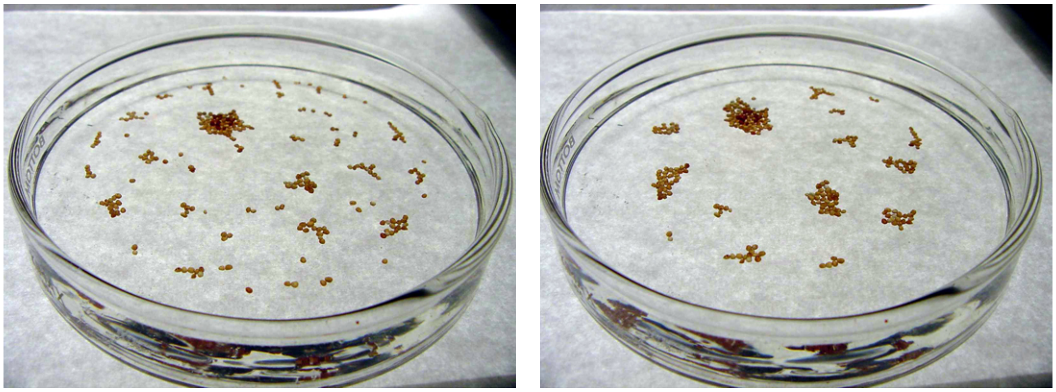

Elapsed time: 3 minutes

10 minutes

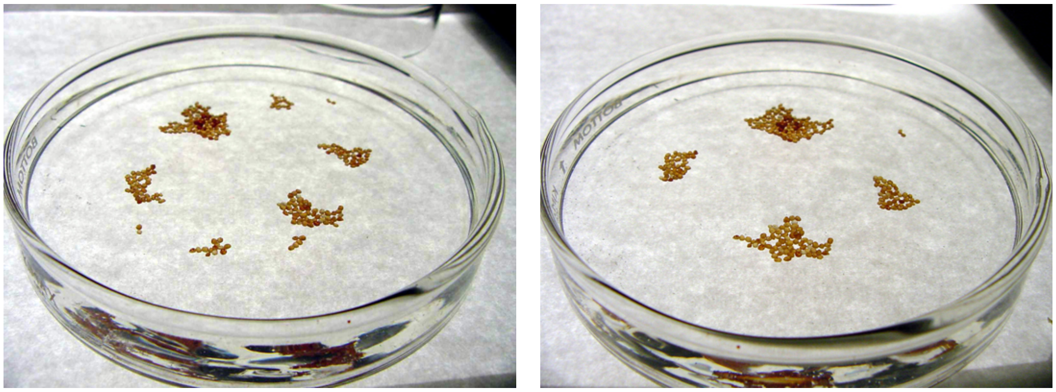

30 minutes

2 hours

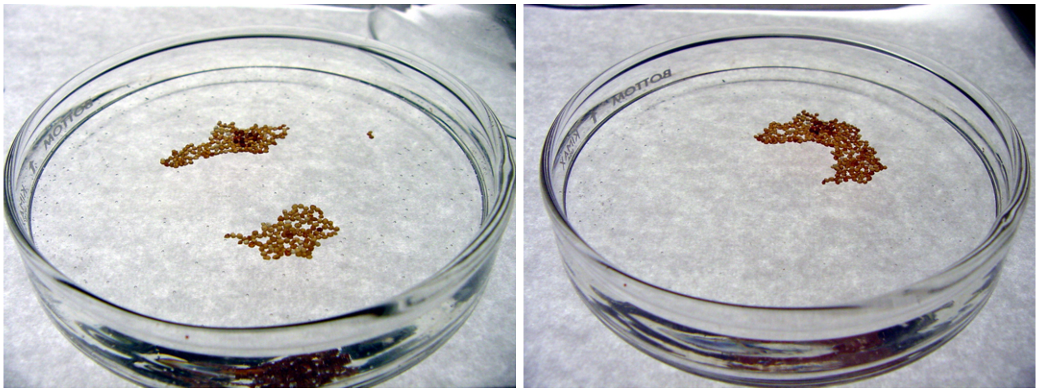

12 hours

24 hours

Figure 4. Free motions leading to self-assembly of floating particles (sands in 1% aqueous polyox solution).

Experiments on particle clustering due to capillarity were carried out in glass petrie dishes with diameters ranging from 5 to 15 cm. Three different liquids (table 1) and two different hydrophobic particles (table 2) were used. Hydrophobic particles did not collect on the glass side-walls of the petri dishes so that end effects arising from walls in dishes of different sizes were not important.

Type of liquid	**Glycerin**	**Soybean oil**	**Triton mixture**
Density ρ (g/cm^3)	1.173	0.915	1.241
Viscosity μ (cp)	1490	282	2950
Surface Tension (mN/m) (measured with a spinning-drop tensiometer)	41.46	24.28	33.15

Table 1. Physical parameters for liquids.

Type of particle	**Polymer particle**	**Nylon particle**
Density ρ (g/cm^3)	1.034	1.170
Diameter d_p (cm)	0.065	0.314

Table 2. Physical parameters for particles.

Clustering, of the type shown in figure 4, was observed for both types of the particles in glycerin and in the Triton-water mixture. These particles could not be suspended in soybean oil, because they were too heavy. However, they could be held by capillarity in the hanging film shown in figure 7.

Rate of approach experiments were conducted for two identical particles attracted by capillary forces on the Glycerin-air and Triton mixture-air interface. The distance between the two particles was measured with a video camera as a function of time until they touch, as shown in figures 5 and 6. In general, the approaching of the particles takes hours, agreeing with the time for cluster formation. The curves are not similar near the time of final approach. The approach velocity depends strongly on liquid properties. Particles in a 6000 cp Triton mixture barely move even when they are placed very close together. On the other hand, the rate of approach of hydrophobic particles on water-air surfaces is surprisingly fast in the final times. The estimated final approaching velocities are $0.2\,\mu m/s$ and $0.025\,mm/s$ for the data shown in figures 5 and 6, respectively. The approach velocity is smaller for the smaller particles, but the data was erratic and quantitative results were not obtained.

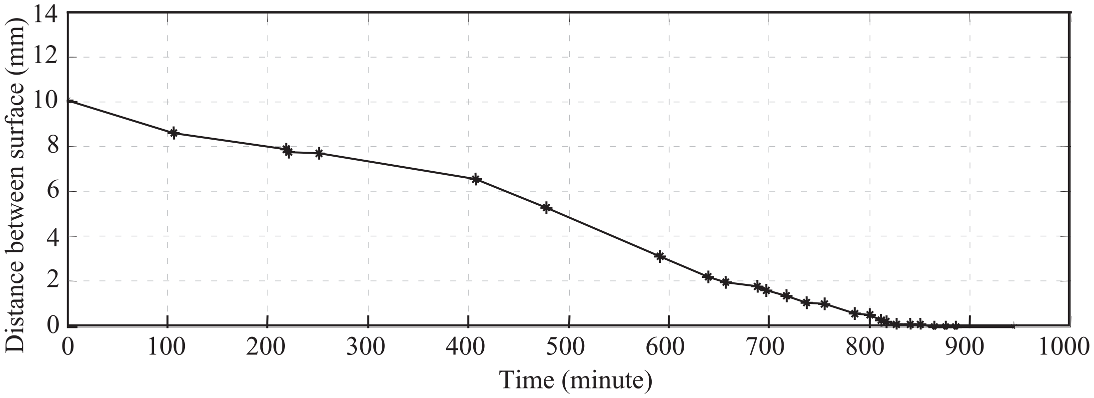

Figure 5. Distance between the two identical particles. Triton mixture (2950 cp) and nylon particles were used.

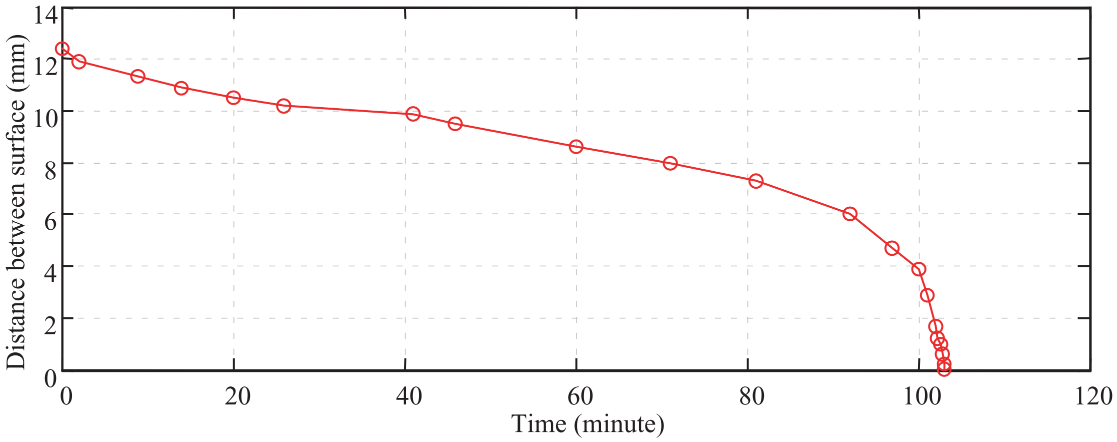

Figure 6. Distance between the two identical particles. Glycerin and nylon particles were used.

The photograph in figure 7 shows the aggregation of polymer particles in a hanging glycerin film on the bottom of a flat glass plate taken from the top of the plate. The particles are encapsulated by glycerin and drawn together in hanging drops of glycerin robustly stable for months. This hanging drop configuration is shown in figure 9 as a cartoon in side view.

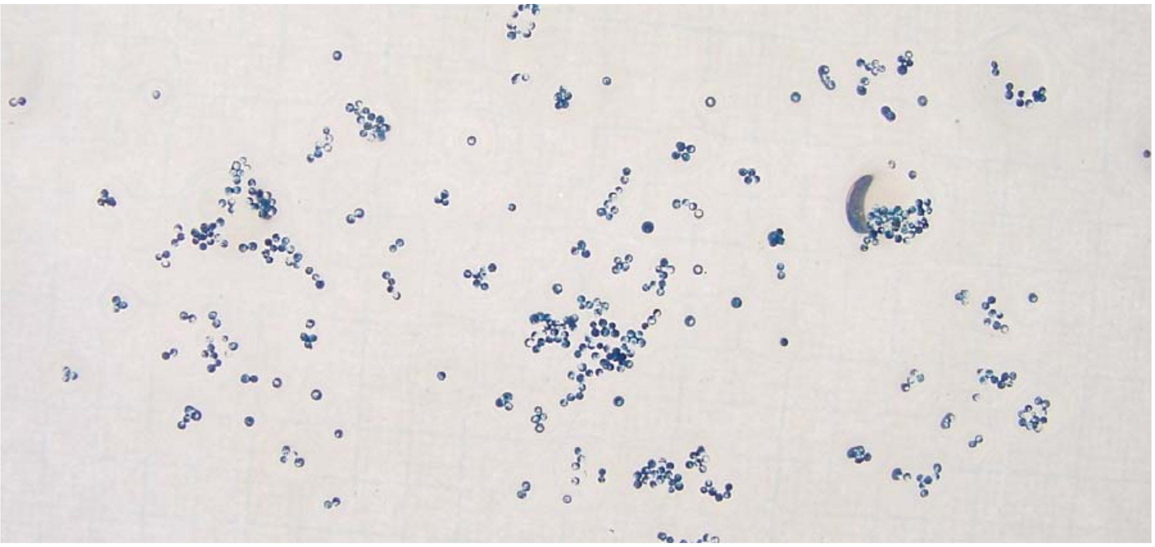

Figure 7. Aggregates of polymer particles in glycerin drops hanging from the bottom of a glass plate.

The ability of self-assembly of particles under the action of lateral capillary forces has been used by Bowden *et al*. (1997, 1999) and Grzybowski *et al.* (2001). They assembled topologically complex mesoscale (from millimeter to micrometer size) objects into ordered two-dimensional arrays by floating the objects at the interface between perfluorodecalin (hydrophobic) and water. The structure of the arrays was manipulated by the design of the shape of the assembling objects and wettability of their surfaces. They modeled the self-assembly process as the minimization of the total interfacial free energy (the sum of the capillary energy and the gravitational energy) of the liquid-liquid interface.

II. Particle aggregation in a liquid film rimming a rotating cylinder

Tirumkudulu, Tripathi and Acrivos (1999) first reported particle segregation in a suspension of monodispersed neutrally buoyant spheres in a Newtonian liquid medium being sheared in a partially filled horizontal Couette device. They found that the suspension separates itself into alternating regions of high and low particle concentration along the length of the tube. In a following study, Tirumkudulu, Mileo and Acrivos (2000) (hereafter denoted as TMA 2000) observed that under certain circumstances particles which are initially uniformly mixed in a film rimming a horizontal rotating cylinder will also be drawn into cylindrical bands of high particle concentration separated by regions of pure liquid. They did not offer a quantitative explanation of this phenomenon but suggested that the cause might be found in changes of the effective viscosity of the suspension induced by fluctuations of concentration. A theory relying on the shear induced diffusion of particles, concentration-dependent viscosity and the existence of a free surface was developed by Govindarajan, Nott and Ramaswamy (2001) to provide an explanation of the above mentioned experiments. However, quantitative comparison with the experimental data was not provided. A latest experimental result was reported by Timberlake and Morris (2002) in which concentration band dynamics was studied using a partially filled Couette device. They showed that the particle migration process observed in experiments was much faster than that predicated by the shear induced diffusion theory, about 40 times faster in one case examined, suggested strong evidence against shear-induced diffusion as the mechanism responsible for the observed segregation.

We carried out similar experiments and identified two regimes in which particles segregate; a low-speed, low-Reynolds number regime, in which particles are segregated at thin places on the rimming film by lateral capillary forces, and a high-speed regime associated with the formation of bubbles (Balmer 1970, Karweit and Corrsin 1975, Preziosi and Joseph 1988 among others). The segregation at low Reynolds numbers occurs in the parameter ranges similar to those studied by TMA 2000. The high-speed segregation has not been noted before.

II-1. The ratio of the minimum film thickness to the particle diameter

The segregation of particles due to capillarity occurs in the thin part of the film rimming the rotating cylinder near the top of the cylinder. The critical parameter for this appears to be the ratio D_{min}/d_p, where D_{min} is the minimum film thickness which is near the top of the cylinder to the side in which the gravity and the vertical component of rotation point downward (figure 8).

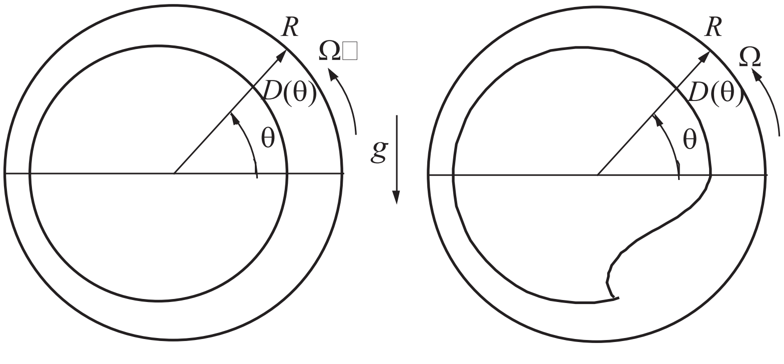

Figure 8. Film profile in rimming flow inside a rotating cylinder. (a) For small β. (b) For β larger than a critical value ($\beta_c = 1.414$*).*

We find that D_{min}/d_p is $O(1)$ and the rotational speed of the cylinder must be slow enough relative to the speed of capillary attraction to allow clusters to form more rapidly than they disperse in the pool of liquid at the bottom of the rotating cylinder. TMA (2000) identified the relevant rotation parameter

$$\beta = F\sqrt{\frac{gR}{\nu\Omega}} \tag{8}$$

where F is the fill ratio, i.e., the ratio of the total volume of liquid inside the cylinder to the volume of the cylinder; R is the radius of the cylinder; Ω is its angular rotational speed; ν is the kinetic viscosity of the liquid; g is the gravitational acceleration. The parameter β is the only dimensionless parameter to arise in lubrication theory; its relation to the filling parameter F is subtle and needs clarification. When $\beta < \beta_c = 1.4142$, a smooth film exists inside the rotating cylinder. However, when β is increased beyond the critical value β_c, smooth solution of the lubrication equations does not exist, and a bump is formed near the bottom of the cylinder where the film thickness varies rapidly, as is shown in figure 8 and in figures 1 and 3 of TMA (2000). Lubrication theory can be used to compute D_{min} when $\beta < \beta_c$; it can also be used to compute the minimum film thickness in the region above the pool of liquid when $\beta > \beta_c$ by a procedure which will be discussed below, but the solution is not uniformly around the cylinder in the pool below. The critical condition for the existence of a smooth solution of the lubrication equation for a thin film on the exterior of a rotating rod was called the "run-off" condition by Preziosi and Joseph (1988) and the critical condition for rimming flow was called a "run-on" condition. The run-off and run-on conditions were verified in experiment reported by Preziosi and Joseph (1988).

Many authors have published analyses of lubrication flows of liquids running inside of a rotating cylinder: Diebler and Cerro (1970), Moffatt (1977), Preziosi and Joseph (1988), Johnson (1988), O'Brien and Gath (1998) and Tirumkudulu and Acrivos (2001).

The segregation of particles by capillary forces does not correlate with β but the ratio D_{min}/d_p is important and lubrication theory can be used to compute D_{min} by the method described below. The physical parameters are the cylinder radius R, the kinematic viscosity of the fluid ν, the angular speed of rotation Ω, the volume fraction of the fluid F, the acceleration of gravity g, the liquid flux Q, and the thickness of the film D. Preziosi & Joseph (1988) obtained the following equation for D using a lubrication theory:

$$Q = \Omega R D - \frac{g}{\nu}\frac{1}{3}D^3\cos\theta = \Omega R D_0 - \frac{g}{\nu}\frac{1}{3}D_0^3 \tag{9}$$

where D_0 is the film thickness at $\theta = 0$. Let $h = D/R$ and $S = gR/\nu\Omega$, (9) can be written in the following non-dimensional form:

$$\frac{Q}{\Omega R^2} = h - \frac{1}{3} S h^3 \cos\theta = h_0 - \frac{1}{3} S h_0^3 \tag{10}$$

where h_o is the maximum film thickness; $h_o = h(\theta)$ at $\theta = 0$ (see figure 8). Preziosi & Joseph gave the condition under which equation (10) is solvable,

$$h_0^2 S < 1 . \tag{11}$$

Expression (11) is also the critical criterion of run-on.

O'Brien and Gath (1998) defined $\eta = D\left(\frac{g}{\Omega R \nu}\right)^{1/2} = \frac{D}{R} S^{1/2}$ and $q = Q\left(\frac{g}{\Omega^3 R^3 \nu}\right)^{1/2} = \frac{Q}{\Omega R^2} S^{1/2}$. Under such definitions, (10) becomes:

$$q = \eta - \frac{1}{3}\eta^3 \cos\theta = \eta_0 - \frac{1}{3}\eta_0^3 \tag{12}$$

O'Brien and Gath gave the condition under which equation (12) is solvable:

$$0 < q < 2/3 \tag{13}$$

Note that when $q = 2/3$, the solution of (12) is $\eta_0 = h_0 S^{1/2} = 1$. Hence, the run-on criterion (11) is equivalent to (13).

The fluid fraction F can be computed by integrating $D(\theta)$:

$$F = \frac{1}{\pi R}\int_{-\pi}^{\pi} D(\theta) d\theta \equiv \frac{\beta}{S^{1/2}}, \text{ where } \beta = \frac{1}{\pi}\int_{-\pi}^{\pi} \eta(\theta) d\theta . \tag{14}$$

By virtue of (12) and (14), the value of β corresponding to $q = 2/3$ is $\beta = 1.4142$.

Therefore, the three run-on conditions are equivalent: $h_0^2 S < 1$, $0 < q < 2/3$, and $\beta < 1.4142$.

When $\beta < 1.4142$, all the fluid join the circulation. The fluid flux is obtained from F,

$$\frac{Q}{\Omega R^2} = \frac{F}{2} . \tag{15}$$

Hence, equation (10) can be solved for the film profile, $h(\theta)$,

$$h - \tfrac{1}{3} S h^3 \cos\theta = \tfrac{1}{2} F , \tag{16}$$

and the minimum film thickness can be obtained from $\theta = \pi$.

The maximum film thickness h_o at $\theta = 0$ is an increasing function of β with a maximum at $\beta = \beta_c$. When $\beta > \beta_c = 1.4142$, there are places on the cylinder where the thickness of the layer is larger than the critical value, and the excess fluid will collect under the bump. However, it may be assumed that h_o remains at $\theta = 0$ (see figure 8); it is the maximum thickness of the film above the bump. This assumption could not be strictly correct; Ruschak and Scriven (1976) showed that under a perturbation of the thin film condition used to justify lubrication theory the position of the maximum thickness rotates into the first quadrant. We assume that the maximum film thickness that can be maintained by rotation is determined by the critical run-on condition (11), $h_0 = 1/\sqrt{S} = \sqrt{\nu\Omega/gR}$. Therefore, we can calculate the actual fluid flux in the circulation by

$$\frac{Q}{\Omega R^2} = h_0 - \frac{S}{3}h_0^3 = \frac{2}{3\sqrt{S}}. \tag{17}$$

Then the minimum film thickness at $\theta = \pi$ is determined from the volume conservation (10),

$$\frac{Q}{\Omega R^2} = h_{\min} + \frac{S}{3}h_{\min}^3 = \frac{2}{3\sqrt{S}}$$

or,

$$h_{\min} = \frac{0.596}{\sqrt{S}} = 0.596\sqrt{\frac{\nu\Omega}{gR}}\ . \tag{18}$$

Tirumkudulu & Acrivos (2001) solved the film profile using lubrication analysis and numerical computation from the full Stokes equations, and compared their solutions with experimental measurements. They found that $\eta_{\min} = h_{\min}\sqrt{\frac{gR}{\nu\Omega}} = 0.6$, (in their Figure 5), which agrees perfectly with our expression (18) based on a much simpler argument. Therefore, when β is greater than β_c, the minimum film thickness D_{min} listed in table 3 are evaluated from (18). Corresponding to a specified filling level F, we may also determine the average film thickness D_a from

$$F = \frac{R^2 - (R - Da)^2}{R^2}\text{ , that is, } D_a = \left(1 - \sqrt{1 - F}\right)R\ . \tag{19}$$

II-2. Particle segregation in aqueous Triton mixtures

TMA 2000 found particle segregation in monodispersed sheared suspensions in a partially filled rotating horizontal cylinder when the filling fractions (liquid volume/total volume) were small $0.1 \le F \le 0.15$. The particle concentrations for the uniform mixtures were 5% and 15%. The values of β in experiments reported in TMA 2000 were all greater than β_c.

Systematic experiments on clustering of particles into bands were carried out using the polymer particle whose properties are described in table 2. In these experiments we used the same fluid as TMA. The liquid is a mixture of Triton X 100, $ZnCl_2$ and water in combinations used to control viscosity. The high viscosity mixture is in the range of 20-60 poise and a density in the range 1.1~1.5 g/cm^3. The viscosity of the mixture is sensitive to temperature which was maintained at 68 ± 2°F in our experiments.

The experiments were conducted in two different rotating cylinders; one is 30 cm long and the inside diameter is 2.792 cm; the other is 15 cm long with the same inside diameter. The cylinder is supported horizontally and is driven at constant rotational speed Ω by a motor. For these experiments, the Reynolds number $R_e = (\Omega D_a^2)/\nu$, where Ω is the angular velocity of the cylinder, D_a the mean thickness of the film, and ν the kinetic viscosity of the pure liquid, is always very small (less than 10^{-2}). Inertial effects were generally negligible.

	F	R (cm)	Ω (rpm)	μ (poise)	ρ (g/cm^3)	ν (cm^2/s)	β	D_a (cm)	D_{min} (cm)	D_{min}/d_p
TMA 1	0.150	1.270	1.40	40.00	1.172	34.13	2.36	0.099	0.0480	1.04
TMA 2	0.125	5.000	2.80	49.00	1.172	41.81	2.50	0.323	0.149	3.24
M1	0.151	1.396	1.65	51.95	1.241	41.86	2.08	0.110	0.0605	0.931
M2	0.140	1.396	1.65	29.50	1.332	22.15	2.05	0.101	0.0440	0.677
M3	0.150	1.396	1.10	51.95	1.241	41.86	2.53	0.110	0.0494	0.760
M4	0.145	1.396	10.9	48.50	1.212	40.02	2.11	0.105	0.0966	1.49
M5	0.061	1.396	1.76	44.34	1.203	36.86	0.87	0.043	0.0403	0.620
M6	0.061	1.396	3.13	44.34	1.203	36.86	0.65	0.043	0.0412	0.634
M7	0.061	1.396	6.00	44.34	1.203	36.86	0.47	0.043	0.0418	0.648
M8	0.061	1.396	10.0	44.34	1.203	36.86	0.37	0.043	0.042	0.646
M9	0.046	1.396	38.71	2.377	1.498	1.587	0.67	0.032	0.0310	0.477
M10	0.046	1.396	51.10	2.377	1.498	1.587	0.58	0.032	0.0313	0.482

Table 3. Parameters for experiments reported in TMA (2000) and for our experiments (M1 through M10).

In table 3 we listed the parameters for the experiments using Triton mixtures reported by TMA and our experiments using the polymer particles (table2) colored blue for visualization.

The derived parameters $\left(\beta, D_a, D_{\min}, D_{\min}/d_p\right)$ are based on the properties of the pure liquid. The particles used by TMA1 and TMA2 were neutrally buoyant with density 1.172 g/cm^3, and diameter $d_p = 0.04625 \pm 0.00375\ cm$ in concentrations of 15%. The values of β for TMA1 and TMA2 based on the viscosity of the homogenous suspension would be 1.8 and 1.9, respectively. In our experiments, M1-M10, the density of the particles $\rho_p = 1.034\ g/cm^3$ is less than fluid density; the diameters of the particles are more dispersed with an average particle diameter $d_p = 0.065\ cm$. The concentrations of the particles range from 2% to 7%. The cylinder length is 15 cm from M4 and M5; otherwise the cylinder length is 30 cm. The values of the minimum film thickness, $D_{\min}/d_p$, listed in table 3 are all of $O(1)$, and are consistent with the observations of particle segregation driven by capillarity of the thin films. Although our particles are not neutrally buoyant, the sedimentation of the particles in the liquid used in the experiments can be neglected, since the sedimentation velocity of the particles in those liquids is of the order of $10\, nm/s$.

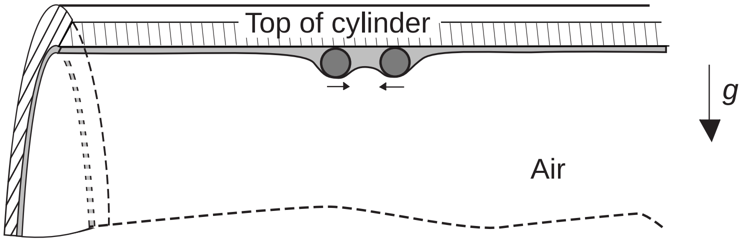

Figure 9. Capillary attraction of two particles hanging in a film at the top of a stationary rotating cylinder. The liquid film is the top section (the gray area). The air fills the other space.

After the cylinder is partially filled with the uniform suspension, it is turned a few times by hand and then put to rest so that the suspension covers the whole inside cylinder. It was observed that particles trapped in the thin film at the top of the cylinder move rather rapidly together under the action of capillarity (see figure 9). A similar kind of dynamics prevails when the cylinder rotates continuously at a constant velocity. In general the trapped particles are completely wet by the liquid as they pass through the deep pool at the bottom of the rotating cylinder. The segregation of particles generally occurs slowly. It takes a long time (hours) for the particles to reach the final steady band formation. The particle segregation occurs in a number of stages. The first is the formation of many small particle clusters, which were nucleated randomly along the cylinder after a few minutes. As time passes by, small particle clusters merge into larger ones.

Eventually they form into several comparatively large blocks which are often far from each other. These large blocks are quite stable, and stay separated. Meanwhile, they are gradually stretched thinner and longer in the flow direction, and eventually form cylindrical bands. Some bands may merge. The final formation of the bands is frequently uniform along the cylinder axis. The bands are not robustly stable; they may born, move, break and reform. It can be said that uniform dispersion is robustly unstable and clusters are robustly stable. The snap shots of the particle band formation are shown in figure 10.

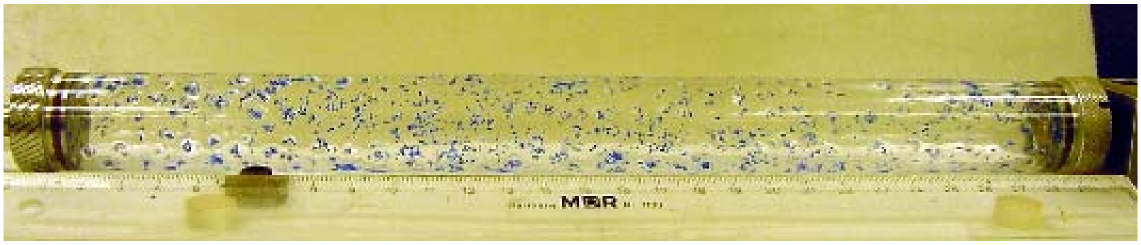

(a) Uniform distribution of particles at the beginning

(b) Particle clusters

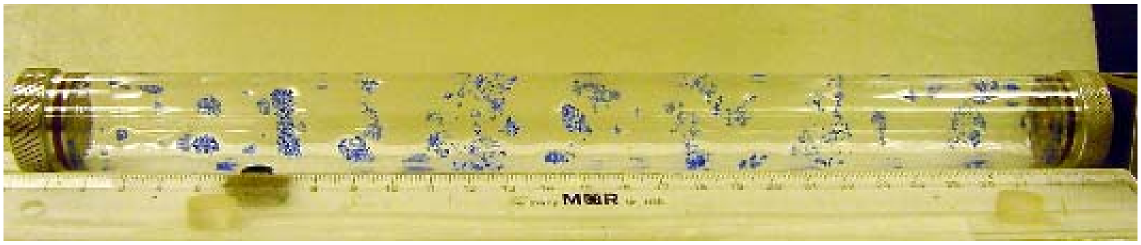

(c) Larger clusters

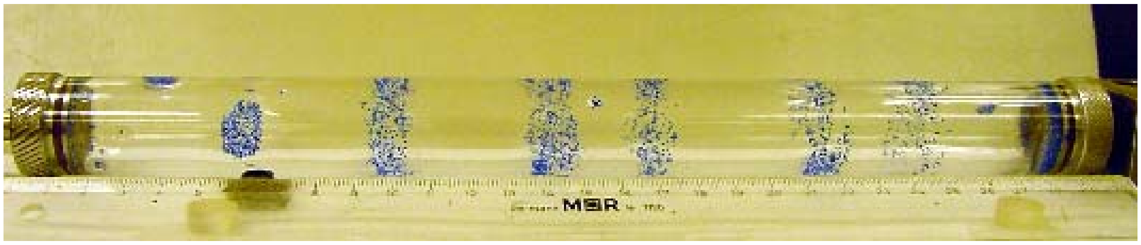

(d) Particle bands

Figure 10. Process of particle bands formation. The experiment is performed with high viscous Triton-mixture fluid under low rotating speed and low filling level (case M7).

In our experiments, it is observed that the formation of particle clusters or bands is easier in more viscous liquid at a low rotational speed. In experiments with a high-viscosity Triton mixture, we had to restrict to low rotating speed to get bands to separate. The rotational speed of the cylinder has to be slow enough such that the time needed for capillary attraction is comparable to the residence time for the particles in the thin part of the rimming film.

For the low-viscosity Triton mixtures, it is possible to get band separation by decreasing the filling level and at the same time increasing the rotational speed. The band formation was observed for the range of small β values (0.5~0.7). However, the rotational speed should not be too high, since then the particle clusters may not form, and even if particle clusters form they are not stable. The process of particle segregation in low-viscosity Triton mixtures (shown in figure 11) is similar to the case with high-viscous Triton-mixture (figure 10). Decreasing the filling level F as well as increasing the rotating speed is not always effective for low-viscosity fluids; we repeated the experiment with soybean oil and glycerin with relatively high rotating speeds (corresponding to β=1.0~1.2), and even though bands did not form, particle clusters were always generated by capillary induced "anti-diffusion".

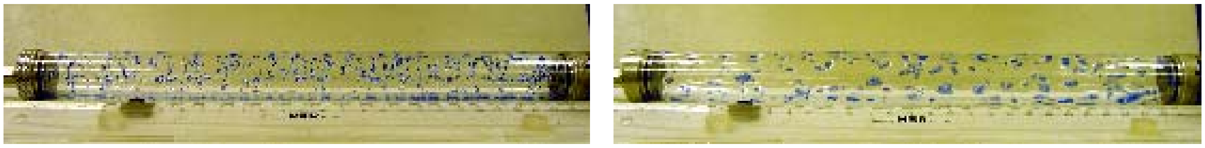

(a) Initial distribution (b) Particle clusters

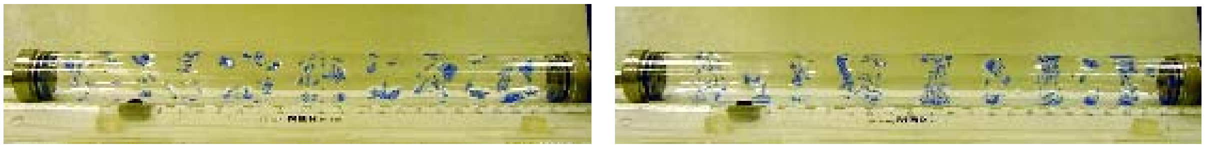

(c) Particle blocks (d) Initial bands

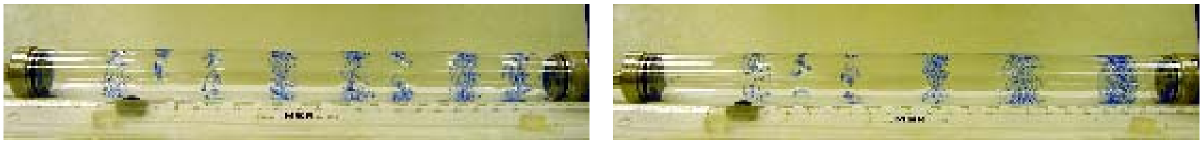

(e) Developing bands (f) Final bands

Figure 11. Process of particle bands formation. The experiment is performed with low viscous Triton-mixture fluid under relatively high rotating speed and low filling level (case M10).

Experiment M3 (table 3) is a high filling level case. Band separation occurred, however, there were many particles in the liquid sections between particle bands, in contrast to the case with low-filling where clear pure liquid between the particle bands were observed. The segregation of particles into cylindrical bands may take hours even days. The achieved configurations are stable for times of the order of hours and days. There is slight secondary flow and transverse movement of particles can be seen between particle bands.

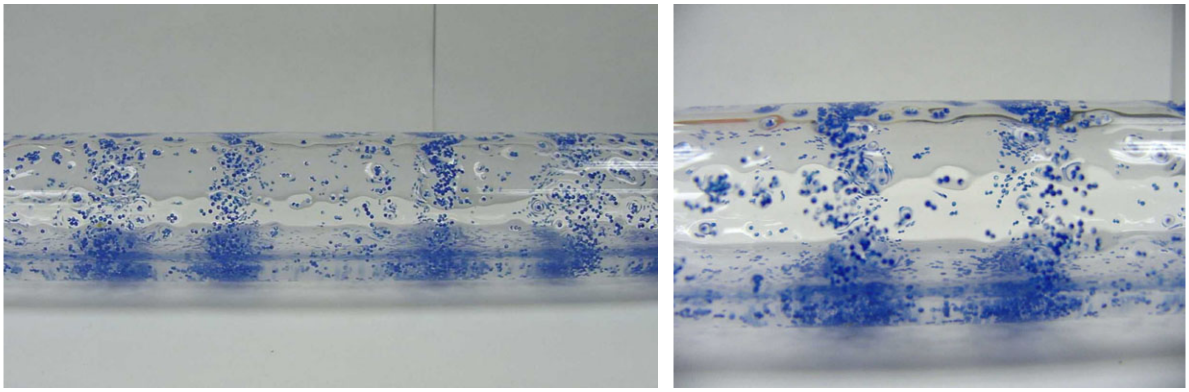

Figure 12. Particles which are initially distributed uniformly in a film rimming a rotating cylinder segregate into cylindrical bands (case M3). The formation of the bands takes hours.

In table 4, we list values for the times of formation of small clusters t_{w1}, large clusters (called blocks) t_{w2} and bands t_{w3} and the distance between bands as a function of the filling level and angular velocity. In general, for the same filling level, clusters form faster with the rotational speed increasing.

Filling level F	**Rotating speed** Ω **(rpm)**	**Waiting time for particle clusters** t_{w1} **(hour)**	**Waiting time for large blocks** t_{w2} **(hour)**	**Waiting time for bands** t_{w3} **(hour)**	**Average distance between bands** $\bar{l}$ **(cm)**
0.061	1.76	1.1	2.6	6.6	6.2
0.061	3.13	0.8	2.1	4.7	5.5
0.061	6.00	0.6	2.2	4.0	3.9
0.061	10.0	0.5	1.8	3.5	4.5
0.046	38.71	0.10	0.25	0.40	3.9
0.046	51.10	0.08	0.20	0.30	3.6

Table 4. Times and distance of cluster and band formation.

In this section we described cluster and band formation due to capillarity for lighter-than-liquid polymer particles in small concentrations in a highly viscous Triton mixture under conditions in which $D_{min}/d_p = O(1)$.

II-3. Particle segregation in water

We did experiments in water using the same polymer particles as before. In figure 13 we show cluster and band formation due to capillarity for heavier-than-water particles in large concentration 20.7% with $\beta = 15.94$.

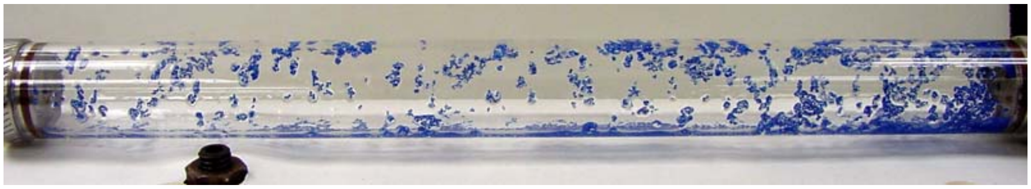

(a) 3 minutes after beginning of rotation

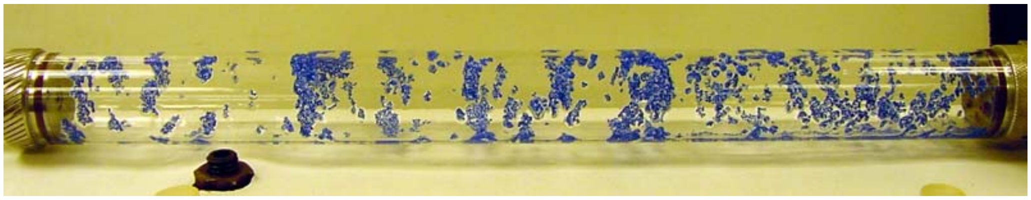

(b) 1.5 hours after beginning of rotation

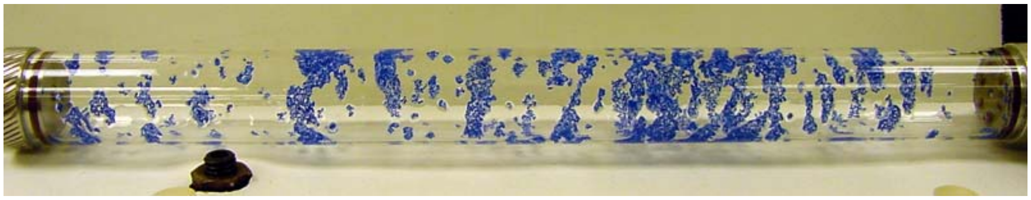

(c) 6 hours after beginning of rotation

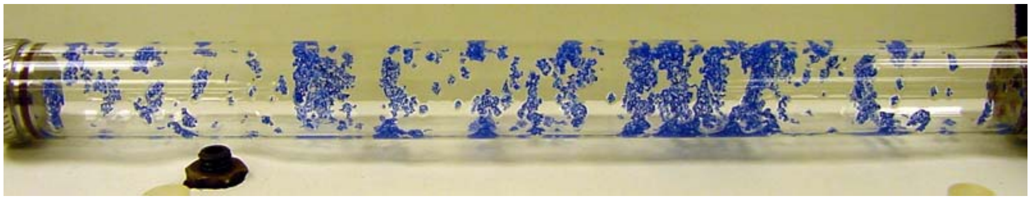

(d) 18 hours after beginning of rotation

Figure 13. Band formation of particles due to capillarity. The fluid is water (18°C) and the particles are polymer particles with a density of 1.034 g/cm^3 *and a diameter of 0.065 cm. The filling level of the fluid is 4.08% and the particle concentration is 20.7%. The rotating speed* $\Omega = 8.57$ *rpm,* $\beta = 15.94$*, average film thickness* $D_a = 0.288$ *mm, minimum film thickness* $D_{min} = 0.0213$ *mm,* $D_{min}/d_p = 0.033$*.*

II-4. Particle segregation in glycerin

Clustering and band formation due to capillarity is very robust in thin films on the inside of a rotating cylinder. In figures 14, 15 and 16 we show clusters and bands for three different cases. In figure 14 the neutrally buoyant particles are very large and the concentration of particles is 54.2%. In figure 15 the particles are much heavier than glycerin, but bands form nonetheless. In figure 16 the particles are lighter than glycerin and bands form as well.

Figure 14. Clustering of particles due to capillarity. The fluid is glycerin with a density of 1.173 g/cm^3, a viscosity of 1490 cp, and a surface tension of 41.46 mN/m. The particles are white Nylon particles with a density of 1.170 g/cm^3 and a diameter of 0.314 cm. The filling level of the fluid is 8.2% and the particle concentration is 54.2%. The rotating speed Ω=5.45 rpm, β=1.127, average film thickness D_a=0.585 mm, minimum film thickness D_{min}= 0.526 mm, D_{min}/d_p = 0.176. Clusters of particles form about 5 minutes after starting of rotation. Bands form occasionally but are not stable.

(a) 2.5 hours after beginning of rotation.

(b) 16 hours after beginning of rotation.

Figure 15. Band formation of particles due to capillarity. The fluid is glycerin with a density of 1.173 g/cm^3, a viscosity of 1490 cp, and a surface tension of 41.46 mN/m. The particles are 16/20 Naplite sands with a density of 2.59 g/cm^3 and a diameter of 0.959 mm. The filling level of the fluid is 7.85% and the particle concentration is 13.0%. The rotating speed Ω=5.45 rpm, β=1.079, average film thickness D_a = 0.559 mm, minimum film thickness D_{min} = 0.506 mm, D_{min}/d_p = 0.528.

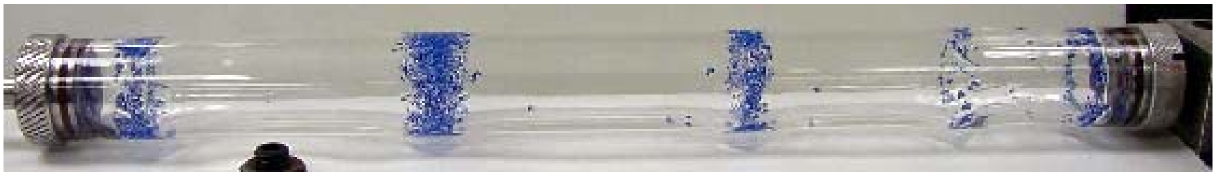

Figure 16. Band formation of particles due to capillarity. The fluid is glycerin with a density of 1.173 g/cm^3, a viscosity of 1490 cp, and a surface tension of 41.46 mN/m. The particles are polymer particles with a density of 1.034 g/cm^3 and a diameter of 0.65 mm. The filling level of the fluid is 10.5 % and the particle concentration is 4.8%. The rotating speed $\Omega = 5.45$ rpm, $\beta = 1.443$, average film thickness $D_a = 0.753$ mm, minimum film thickness $D_{min} = 0.605$ mm, $D_{min}/d_p = 0.931$. Band formation 15 hours after beginning of rotation is shown in the figure.

III. Particle segregation due to the formation of bubbles

When a partially filled horizontal cylinder is rotated at rates which are not too high or too low such that the effects of surface tension and gravity are both important, air bubbles separated by disks of liquid will form. The bubbles are then not centered and can take different shapes depending on conditions. The off-center bubbles pump the liquid to form the secondary motion which is from the bubble to the liquid disks near the bubble surface and from the liquid disks to the bubble near the wall (see figure 19). Particles are centrifuged to the wall if they are heavier than the liquid; they are centrifuged to the surface of the bubble is they are heavier than the air but lighter than the liquid. Driven by the secondary motion, lighter-than-liquid particles segregate in the liquid disks; heavier-than-liquid particles segregate in the region circling the bubbles when the bubbles are off the wall, and in the liquid disks when the bubbles touch the wall.

III-1. Bubbles in a partially filled rotating cylinder

Rimming flow is a coating flow inside a partially filled rotating horizontal cylinder. The filling level F is the volume fraction of liquid in the cylinder; when F is large there is very little air in the cylinder. If the filling fraction is not too small, which is characterized by $\beta > \beta_c$ in expression (9) and the flat bump of the film profile depicted in figure 8(b) becomes unstable, air bubbles will form and the shape, numbers and position of these bubbles depend on F, the angular velocity Ω, the surface tension γ, the viscosity of the liquid, the density difference between liquid and gas $\rho_l - \rho_g$, and the dimensions of the apparatus. The qualitative effects of all these parameters are fairly well understood.

When the cylinder rotates so fast that the effects of centrifugal gravity $\Omega^2 R$ (R is the cylinder radius) overwhelm those of terrestrial gravity, $\Omega^2 R/g >> 1$, all of the liquid is centrifuged and rotates with the cylinder as a rigid body; in this case the air is centered and if the filling level is not too small, bubbles will form under the action of an interfacial potential (see Preziosi and Joseph 1987). An important parameter for this potential is

$$J = \frac{(\rho_l - \rho_g)\Omega^2 R_b^3}{\gamma} \tag{20}$$

where R_b is the maximum radius of the bubble. This parameter J does not depend on gravity, viscosity, filling level or the length of the apparatus. If $J < 4$ cigar shaped bubbles will form; the bubbles are all identical but the number of them depends on the filling level and the history of their creation. $J = 4$ is a limiting value for the drop shape parameters; when Ω is increased, the maximum radius of the bubble decrease in such a way that $J = 4$; when the ratio of bubble length to radius $L/R_b > 8$, the bubble shape is very closely approximated by a cylinder of constant radius R_b bounded by two semi-spherical end caps (this is nearly achieved in figure 17f).

Equation $J = 4$ was derived from heuristic arguments by Vonnegut (1942). It is the working formula for “spinning drop” tensiometer which are used to measure interfacial tension (see Joseph *et al*. 1992).

As Ω is increased, R_b decreases with $J = 4$. Since the bubble volume is fixed the length L increases and eventually all the bubbles collect end to end to form a long cylindrical column, rigorously centered, which does not change under further increases of angular velocity.

Coming the other way, decreasing from large values of $\Omega^2 R/g$, the length of the bubbles will decrease and the maximum radius R_b will increase with $J = 4$. Eventually, when $\Omega^2 R/g \sim O(1)$ the effect of terrestrial gravity becomes important, the bubble rise; secondary motions are generated and velocity becomes important. Photographs which exhibit typical regimes are displayed in figure 17 where we compare soybean oil whose viscosity is 282 cp with Triton mixture whose viscosity is 2950 cp. The main effect of viscosity here is to maintain rigid motion of the fluid under perturbations with gravity. The radius of the cylinder used in our experiments is 0.64 cm and the ratio of centrifugal to terrestrial gravity are listed below:

Ω	200	300	600	1000

$\Omega^2 R/g$	0.287	0.64	2.57	7.16

Table 5. Gravity ratio for different angular velocity.

When $\Omega = 1000$ rpm, the bubble is rigorously centered and extends from end to end of the cylinder. When $\Omega = 600$ rpm, the effects of gravity are sensible. The perturbation of rigid motion in the high viscosity Triton mixture is small and the secondary motions are much weaker than in soybean oil. The configuration in figure 17(f) is essentially uninfluenced by gravity with centered bubbles whose shape is determined by a potential lined up end to end. At lower value of Ω, the bubbles rise but the secondary motions which distort the bubbles are less important in the high viscosity fluid.

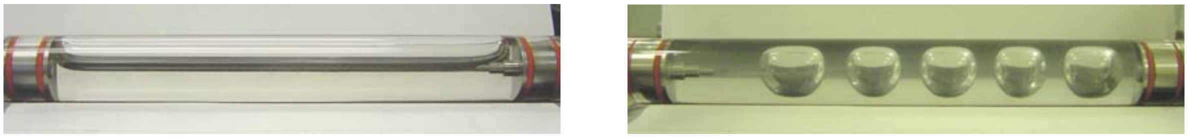

(a) Soybean oil, $\Omega = 200$ rpm

(b) Triton mixture, $\Omega = 200$ rpm

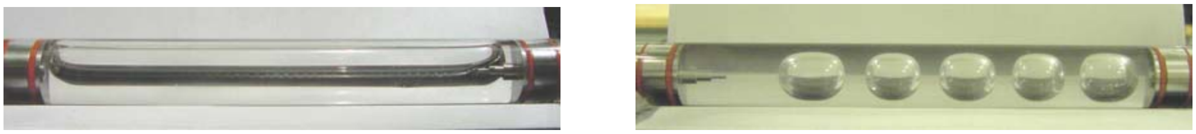

(c) Soybean oil, $\Omega = 300$ rpm

(d) Triton mixture, $\Omega = 300$ rpm

(e) Soybean oil, $\Omega = 600$ rpm

(f) Triton mixture, $\Omega = 600$ rpm

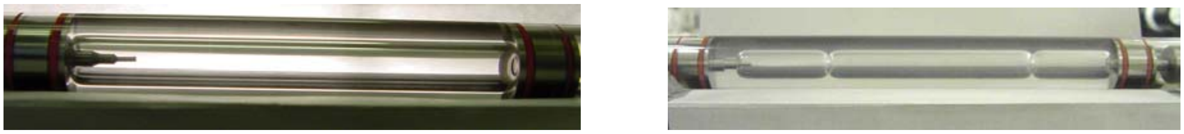

(g) Soybean oil, $\Omega = 1000$ rpm

(h) Triton mixture, $\Omega = 900$ rpm

Figure 17. Comparison of soybean oil and Triton mixture under same conditions

As the angular velocity is decreased to zero the liquid and air stratify, with all the air at the top. Even in this case, a stationary liquid, the air may separate into bubbles induced by capillarity if the filling level is not very high; if the filling level is near 100%, the very small amount of air will rise to the top and form a single short bubble due to the restraining action of surface tension.

Many unusual shapes of bubbles may occur when $\Omega^2 R/g \sim O(1)$, as put into evidence and in the papers by Balmer (1970), Sanders, Joseph and Beavers (1981) and Preziosi and Joseph (1988).

The combined effects of the filling level and rotational speed on the formation of the bubbles are of interest. When the gravity ratio parameter is small, $\Omega^2 R/g << 1$, the liquid and air are stratified with a thin film being dragged up by the rotating cylinder. If the filling level is large enough, the thickness of the film dragged up increases as the cylinder rotates faster. Up to a critical condition, the thick liquid film on the top of the cylinder cannot be maintained and part of it falls down under gravity, subsequently the single air bubble breaks. On the other hand, when the gravity ratio parameter is large, the air forms a rigorously centered cylindrical column stretching from end to end of the cylinder. If the rotational speed decreases, the stabilizing effect of the centrifugal acceleration decreases. Up to a point, the combined effects of the surface capillarity and the terrestrial gravity will break up the air bubble into smaller ones.

The critical conditions under which the single air bubble breaks were determined experimentally for the rimming flow of soybean oil. The two lines on a (F, Ω) plane in figure 18 indicate the critical conditions. When the filling level and rotational speed fall in the region between the two lines, the bubble breakup is observed; otherwise, a single air bubble is stable. Note that when $F < 0.4$, a single air bubble is stable at any rotational speed.

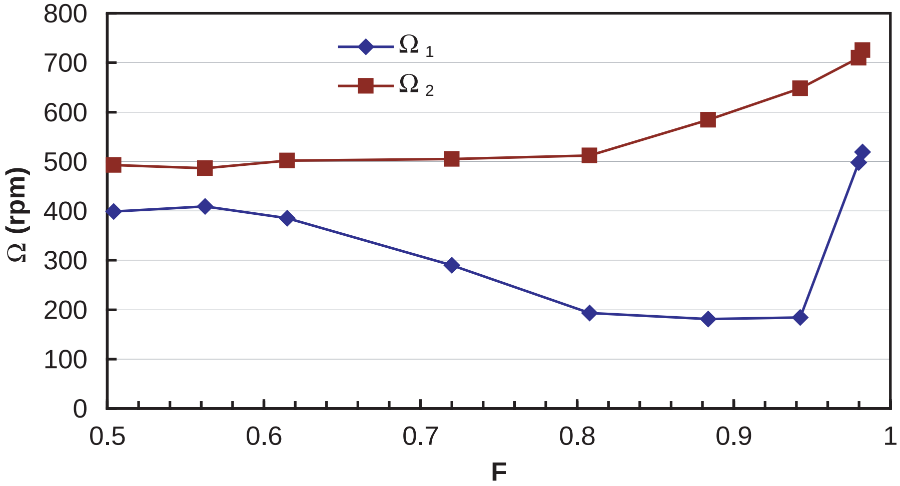

Figure 18. Critical conditions for the single air bubble breakup in soybean oil. The experiments were carried out in a cylinder of glass with inside diameter 1.28 cm and length 22.14 cm. When $F < 0.4$, a single air bubble is stable at any rotational speed. For $F \geq 0.5$, when the rotational speed is between Ω_1 and Ω_2, air bubble breakup is observed.

III-2. Particles segregation due to bubbles

In a system with several smaller air bubbles distributed along the length of the cylinder and displaced off the axis of the rotation by the action of gravity, the motion of the particles suspended in the liquid may be driven by the secondary motions associated with the pumping effect around the off-center bubbles. The liquid passes by the above-center bubbles which are relatively stationary and are pushed away from the places occupied by the air. The pumping motion of the bubble sets up an eddy which will push the liquid from the bubble to the liquid disks near the bubble surface and from the liquid disks to the bubble near the wall (see figure 19).

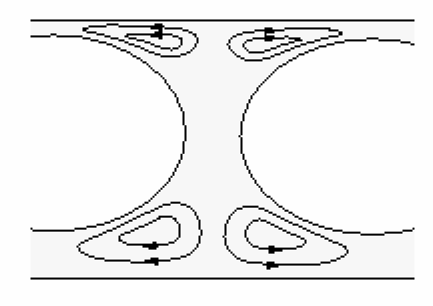

Figure 19. The eddies set up by the pumping motion of the off-center bubble. Liquid flows from the bubble to the liquid disks near the bubble surface and from the liquid disks to the bubble near the wall.

(a) $\Omega = 200$ rpm

(b) $\Omega = 300$ rpm

(c) $\Omega = 600$ rpm

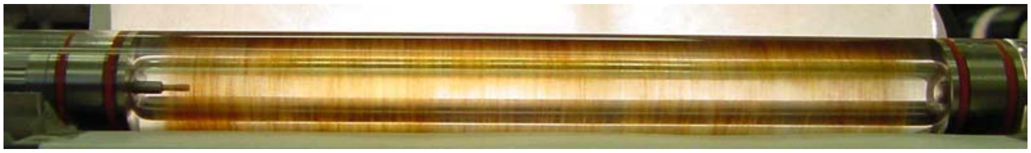

(d) $\Omega = 1000$ rpm

Figure 20. Particle segregation of resin particles $\rho_p = 1.13$ *g/cm, average diameter* $d_p = 0.065$ *cm, concentration 15% in soybean oil, filling level 60%.*

The changes in the nature of heavier-than-liquid particle segregation as $\Omega^2 R/g$ changes (see table 5) are shown in four panels of figure 20 where we go from stratified flow (a) to uniform flow (d). The experiments were carried out in a cylinder of glass with inside diameter 1.28 cm and length 22.14 cm. Comparing figure 17(a, c) with figure 20(a, b) we see that the particles promote bubble formation at low speeds in soybean oil. This effect may be due to the increase in the effective density of the mixture which increases the value of J in (20) by replacing ρ_l with $\rho_c = \rho_p \phi + \rho_l (1 - \phi)$ where ϕ is the particle fraction.

The heavier-than-liquid particles are centrifuged and segregated near the cylinder wall where secondary motions are weakest. The eddies push the particles on the wall to the region circling the bubble and away from the gap between bubbles when the rotational speed of the cylinder is large enough to centrifuge the air away from the wall but not so large as to center it (figure 20c).

At lower speeds, the bubbles rise all the way to the wall and the particles on the wall are pushed to the space between bubbles (figure 20a,b).

In figure 21 we show that for heavier-than-liquid particles, segregation does not depend sensitively on the type of particle.

(a) 16/30 AcFrac PR, $\Omega = 300$ rpm

(b) Resin particle, $\Omega = 300$ rpm

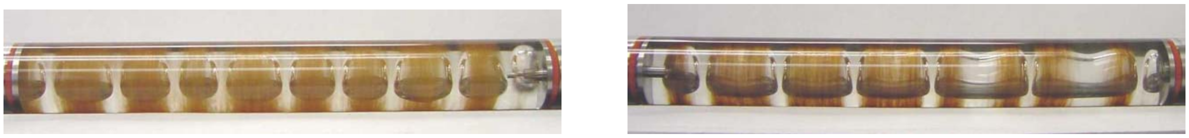

(c) 16/30 AcFrac PR, $\Omega = 600$ rpm

(d) Resin particle, $\Omega = 600$ rpm

Figure 21. Segregation of two different particles in soybean oil. The AcFrac PR particles are hydrophilic, ρ_p *=1.64 g/cm, average diameter* $d_p = 0.088$ *cm; the resin particles are hydrophobic,* $\rho_p = 1.13$ *g/cm, average diameter* $d_p = 0.065$ *cm.*

(a) 200 rpm

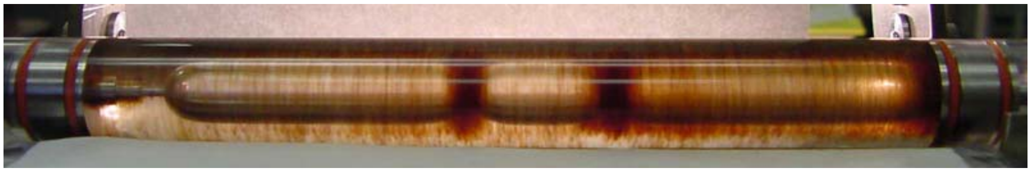

(b) 600 rpm

Figure 22. Particle segregation of resin particles $\rho_p = 1.13$ *g/cm, average diameter* $d_p = 0.065$ *cm, concentration 8.96% in glycerin, filling level 66.7%.*

Figure 22 shows the segregation pattern of particles which are lighter than the liquid. The lighter-than-liquid particles are centrifuged to the surface of the bubbles. The eddies described in figure 19 will push the particles to the space between air bubbles. Compare figure 20(c) with figure 22(b), the different patterns should be noted. The heavier-than-liquid particles segregate in the region above the bubbles, whereas the lighter-than-liquid particles segregate in the space between bubbles. In figure 22(b), some of particles do circulate around the bubbles because the bubbles are almost centered and the secondary motions are weak.

III-3. Segregation of bi-disperse suspension in a partially filled rotating cylinder

Preliminary experiments using suspensions of particles with two different weights show that the rotating flow leads to segregation of the two types of particles into separate regions whose exact form depends on the weight and concentration of particles and on other features which have yet to be determined. Here we show that this kind of segregation does occur and is robust.

Figure 23 and 24 show two experiments of segregation of bi-disperse suspension in aqueous glycerin solutions. The different concentrations of the brown resin particles cause different patterns of segregation (figure 23a and figure 24a). The rotating flow finally leads to uniform distribution of particles, with the heavy particles at the end of the cylinder and the light particles at the middle of the cylinder (figure 23c and figure 24c). Figure 25 shows bi-disperse suspension in water. The configuration shown in figure 25 is stable for hours.

(a) 30 minutes after beginning of rotation.

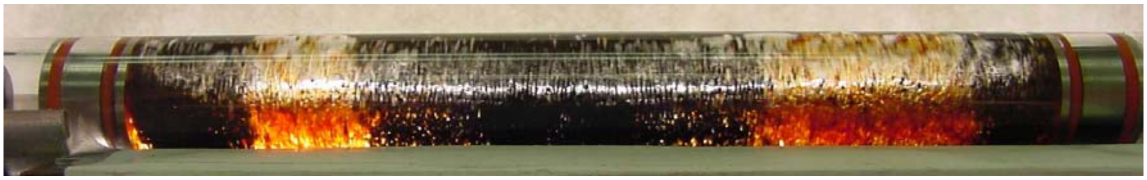

(b) two hours after beginning of rotation.

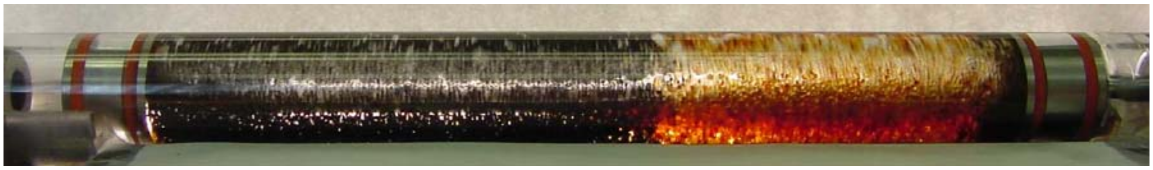

(c) 20 hours after beginning of rotation.

Figure 23. Segregation of two types of particles in a 47.8% aqueous glycerin solution, $\rho_l = 1.09$ g/cm^3. The filling level of the liquid is 0.354. The black is a silicon particle with $\rho_p = 3.07$ g/cm^3, average diameter $d_p = 0.05$ cm, and its concentration is 21.7%. The brown is a resin particle with $\rho_p = 1.13$ g/cm^3, average diameter $d_p = 0.065$ cm, and its concentration is 12%. The rotational speed is 165 rpm.

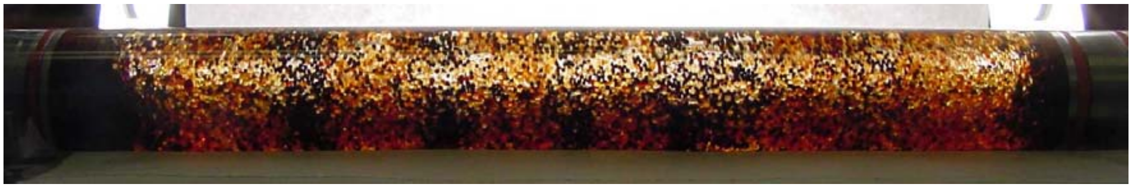

(a) four minutes after beginning of rotation.

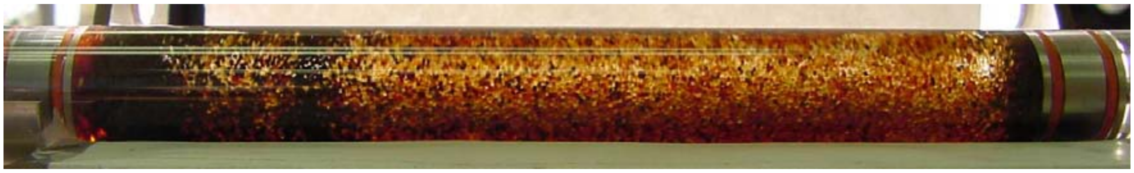

(b) 24 minutes after beginning of rotation.

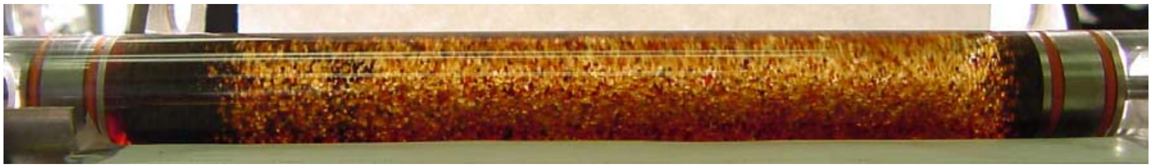

(c) 36 minutes after beginning of rotation.

Figure 24. Segregation of two types of particles in a 48.7% aqueous glycerin solution. The filling level of the liquid is 0.328. The black is a silicon particle with $\rho_p = 3.07$ *g/cm*^{3}*, average diameter* $d_p = 0.05$ *cm, and its concentration is 16%. The brown is a resin particle with* $\rho_p = 1.13$ *g/cm*^{3}*, average diameter* $d_p = 0.065$ *cm, and its concentration is also 16%. The rotational speed is 160 rpm.*

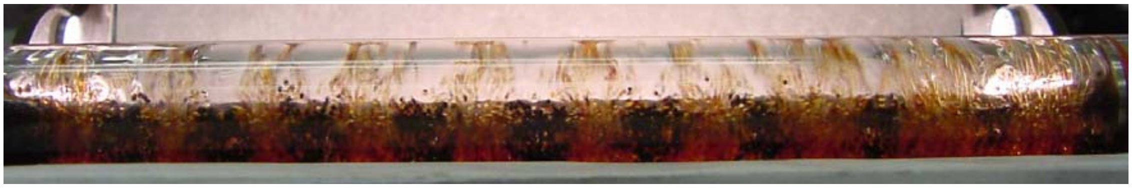

Figure 25. Segregation of two types of particles in water. The filling level is 0.357. The black is a silicon particle with $\rho_p = 3.07$ *g/cm*^{3}*, average diameter* $d_p = 0.05$ *cm, and its concentration is 4%. The brown is a resin particle with* $\rho_p = 1.13$ *g/cm*^{3}*, average diameter* $d_p = 0.065$ *cm, and its concentration is 16%. The rotational speed is 306 rpm.*

IV. Conclusion

The principal facts concerning capillary attraction and self-assembly of small lighter- and heavier-than-fluid floating particles were reviewed. These facts were applied to explain the clustering and segregation of bands of particles in a thin liquid film rimming the inside of a partially filled, slowly rotating cylinder in situations resembling those first observed by Tirumkudulu, Mileo and Acrivos (2000). In our experiments clustering and band formation occurred under all kinds of conditions, for lighter- and heavier-than-liquids, for small particles and large particles, and for low concentrations and high concentrations of particles. Uniform dispersions of particles in thin films are robustly unstable to anti-diffusion due to capillarity, and clusters which are self-assembled are robustly stable. The conditions required to support this phenomenon are that the liquid film is thin relative to the particle size; the film should be thin, or in any case, not much thicker than the particles. The rotation speed of the cylinder should be slow enough that the time needed for sensible capillary attraction is comparable to the time of residence of the particle in the thin part of the rimming film.

Particle segregation may also be generated by pumping secondary motions of fluid by off-center gas bubbles, which arise when the gravity parameter $\Omega^2 R/g \leq O(1)$ and the filling level is not too small. Lighter-than-liquid particles segregate in the liquid disks between bubbles; heavier-than-liquid particles segregate in the region above the bubbles when they are off the wall, and in the liquid disks when the bubbles touch the wall.

A third regime of segregation of bi-disperse suspension of particles of different heavier-than-liquid weights, which stratify when the cylinder is at rest, form into rings when the cylinder rotates. Different forms of the ring appear to depend on the particle concentration and other factors which have as yet to be determined.

Acknowledgement

The work of authors Joseph, Wang, Bai and Yang was supported by the NSF/CTS under grant 9873236, and by the Engineering Research Programs at the Office of Basic Energy Science of the DOE.

References

Balmer, R.T. The hydrocyst—a stability phenomenon in continuum mechanics, *Nature* (London) **227**, 600 (1970).

Bowden, N., I.S. Choi, B.A. Grzybowski, G.M. Whitesides, Mesoscale self-assembly of hexagonal plates using lateral capillary forces: synthesis using the “capillary bond”, *J. Am. Chem. Soc*. **121**, 5373-5391. (1999).

Bowden, N., A. Terfort, J. Carbeck, G.M. Whitesides, Self-assembly of mesoscale objects into ordered two-dimensional arrays, *Science,* **276**, 233-235. (1997).

Brenner, H. and L.G. Leal. A micromechanical derivation of Fick’s law for interfacial diffusion of surfactant molecules, *J. Colloid Interface Sci.* **65**, 191 (1978).

Brenner, H. and L.G. Leal. Conservation and constitutive equations for adsorbed species undergoing surface diffusion and convection at a fluid-fluid interface, *J. Colloid Interface Sci.* **88**, 136 (1982).

Chan, D.Y.C., J.D. Henry Jr. and L.R. White. The interaction of colloidal particles collected at the fluid interface, *J. Colloid Interface Sci*. **79**, 410 (1981).

Danov, K.D., R. Aust, F. Durst and U. Lange. Influence of the surface viscosity on the hydrodynamic resistance and surface diffusivity of a large Brownian particle, *J. Colloid and Interface Science*, **175**(1), Oct 36-45 (1995).

Fortes, M.A. Attraction and repulsion of floating particles, *Can. J. Chem.* **60,** 2889 (1982).

Gifford, W.A. and L.E. Scriven. On the attraction of floating particles, *Chem. Engrg. Sci.* **26**, 287-297 (1971).

Goldman, A.J., R.G. Cox and H. Brenner. Slow viscous motion of a sphere parallel to a plane wall—I Motion through a quiescent fluid, *Chem. Eng. Sci*. **22**, 637-651 (1967).

Govindarajan, R., P.R. Nott, and S. Ramaswamy. Theory of suspension segregation in partially filled horizontal rotating cylinders, *Phy. Fluids*, **13**(12), 3517-3520 (2001).

Grzybowski, B.A., N. Bowden, F. Arias, H. Yang, G.M. Whitesides, Modeling of menisci and capillary forces from the millimeter to the micrometer size range, *J. Phys. Chem. B* **105**, 404-412. (2001).

Joseph, D.D., M. Arney, G. Ma, 1992. Upper and lower bounds for interfacial tension using spinning drop devices, *J. Colloid Interface Sci*., **148**(1), 291-294.

Karweit, M.J. and S. Corsin. Observation of cellular patterns in a partly filled, horizontal, rotating cylinder, *Phys. Fluids* **18**, 111 (1975).

Katoh, K., H. Fujita and E. Imazu. Motion of a particle floating on a liquid meniscus surface, *J. Fluids Engrg*. **114**, 411 (1992).

Kralchevsky, P.A., V.N. Paunov, N.D. Denkov, I.B. Ivanov and K. Nagayama. Energetical and force approaches to the capillary interactions between particles attached to a liquid-fluid interface, *J. Colloid and Interface Sci.* **155**, 420-437 (1993).

Kralchevsky, P.A., V.N. Paunov, I.B. Ivanov and K. Nagayama. Capillary meniscus interactions between colloidal particles attached to a liquid-fluid interface, *J. Colloid Interface Sci.* **151**, 79 – 94 (1992).

Kralchevsky, P.A. and K. Nagayama. Capillary interactions between particles bound to interfaces, liquid films and biomembranes, *Advances in Colloid and Interface Sci.* **85**, 145-192 (2000).

Majumdar, S.R., M.E. O'Neill, and H. Brenner. Note on the slow rotation of a concave spherical lens or bowl in two immiscible semi-infinite viscous fluids, *Mathematika,* **21**, 147-154 (1974).

Nicolson, M.M. The interaction between floating particles, *Proc. Cambridge Philosophical Soc.,* **45**, 288 (1949).

Petkov, J.T., N.D Denkov, K.D Danov, O.D. Velev, R. Aust and F Durst. Measurement of the drag coefficient of spherical particles attached to fluid interfaces, *J. Colloid and Interface Science,* **172**, 147-154 (1995).

Poynting, J.H. and J.J. Thompson. *A Text-book of Physics: Vol. 1, Properties of Matter*, C. Griffith & Co. Ltd (London) 153-155 (1913).

Preziosi, L. and D.D. Joseph. The run-off condition for coating and rimming flows, *J. Fluid Mech.*, **187**, 99-113 (1988).

Princen, H.M. Equilibrium shape of interfaces, drops, and bubbles. Rigid and deformable particles at interfaces, *Surface and Colloid Science*, E. Matijevie, ed., Interscience, New York, Vol. 2, p.1-84 (1969).

Rapacchietta, A.V. and A.W. Neumann. Force and free-energy analyses of small particles at fluid interfaces: II. Spheres, *J. Colloid and Interface Sci.*, **59**(3), 555-567 (1977).

Redoev, B., M. Nedjalkov and V. Djakovich. Brownian motion at liquid-gas interfaces. 1. Diffusion coefficients of macroparticles at pure interfaces, *Langmuir,* **8**, 2962 (1992).

Ruschak, K.J. and L.E. Scriven, Rimming flow of liquid in a rotating horizontal cylinder, *J. Fluid Mech.* **76**, 113-127 (1976).

Saif, T.A., On the capillary interaction between solid plates forming mensci on the surface of a liquid, J. Fluid Mech. in press (2002).

Schneider, Y.C., M.E. O'Neill, and H. Brenner. On the slow viscous rotation of a body straddling the interface between two immiscible semi-infinite fluids, *Mathematika,* **20**, 175 (1973).

Timberlake, B.D., J.F. Morris, Concentration band dynamics in free-surface Couette flow of a suspension, *Phy. Fluids*, 14(5), 1580-1589 (2002).

Tirumkudulu, M., A. Tripathi, A. Acrivos. Particle segregation in monodisperse sheared suspensions, *Phy. Fluids*, **11**(3), 507-509 (1999).

Tirumkudulu, M., A. Mileo, A. Acrivos. Particle segregation in monodisperse sheared suspensions in a partially filled rotating horizontal cylinder, *Phy. Fluids*, **12**(6), 1615 (2000).

Tirumkudulu, A. Acrivos. Coating flows within a rotating horizontal cylinder: Lubrication analysis, numerical computations, and experimental measurements, *Phys. Fluids,* **13**, 3517 (2001).

Vonnegut, B., Rotating Bubble Method for the Determination of Surface and Interfacial Tension, *Rev. Sci. Instrum*. **13**, 6-9, (1942).

Wakiya, S. *Niigata Univ. College of Engng. Res. Rept. 6*, Nagoaka, Japan (30 March 1957).

Table of contents

- **Fluid Dynamics of Floating Particles**

Singh and Joseph (2005) have developed a numerical package to simulate particle motions in fluid interfaces. The particles are moved in a direct simulation respecting the fundamental equations of motion of fluids and solid particles without the use of models. The fluid-particle motion is resolved by the method of distributed Lagrange multipliers and the interface is moved by the method of level sets. The present work fills a gap since there are no other theoretical methods available to describe the nonlinear fluid dynamics of capillary attraction.

Two different cases of constrained motions of floating particles are studied here. In the first case, we study motions of floating spheres under the constraint that the contact angle is fixed by the Young-Dupré law; the contact line must move when the contact angle is fixed. In the second case, we study motion of disks (short cylinders) with flat ends in which the contact line is pinned at the sharp edge of the disk; the contact angle must change when the disks move and this angle can change within the limits specified by Gibbs extension to the Young-Dupré law. The fact that sharp edged particles cling to interfaces independent of particle wettability is under appreciated and needs study.

The numerical scheme presented here is at present the only one which can move floating particles in direct simulation. We simulate the evolution of single heavier-than-liquid spheres and disks to their equilibrium depth and the evolution to clusters of two and fours spheres and two disks under lateral forces collectively called capillary attraction. New experiments by Wang, Bai and Joseph (WBJ 2003) on the equilibrium depth of floating disks pinned at the edge are presented and compared with analysis and simulations.

Contents

I. Introduction

In the work which follows, we will be considering the motions of particles which float in the interfaces between two fluids. We shall sometimes describe the wettability properties of the particles as hydrophobic or hydrophilic. The mathematical description of our problem in terms of air and water is only a convention for the general problem of motion of particles in the interfaces between any two fluids.

It is well known that small tea leaves floating on the tea surface collect near the cup wall due to the formation of a meniscus that rises near the wall and results in a net capillary force towards the wall. The meniscus rises near the wall because the water wets the cup. If, on the other hand, the liquid does not wet the cup, i.e., the meniscus falls near the cup wall, small floating particles tend to move away from the wall and toward the center of the cup. Similarly, the deformation of liquid-liquid interfaces due to floating light particles, or due to trapped heavy particles, gives rise to capillary forces on the particles which cause them to cluster, as can be seen in figure I.1. The clustering of particles on interfaces is important because it modifies the interfacial properties of the two-phase system and is used in many flotation based extraction and separation processes (Gerson, Zaijc and Ouchi 1979). More recently, this effect has been used for the self-assembly of submicron sized particles on two-liquid interfaces (see Bowden, et al. 1997,1999, Grzybowski, et al. 2001, and references therein).

(a)

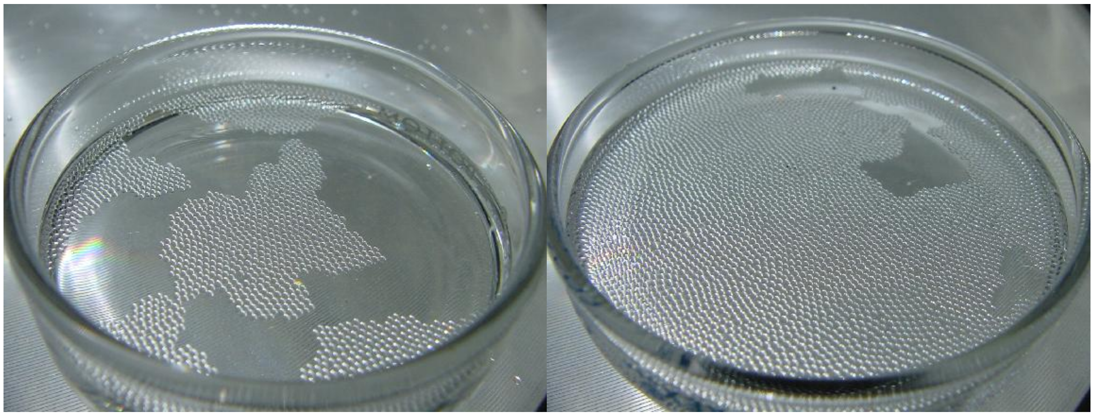

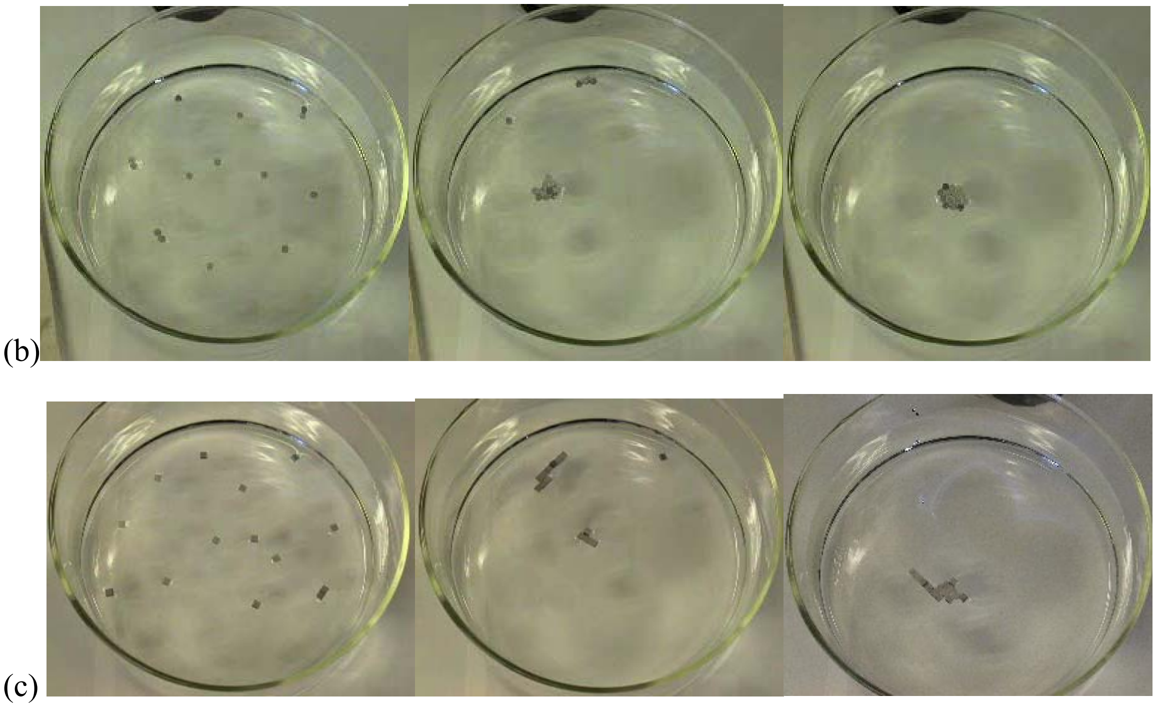

***Figure** I.1. (WBJ 2003) Capillary attraction of floating particles. (a) Neutrally buoyant copolymer particles of nominal diameter 0.1 cm cluster in water/air interface. (b) Heavy aluminum disks (short cylinders with circular cross sections) hanging in water/air interface at the sharp rim. The distributions of 14 particles at 0 second (left), after 60 seconds (middle) and after 200 seconds (right) are shown. The diameter of the disks is 0.3175 cm and its height is 0.15875 cm. (c) Heavy aluminum bricks with square cross sections hanging in water/air interface at the sharp corners. The distributions of 14 particles at 0 second (left), after 142 seconds (middle) and after 220 seconds (right) are shown. The dimension of the bricks is 0.3175 cm × 0.3175 cm × 0.15875 cm. The attractive power of capillarity on floating particles is very long range and the accelerations in the final stage of clustering are exceedingly large. Movies of these experiments can be viewed at* [*http://www.aem.umn.edu/research/particles/floating/*](http://www.aem.umn.edu/research/particles/floating/)*.*

The motion of tea leaves towards or away from the wall, in the above example, is entirely due to the deformation of the meniscus near the cup wall. The clustering of particles, on the other hand, is a consequence of the interface deformation caused by neighboring particles. Specifically, when two heavy hydrophobic spheres are close to each other the deformed interface around the spheres is not symmetric because the interface height between the spheres is lowered by the capillary force; on the other hand, lighter-than-water hydrophilic spheres will rise as shown in figure I.2. In both of these cases, the lateral component of interfacial tension is attractive and the spheres tend to cluster. But, when one sphere is hydrophilic and the other is hydrophobic, the lateral force at short range is repulsive and tight clusters cannot form.

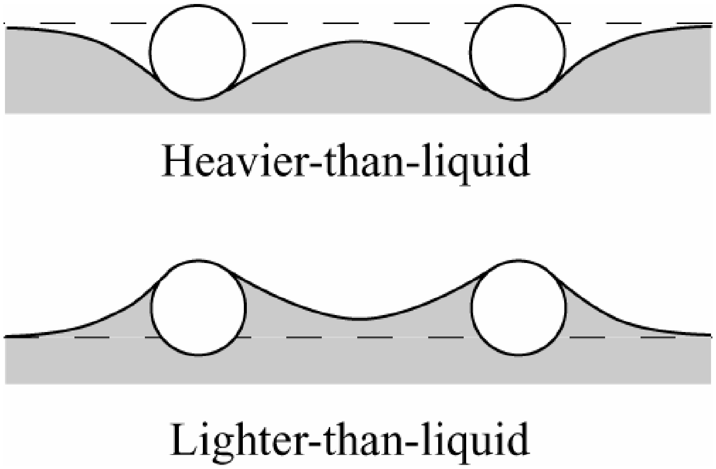

***Figure** I.2. Spherical particles in water. (a) heavier-than-water hydrophobic spheres. The meniscus between the spheres is below the undisturbed level. Assuming that the contact angle remains fixed, the horizontal component of capillary force moves them toward each other. (b) Lighter-than-water hydrophilic spheres will rise into the elevated section of the meniscus and come together.*

The literature on capillary attraction is cited by Kralchevsky and Nagayama 2000 and Saif 2002, here in section III, and in the paper on capillary attraction of particles embedded in a thin film rimming the inside of a rotating cylinder by Joseph, Wang, Bai, Yang and Hu 2003. These works do not treat the case of capillary attraction of particles pinned to the interface at a sharp edge which is one of the main subjects in this paper.

Problems of evolution to equilibrium of heavier-than-liquid floating particles may be studied by direct numerical simulation (DNS); this simulation method fills a gap identified by Gifford and Scriven 1971 who note that

"casual observations… show that floating needles and many other sorts of particles do indeed come together with astonishing acceleration. The unsteady flow fields that are generated challenge analysis by both experiment and theory. They will have to be understood before the common-place 'capillary attraction' can be more than a mere label, so far as dynamic processes are concerned."

The basic facts about the equilibrium of single particles are discussed in section II and new experiments on the equilibrium depth of disks pinned at their edges are presented. The prior literature on capillary attraction is briefly reviewed in section III. In section IV we set out the equations which govern the motions of floating particles and introduce the basic dimensionless groups which characterize these motions. In section V, we outline the numerical method stressing only those details which are new. Readers interested in constructing or improving the numerical algorithm used in this study can find a detailed description in the appendix. In section VI, we compute the solutions of the initial value problems, starting from rest, for one, two and four spheres with contact angle prescribed. In section VII, we compute the solutions of the initial value problems, starting from rest, for one and two disks pinned at their sharp edges. The solutions are compared with experimental data.

II. Floating particles which should sink

In this section we consider the forces that determine the equilibrium depth of a floating particle. Princen 1969 gave an excellent analysis of this problem for a sphere and prismatic particles with sharp edges. Keller 1998 generalized this analysis for smooth bodies of arbitrary shape. Kotah, Fujita and Imazu 1992 used the floating ball to measure contact angles.

Floating particles which should sink are held up by capillary forces at the line of contact of the three phases on the particle surface. The hanging depth between the contact line and the highest point on the meniscus depends on whether the meniscus attaches to the particle on the smooth surface with uniquely determined normal or at a corner or edge where the normal is undefined. Here we show that the hanging depth is determined by the position of the contact line on a floating sphere when the contact angle is fixed by the Young-Dupré law, and by the value of the contact angle which changes with the weight of the particles when the contact line is pinned at a sharp edge.

II.1 Floating particles with sharp edges

It is well known, but not well understood, that liquid-air-solid interfaces tend to locate at sharp edges. This mechanism allows a prismatic disk or cube to float with contact line pinned to its sharp rim. Even when a downward vertical force is applied by adding weights onto the top surface of a floating disk, as discussed below, the contact line remains pinned to the rim.

Obviously, a prismatic particle which is denser than the liquid below can float only if the vertical component of interfacial tension is sufficiently large to balance its buoyant weight and will sink when this is no longer true.

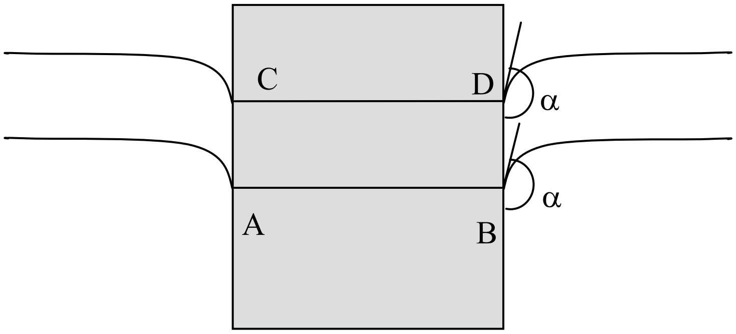

Figure II.1. The vertical component of capillary force for the disk does not change when the contact line moves from AB to CD, for two different floating heights, because the contact angle α is fixed. For a sphere, the vertical component of the capillary force changes as the contact line moves on its surface.

The effects of the buoyant weight may be isolated in the case of a circular cylinder or disk, with axis vertical, which is suspended with the contact line on a circle perpendicular to the cylinder generator (see figure II.1). The contact angle is fixed by the Young-Dupré law and does not change even as the contact line sinks due to change in the cylinder buoyant weight. The cylinder can be denser than the liquid provided that the vertical capillary force is just large enough to balance its buoyant weight. If the cylinder's weight is increased, it will sink further and the contact line on the smooth surface will move upwards. But, the vertical component of capillary force will not change because the angle between the interface and the horizontal, which only depends on the contact angle, does not change when the cylinder sinks (see figure II.1). Consequently, the maximum interfacial deformation, the vertical distance between the contact line and the highest point on the meniscus, will also not change as the cylinder sinks. The buoyancy force acting on the disk, however, increases, as it sinks into the liquid below. Disks of different weight in air, with same contact angle and buoyant weight can be suspended as in figure II.1.

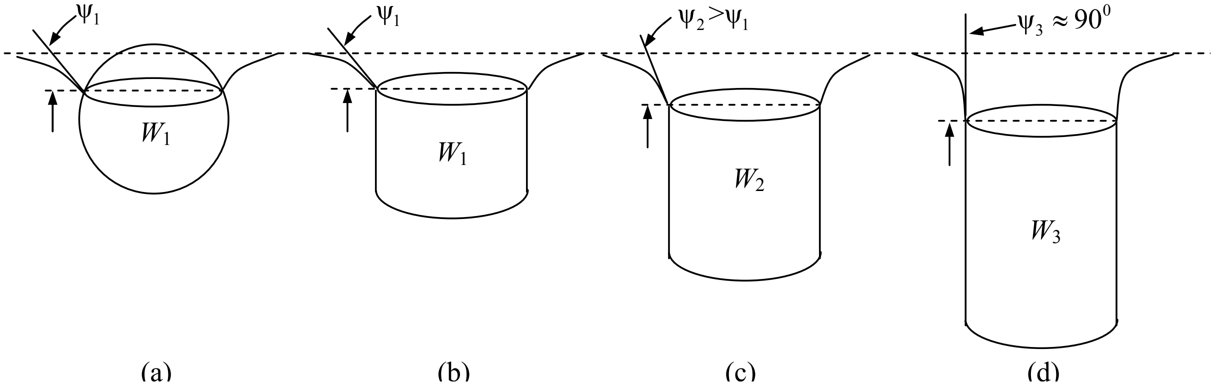

Figure II.2. Effect of changing the buoyant weight on the contact angle at the rim of a cylinder. The contact angle is the same for a sphere (a) and disk (b) when the buoyant weights are the same. Increasing the buoyant weight leads to larger contact angles which have larger vertical components of the capillary force as shown in (b), (c) and (d). In the experiments of (WBJ 2003) the cylinder would sink when $\psi \leq\sim 90^0$; however theoretically the cylinder can float with $\psi > 90^0$ (Hesla and Joseph 2003).

At a critical value of the disk weight, the contact line moves from the smooth surface to the sharp edge. If the disk weight is increased further, the contact line remains pinned at the sharp corner for a range of weight, even though the disk continues to sink further (see figures II.2-II.5). A heavier-than-liquid disk can float with the interface pinned to the sharp edge, as in figure II.2, provided the vertical component of the capillary force is large enough to balance its buoyant weight. In this paper, we will study the dynamics of floating disks in this state.

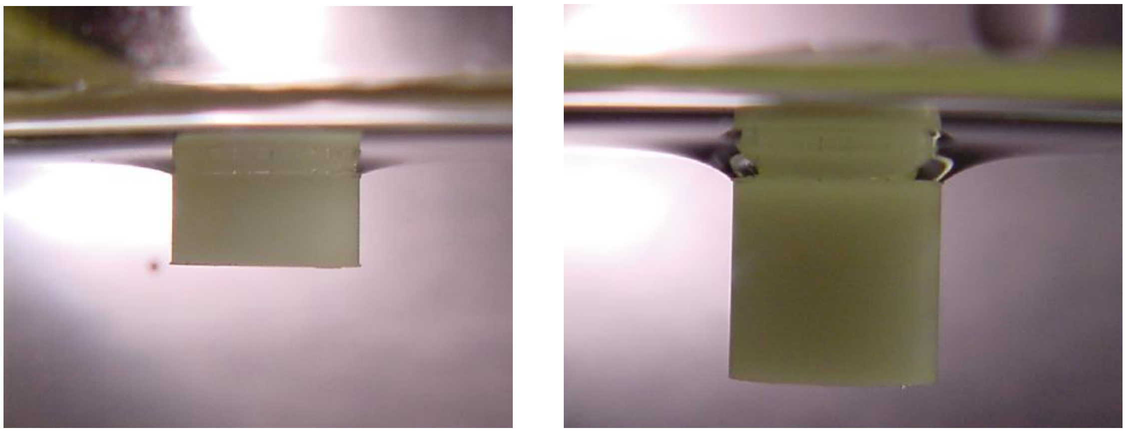

(a) (b)

Figure II.3. (WBJ 2003). Two photos of floating Teflon disks of density ρ_s=1.4g/cc held at the contact line in water of density ρ_f=1g/cc. Both disks have a diameter of 0.8 cm; the height from the bottom of the disk to the contact line is 0.4cm in (a) and 0.8 cm in (b). The contact angle in (b) is larger than that in (a) in order to satisfy the force balance. The image of the disk projecting above the contact line is a reflection in the surface of the water.

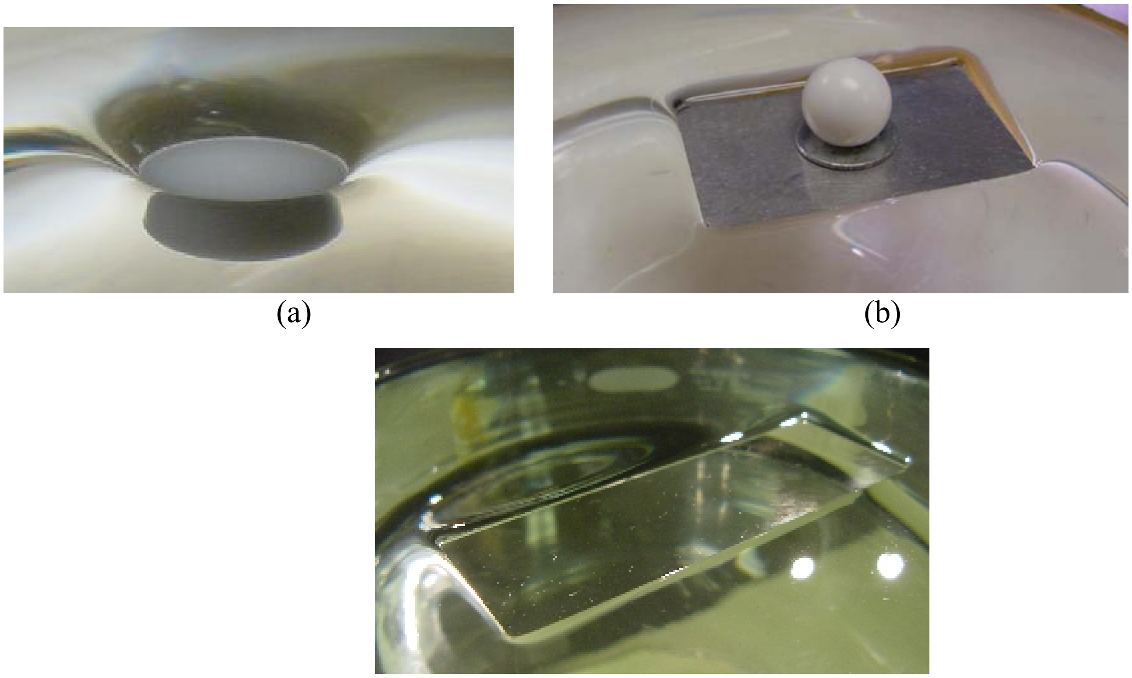

(a) (b)

(c)

Figure 4 (WBJ 2003). (a) The meniscus for a Teflon cylinder of density ρ_s=1.4g/cc hanging from a flat edge in water. (b) An aluminum plate can float in water hanging from the sharp edge; when weighted by a Teflon ball, the plate still floats but the hanging depth increases. (c) A floating glass plate is held at the sharp edge in water. Spheres of aluminum and glass will sink in water, provided that the spheres are not so small that the surface tension will dominate the buoyant weight. The contact angle on the hydrophilic glass plate and the hydrophobic Teflon plate is determined by their buoyant weight and not by wettability.

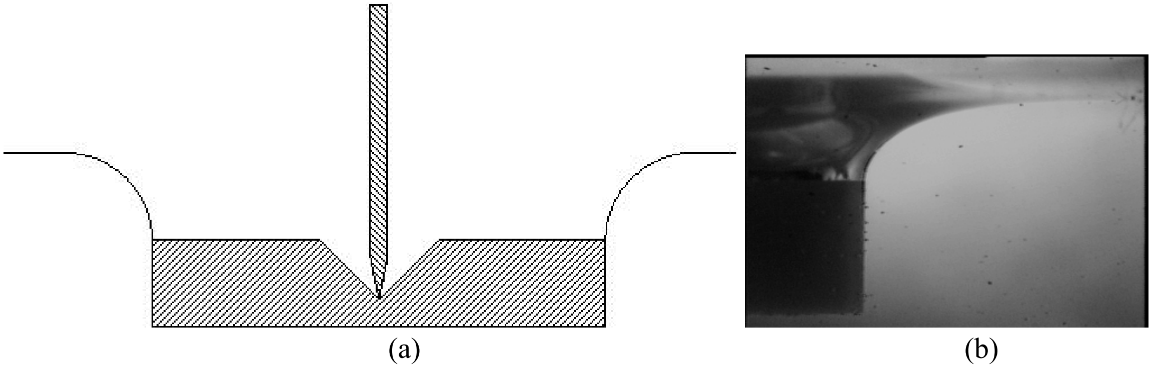
(a) (b)

Figure II.5 (WBJ 2003). (a) A cartoon for the experiment determining the critical contact angle at the sharp edge. See section II.5 for details of the experiment. (b) A photo from the video showing that the contact angle reaches 90° at a moment just before the disk sinks. The square, solid black part in the photo, is the disk and the bright part is water.

II.2 Gibbs Inequality

This pinning of the contact line at the disk edge appears to be conflict with the Young-Dupré law which states that the equilibrium contact angle between a liquid, a gas and a solid wall is constant

$$\gamma_{LG} \cos \alpha = \gamma_{SG} - \gamma_{SL},$$

where α is the contact angle and γ_{LG}, γ_{SG} and γ_{SL} are the interfacial energy between liquid and gas, solid and gas, and solid and liquid, respectively. To ensure that the equilibrium contact angle is fixed, when the interface at a small distance away from the contact line moves the contact line must also move. But, since the normal at the corner is not defined, Young-Dupré law is not violated provided the contact angle α at the corner, as shown in figure II.6, stays within the range specified by the Gibbs extension to Young-Dupré law:

$$\alpha_0 < \alpha < 180-\phi + \alpha_0$$

where ϕ is the wedge angle and α_0 is the equilibrium contact angle for the vertical face (see Gibbs 1906 and Princen 1969).

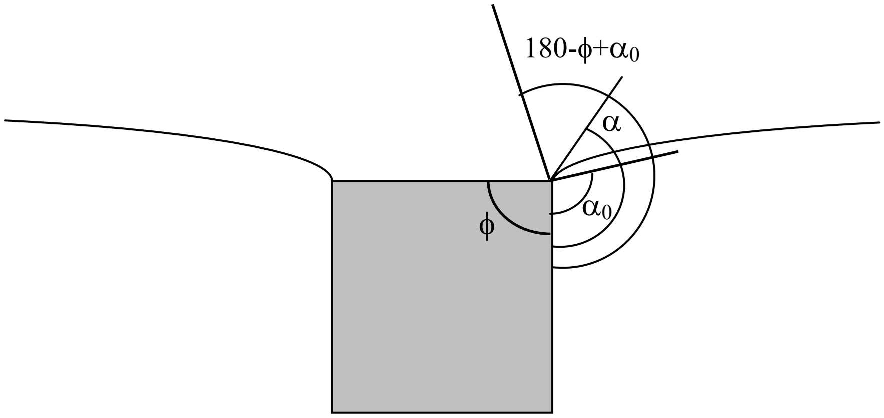

Figure II.6. Two limiting angles for the Gibbs extension to Young-Dupré law which states that the contact angle α *at the sharp edge can take any value between* α_0 *and 180-*ϕ *+* α_0*.*

II.3 Vertical force balance in equilibrium

The analysis of the forces which keep a sphere suspended in the interface between fluids was given first by Princen 1969, then by Rapacchietta and Neumann 1977, and Kotah, Fujita and Imazu 1992, who used the floating ball to measure contact angles. A detailed discussion of the vertical balance of a ball in equilibrium can be found in Joseph et al. 2003. The analysis of the forces which keep a heavy disk suspended in the interface at the sharp upper rim of the disk was given by Hesla and Joseph 2003, following an earlier analysis of Princen 1969 for a prismatic particle.

For equilibrium, the buoyant weight of particle must be equal to the vertical component of the capillary force. If the particle density is larger than that of both fluids, equilibrium is possible only when the particle is hydrophobic and the vertical component of capillary force is large enough to balance its buoyant weight. The interface shape in this case is concave down and the net capillary force acts against gravity.

Force balance for a sphere

The conditions for equilibrium of a floating sphere can be framed with the help of the cartoon in figure II.7. The vertical component of capillary force F_C depends on the particle radius R, the surface tension coefficient γ, the filling angle θ_c and the contact angle α, and is given by

$$F_C = 2\pi(R\sin\theta_c)\gamma\sin[\theta_c-(\pi-\alpha)] = -2\pi(R\sin\theta_c)\gamma\sin(\theta_c+\alpha). \qquad (II.1)$$

The above expression holds for both the hydrophobic and hydrophilic cases.

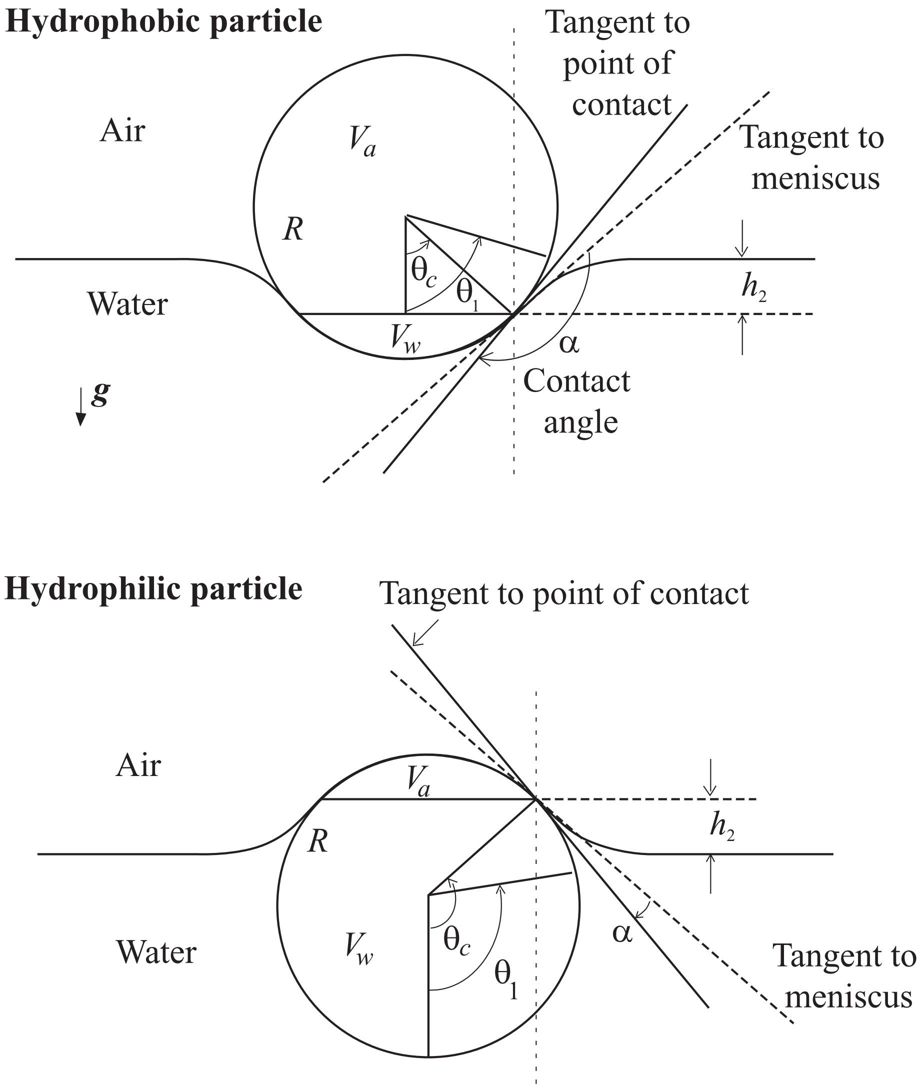

***Figure** II.7 (Joseph et al. 2003). Hydrophobic and hydrophilic particles in equilibrium. The position of the contact ring determines the angle θ_C. The point of extension of the flat meniscus on the sphere determines the angle θ_1.* $h_2=R(\cos\theta_c - \cos\theta_1)$.

The weight mg of a heavy particle in equilibrium is balanced by a capillary force F_c and net pressure force F_p satisfying:

$$\mathbf{F}_C + \mathbf{F}_p = m\mathbf{g}, \tag{II.2}$$

where F_c is given by II.1. F_p is the pressure force given by

$$F_p = \int_0^{\theta_c} p\cos\theta\,(2\pi R\sin\theta)\,R\,d\theta \tag{II.3}$$

$$= \rho_L g\pi R^3 (\frac{2}{3} - \cos\theta_c + \frac{1}{3}\cos^3\theta_c) + \rho_a g\pi R^3 (\frac{2}{3} + \cos\theta_c - \frac{1}{3}\cos^3\theta_c) -$$
$$(\rho_L - \rho_a) g h_2 \pi R^2 \sin^2\theta_c$$

where h_2 is the meniscus height, and ρ_L is the density of the lower liquid and ρ_a is the air density. Substituting into (II.2) we get

$$\begin{aligned} &2\pi\gamma(R\sin\theta_c)\sin(\theta_c + \alpha) - \rho_L g\pi R^3 (\frac{2}{3} - \cos\theta_c + \frac{1}{3}\cos^3\theta_c) - \\ &\rho_a g\pi R^3 (\frac{2}{3} + \cos\theta_c - \frac{1}{3}\cos^3\theta_c) + (\rho_L - \rho_a) g h_2 \pi R^2 \sin^2\theta_c = mg \end{aligned} \qquad \text{(II.4)}$$

with $m = \frac{4}{3}\pi R^3 g\rho_p$, the above expression may be expressed in a dimensionless form as

$$\begin{aligned} &\sin\theta_c \sin(\theta_c + \alpha) = -\frac{1}{2} B[\frac{4}{3} l_1 - (\frac{2}{3} - \cos\theta_c + \frac{1}{3}\cos^3\theta_c) - \\ &l_2 (\frac{2}{3} + \cos\theta_c - \frac{1}{3}\cos^3\theta_c) + (1 - l_2)(\cos\theta_1 - \cos\theta_c)\sin^2\theta_c] \end{aligned} \qquad \text{(II.5)}$$

where $B = \rho_L R^2 g/\gamma$ is the Bond number and $l_1 = \rho_p/\rho_L$ and $l_2 = \rho_a/\rho_L$ are the density ratios.

The capillary force acts against gravity only when $\theta_C + \alpha - \pi$ is positive, in which case $\sin(\theta_C + \alpha) < 0$, otherwise it acts in the same direction as gravity. For example, if $\alpha = 3\pi/4$, a heavy sphere will float with $\theta_C > \pi/4$. For $\alpha = 3\pi/4$ and $\theta_C = \pi/4$, the force F_C is zero and there is no interface deformation (see figure II.8). F_c increases when θ_C is increased from $\pi/4$ and reaches its maximum value at $\theta_C \approx 1.9$ and then decreases with increasing θ_C. On the other hand, when the contact angle is π, F_C is always non-negative and its maximum value is for $\theta_C = \pi/2$, i.e., the sphere half immersed in the lower liquid. The buoyant weight of the particle, of course, also changes with θ_C.

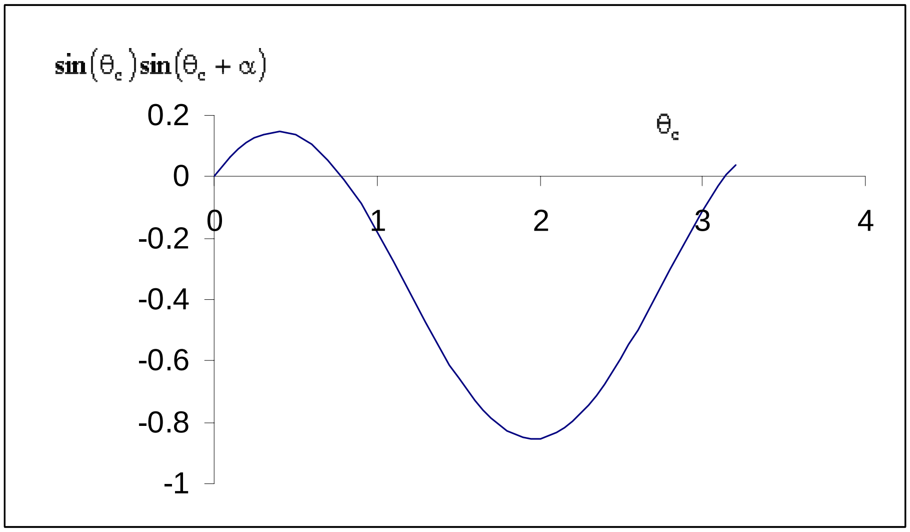

***Figure** II.8. For the contact angle* $\alpha = 3\pi/4$, $\sin(\theta_c)\sin(\theta_c+\alpha)$ *is plotted as a function of* θ_C. *Notice that the vertical component of capillary force* F_C *given by (II.1) is negative for* $\theta_C < \pi/4$ *and maximum for* $\theta_C \approx 1.9$ *radians=~109º.*

Force balance for a disk

The force balance for the disk is given by (II.2). From figure II.9 it is clear that

$$F_c = 2\pi R\gamma \sin\psi \qquad \text{(II.6)}$$

$$F_p = (P_0 - P_a)\pi R^2 = \rho_L g(h + h_2)\ \pi R^2 \qquad \text{(II.7)}$$

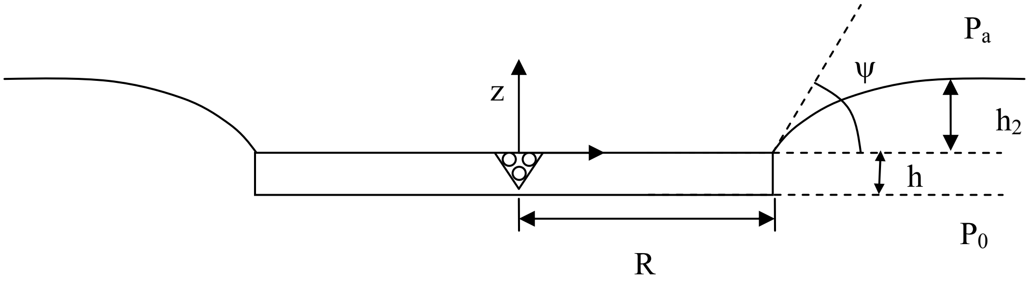

Figure II.9. Heavier than liquid disk hanging from a flat edge. The capillary force is given by $F_c=2\pi R\gamma\sin\psi$, *where* γ *is the interfacial tension. The meniscus is* $z = h(r)$; $h(\infty)=h_2$ *is the highest value of z on the meniscus.* P_a *is air pressure and* P_0 *is the pressure at the bottom of the disk* $z = -h$. *The disk may be weighted by heavy balls in the cone shaped cavity, increasing* h_2 *and* ψ *without sinking.*

Substituting into (II.2), we get

$$2\pi R\gamma \sin\psi + \rho_L gV + \pi R^2 h_2\rho_L g = mg, \qquad \text{(II.8)}$$

where $V=\pi R^2 h$ is the volume of the disk. The angle $\psi=\alpha-90$, where α is the contact angle, is measured from the horizontal. The dimensionless form of (II.8) is given by

$$\sin\psi = B\frac{1}{2}\left[(l_1-1)\frac{h}{R}-\frac{h_2}{R}\right]. \tag{II.9}$$

The meniscus height h_2 is determined from the solution of the meniscus equation

$$\rho g h[h(r)-h_2]=\frac{\gamma}{r}\left[\frac{rh'(r)}{\sqrt{1+h'(r)^2}}\right]', \tag{II.10}$$

where the origin (z, r)=(0,0) is in the plane at the center of the circle of radius R defined by the contact line. The integration starts at (z, r)=(0,R) where

$$h'(r)=\tan\psi. \tag{II.11}$$

Far from the particle, the meniscus is flat and

$$\lim_{r\to\infty}\{rh'(r), h(r)\}=\{0, h_2\}. \tag{II.12}$$

For a cylinder, the values of ψ and h_2 can be determined from the solution $z=h(r)$, using (II.8) together with

$$\rho g\int_R^\infty [h_2-h(r)]r\,dr=\gamma R\sin\psi \tag{II.13}$$

which follows from (II.9), (II.11) and (II.12).

Hesla and Joseph 2003 worked an exact numerical solution of the problem just considered; they gave a simple mathematical argument that as the weight of the floating disk is gradually increased (figure II.2), the maximum contact angle at the sharp rim which is attained before the disk sinks is greater than 90^o. They presented numerical results which support this conclusion. Though such solutions are allowed by the equilibrium analysis, they have not been observed. It may be that configurations with contact angle greater than 90^o are unstable (see figure II.5).

II.4 Small particles, large particles and heavy particles

The left side of equation (II.5), and thus also the right side, lies in the range $-1\le\sin\theta_C\sin(\theta_C+\alpha)\le 1$. Obviously, (II.5) cannot be solved if B is too large which may be the case when the sphere is too heavy or too large. Similarly, for a floating disk if B is too large, (II.9) cannot be solved; the disk will sink when the capillary force is not large enough to balance its buoyant weight.

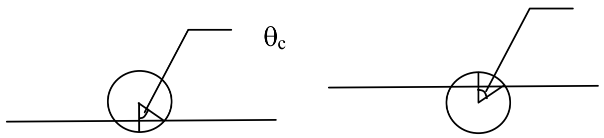

Small hydrophobic sphere Small hydrophilic sphere

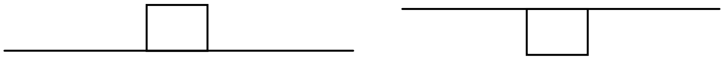

Small hydrophobic disk Small hydrophilic disk

Figure II.10. The deformation of the interface due to floating sufficiently small spheres or disks is negligible. A small hydrophobic sphere will float with $\theta_C \approx \pi - \alpha$ *so that interfacial deformation is negligible even if it is denser than the liquid below. A small less dense hydrophilic sphere also does not deform the interface. Similarly, a small dense hydrophobic disk floats on the surface with negligible penetration into the liquid.. A small hydrophilic disk which is less dense than the lower liquid does not deform the interface and it is kept inside the lower liquid by the capillary force which acts downwards.*

As R approaches zero, the capillary force, which varies linearly with R, dominates the buoyant weight of the sphere which varies with R^3. In this limit since the Bond number $B=\rho_L R^2 g/\gamma \to 0$, the right hand side of (II.5) is zero and thus sin ($\alpha + \theta_C$) $\approx$ 0 or $\theta_C \approx \pi - \alpha$ (see figure II.10). We may therefore conclude that heavy small particles can be suspended without causing significant interfacial deformation when B is small. Krahshesky, et al. 1992, 1993 noted that for particles floating on water this limit is approximately reached when their diameter is 10 μm. Hence, the lateral capillary forces, which arise from interfacial deformation, are also insignificant when the particle diameter is smaller than 10 μm. Similarly, if volume of the disk approaches zero, the capillary force, which varies linearly with R, will dominate its buoyant weight which varies as hR^2. In this limit, the right hand side of (II.8) is zero and $\sin\psi \approx 0$ or $\psi = 0$. The disk therefore does not deform the interface, and floats with its top surface in the plane of the interface (see figure II.10).

The vertical component of the capillary force for the two positions in figure II.1 can be zero only if the contact angle α is 90°. This implies that a small hydrophobic (α>90°) disk must float on its bottom edge, as shown in figure II.10; it cannot be suspended as in figure II.1. When the contact line is pinned to an edge the contact angle can take any value, between the two values specified by Gibbs inequality. The argument just given applied to all cases in which the Bond number is small, to particles with other shapes, like cubes and to lighter and larger particles.

When particles are partially immersed in a thin liquid film and their weight is supported by the substrate below, the arguments just given are not applicable and the interface deformation can be significant even for small particles. Kralchevsky and Nagayama 2000 have shown that in thin films the particle-particle attraction force increases with decreasing particle size.

II.5 Experiments on floating disks pinned to the interface at the sharp edge (WBJ 2003)

WBJ used a 3.38g Teflon cylinder with a cone cut in the center. 0.25 g steel beads were put in the cone to change the weight (see figure II.9). The radius, height and volume of the disk are [1.27 cm, 0.495 cm, 2.51cc]. The angle ψ and the depression h_2 were measured using a video camera. Measurements were taken at several azimuthal positions and the average value ψ and h_2 recorded. After inserting the measured parameters into the force balance equation (II.8), the difference between the measured vertical force and the particle weight, the residual e was computed:

$$e = \mathrm{mg} - 2\pi \mathrm{R}\gamma \sin\psi - \rho_1 \mathrm{g}\pi \mathrm{R}^2\left(\mathrm{h} + \mathrm{h}_2\right) \qquad \text{(II.16)}$$

m(gram)	3.38	3.63	3.88	4.13	4.38
ψ (degree)	28.4	37.8	43.0	51.7	71.1
H_2(cm)	0.130	0.176	0.206	0.255	0.302
$2\pi R\gamma\sin\psi/mg$(%)	5.27	6.31	6.58	7.11	8.08
$\rho_l gh_2\pi R^2/mg$(%)	19.44	24.54	26.94	31.34	34.98
$\lvert e\rvert/mg$(%)	1.03	0.01	1.8	0.77	0.36

Table II.1 (WSJ 2003). Quantities entering into the force balance equation (II.8). The residual e is computed from (II.16). The values of e are small.

Table II.1 shows that the contact angle at the rim increases when the weight of the particle is increased. A maximum weight can be held in this manner; beyond this weight the particle will sink. WBJ did experiments to determine the critical contact angle corresponding to this maximum weight. The 3.38g Teflon disk with a cone cut in the center was used. The contact angle was gradually increased by pushing the disk down into the water with a needle (see figure II.5). A video camera was used to record the whole process and the critical contact angle was determined using the video replay. The contact angle increased up to 90° while the contact line was pinned at the rim (see figure II.2); when the needle was pushed further down, the contact line moved away from the sharp edge to the flat top of the disk, and the disk sank instantaneously. They concluded that the critical contact angle corresponding to the maximum weight which could be held at the sharp edge is 90°. Hesla and Joseph 2003 have shown that that the equilibrium solution for this problem allows contact angles larger than 90°; the vertical component of the capillary force decreases while the buoyant force increases maintaining the balance. These larger contact angles may be unstable.

III. Motion due to the capillarity of floating particles on liquid surfaces

The deformation of a fluid-fluid interface due to floating or trapped particles gives rise to lateral capillary forces. A simple explanation is given in figure I.2. A heavier-than-liquid particle will fall down a downward sloping meniscus while an upwardly buoyant particle will rise.

There are several ways to isolate the effects of capillarity uninfluenced by gravity (see Joseph et al. 20003). Poynting and Thompson 1913 investigated the capillary effect by considering two vertical plates immersed in a liquid, the space between the plates is a two dimensional capillary tube. If the plates are hydrophobic, the level in the capillary gap sinks below the liquid outside; if the plates are hydrophilic the levels will rise. Another way to take away the effects of gravity is to support the particles on a substrate. In this case, the horizontal forces are due to capillary effects alone. Katoh, Fujita and Imazu 1992 studied the motion of a particle floating on a liquid meniscus surface which could be interpreted as motion on a substrate because the foaming phlystyrol particles used by them are an order of magnitude lighter than water, and minimize the effects of gravity compared to capillarity. Their experimental results are completely consistent with the predictions of Poynting and Thompson: when the sphere and the wall are alike with respect to wetting, say both are hydrophobic or hydrophilic, the wall and sphere attracts; when they are unlike the sphere and wall repel.

There are only a few theoretical studies of capillary attraction. Nicolson 1949 was the first to derive an analytical expression for the capillary force between two floating bubbles by using the superposition approximation to solve the Laplace equation of capillarity. A similar approximate method was applied by Chan et al. 1981 to floating spheres and horizontal cylinders. For horizontal cylinders the alternative approaches were proposed by Gifford and Scriven 1971 and by Fortes 1982. The theoretical works are based on solutions of the Laplace equations for capillary menisci with translational or rotational symmetry, where the Laplace equation reduces to an ordinary differential equation. Saif 2002 constructed an interesting analysis of the capillary interaction of long plates with round ends at prescribed heights which do not float.

For the case where the meniscus slope and the particle size are small, the Laplace equation for the interface shape was solved using bipolar coordinates by Krahshesky, et al. 1992, 1993. This solution provides expressions for calculating the capillary meniscus force between two vertical disks, between two spheres partially immersed in a liquid layer and between a vertical disk and a sphere. Specifically, Kralchevsky and Nagayama 2000 have shown that the lateral force F_l acting on particles of radii R_1 and R_2 separated by distance L is equal in magnitude and opposite in sign and is given by

$$F_l = -2\pi Q_1 Q_2 q K_1(qL)\left[1 + O(q^2 R_k^2)\right] \text{ when } L >> r_k. \qquad (II.17)$$

Here $r_k = R_k \sin(\theta_c)$, k=1, 2 are the radii of the two contact lines as shown in figure II.7 (where the particle radius is assumed to be R), $Q_k = r_k \sin\psi_k$, where ψ_k is the interface slope with the horizontal plane at the point of contact, $q = \sqrt{(\rho_l - \rho_p)g/\gamma}$ is the inverse of the capillary length, $K_1(x)$ is the modified Bessel function of the first order. (II.17) is valid for particles much smaller than the capillary length. The force acting between two floating particles decreases with increasing distance them.

The analysis just given is useful for determining the parameter values for which the particles can remain trapped on two-fluid interfaces, as well as the sign and magnitude of forces that act between two suspended particles, but to understand the actual motion of particles on the interface we must solve the governing equations of motion. Since the governing equations are complex, the dynamic behavior of fluid and particles is not well understood.

A small number of theoretical studies have looked at the drag and diffusion coefficient of a spherical particle attached to a fluid interface (Brenner and Leal 1978, 1982; Goldman, Cox and Brenner 1967; Schneider, O'Neill and Brenner 1973; Majumdar, O'Neill and Brenner 1974 and Wakiga 1957; Redoev, Nedjalkov and Djakovich 1992; Danov, Aust, Durst and Lange 1995). Brenner and Leal have shown that the drag F_D acting on a floating sphere in the zero Reynolds number limit is $F_D = 3\pi\eta D U_x f_D$, where U_x is the lateral velocity of the sphere, D is the diameter, f_D is the drag coefficient which is O(1) and depends on the ratio of viscosities of the upper and lower fluids.

The only experimental study for determining drag coefficients of floating particles is by Petkov, Denkov, Danov, Velev, Aust and Durst 1995. They calculated the drag coefficients for particles of sub-millimeter radius by measuring the particle velocity under the action of a well defined external force. They showed that the capillary interactions are quite strong and very long range. Danov, Aust, Durst and Lange 1995 performed numerical simulations to obtain the drag coefficients for floating spheres, but they assumed that the interface between the two fluids stays flat and the particle translates with a constant velocity along the interface.

To understand the dynamics of clustering and self assembly of particles due to capillarity, we have developed a numerical package which treats the problem by direct numerical simulation. The method is as exact as numerical methods allow; in particular, the changing shape of the meniscus and the hydrodynamic forces which move particles are computed and not modeled. At each time step, we solve the governing mass and momentum conservation equations for the two fluids, compute the forces acting on the particles and then move them using Newton's equations for rigid solids. The interface shape changes in response to the fluid motion while satisfying the contact angle or contact line requirement on the particle surface. In addition, across the interface the fluid properties change suddenly and a capillary force acts between the two fluids.

We have performed dynamic simulations of spherical particles for which the contact angle is maintained at the equilibrium value and the position of the contact line changes, as well as for floating disks with sharp edges. For floating disks, the meniscus remains pinned at the rim even when the disk moves relative to the interface, but the contact angle at the rim changes. In our numerical study it is assumed that the interface is initially flat and the top surface of the disk is in the plane of the interface. As the disk is denser than the liquid, it sinks but the contact line remains at the rim. Consequently, the interface near the rim becomes more vertical increasing the vertical component of the capillary force. In our code, the contact line is kept at the sharp edge of a floating cylindrical particle by making the level set function vanish on the rim.

In the next section we will state the governing equations for the fluids and the particles, briefly describe the level set and distributed Lagrange multiplier approaches and present our finite element method. A detailed description of the numerical method is included in the appendix. In section VI, we will discuss the convergence study that shows that the numerical results are independent of the mesh size as well as the time step size and present results for the transient motion of particles along two-fluid interfaces.

IV. Governing Equations and dimensionless groups

In our numerical studies of particle motion in two-fluid interfaces we will assume that the fluids are immiscible and Newtonian. The particles are assumed to be rigid. Let us denote the domain containing the two liquids and N particles by Ω, the domain boundary by Γ_d, and the interior of the ith particle by $P_i(t)$. The governing mass and momentum conservation equations for the fluid phases can be written as

$$\rho\left[\frac{\partial \mathbf{u}}{\partial t} + \mathbf{u}.\nabla\,\mathbf{u}\right] = \rho\,\mathbf{g} - \nabla p + \nabla.\sigma + \gamma\,\kappa\,\delta(\phi)\,\mathbf{n};\ \nabla\cdot\mathbf{u} = 0 \quad \text{in } \Omega\backslash\overline{P(t)} \qquad \text{(IV.1)}$$

$$\mathbf{u} = \mathbf{u}_L \qquad \text{on } \Gamma_d \qquad \text{(IV.2)}$$

$$\mathbf{u} = \mathbf{U} + \boldsymbol{\omega} \times \mathbf{r} \qquad \text{on } \partial P(t) \tag{IV.3}$$

with the extra stress tensor $\boldsymbol{\sigma} = 2\eta\mathbf{D}$, ρ is the fluid density which is different for the two fluids, p is the pressure, **D** is the symmetric part of the velocity gradient tensor, $\delta(.)$ is the Dirac delta function, **n** is the outer normal at the interface, γ is the surface tension, κ is the mean surface curvature, ϕ is the distance from interface, η is the viscosity which is different for the two fluids and $\mathbf{u}_L$ is the prescribed velocity on Γ_d. The surface tension force acts along the interface between the two fluids.

The particle velocity **U** and angular velocity $\boldsymbol{\omega}$ are governed by

$$M\frac{d\mathbf{U}}{dt} = M\mathbf{g} + \mathbf{F} \tag{IV.4}$$

$$\frac{d(\mathbf{I}_P\,\boldsymbol{\omega})}{dt} = \mathbf{T} \tag{IV.5}$$

$$\mathbf{U}\,|_{t=0} = \mathbf{U}_0$$

$$\boldsymbol{\omega}\,|_{t=0} = \boldsymbol{\omega}_0 \tag{IV.6}$$

where M and $\mathbf{I}_P$ are the mass and moment of inertia of the particle. The particle density is denoted by ρ_P. The force **F** acting on a particle in the above equations is

$$\mathbf{F} = \oint(-p\mathbf{I} + \boldsymbol{\sigma}).\mathbf{n}\, dA + \oint_{C.L.} \boldsymbol{\Gamma}\, ds \tag{IV.7}$$

The first term on the right of (IV.7) is the force on the particle due to stresses generated by fluid motion; the second term

$$\oint_{C.L.} \boldsymbol{\Gamma}\, ds = \gamma \oint_{C.L.} \mathbf{n}_c\, ds \tag{IV.8}$$

is the capillary force, $\boldsymbol{\Gamma} = \gamma\mathbf{n}_c$ is a line stress on the contact line (C.L.) and $\mathbf{n}_c$ is the capillarity unit vector which lies in the interface and is normal to the contact line. This unit vector gives the direction of the action of the capillary force. A numerical algorithm for constructing $\mathbf{n}_c$ is given in section 5. Similarly, the torque **T** acting on the particle is given by

$$\mathbf{T} = \oint(\mathbf{x} - \mathbf{X}) \times [(-p\mathbf{I} + \boldsymbol{\sigma}).\mathbf{n}]\,dA + \oint_{C.L.} (\mathbf{x} - \mathbf{X}) \times \boldsymbol{\Gamma}\, ds\,. \tag{IV.9}$$

Here **X** is the center of particle, the first term gives the torque due to the fluid stress and the second due to the capillary force acting on the contact line. For a spherical particle, which is one of the cases considered in this paper, if the interfacial tension γ is constant, the torque due to the interfacial tension is zero (see Singh and Hesla 2003).

The shape of the meniscus must be compatible with conditions which are prescribed at the contact line on every particle and at remote boundaries; for spherical particles the contact angle α is prescribed (see figure II.7), but the contact line evolves during motion. For disks hanging at the sharp edge, the position of the contact line is prescribed and the contact angle changes. At remote boundaries different conditions could be considered, but in our simulations we have required the interface to be flat there. The motion of particles in fluid interfaces is very complex because the prescribed value of the contact angle is to be applied at the contact lines whose positions cannot be prescribed a *priori* and at the sharp edges the contact angle is not known a *priori*.

A particle placed in a two-fluid interface can be in a state of equilibrium provided its buoyant weight is equal to the z-component of capillary force. The capillary force changes when the particle sinks or rises or the interface deforms to satisfy the contact angle requirement. Clearly, for a particle moving laterally along the interface, the vertical acceleration is small, and thus the z-component of (IV.4) is

$$0 = -Mg + \mathbf{k}\cdot\oint(-p\mathbf{I}+\boldsymbol{\sigma}).\mathbf{n}\,dA + \gamma\oint_{C.L.}\mathbf{k}\cdot\mathbf{n}_c\,ds, \tag{IV.10}$$

where **k** is the unit vector in the z-direction. The last term of (IV.14) is the vertical projection of the capillary force which depends on the contact angles. For isolated spheres or disks in equilibrium (IV.10) and the vertical projection of (IV.1) with **u**=0 reduce to equation (II.5) or (II.8).

The x-component of particle momentum equation, which governs its lateral motion, can be written as

$$M\frac{d\mathbf{U}_x}{dt} = \mathbf{i}\cdot\oint(-p\mathbf{I}+\boldsymbol{\sigma}).\mathbf{n}\,dA + \gamma\oint_{CL.}\mathbf{i}\cdot\mathbf{n}_c\,ds. \tag{IV.11}$$

where **i** is the unit vector in the x-direction. The first term on the right hand side is the x-component of fluid stress and the second is the x-projection of the integral of $\mathbf{n}_c$ around the contact line.

If we assume that a particle is accelerating slowly, which is the case, for example, when the two attracting particles are far from each other, then the two terms on the right hand side of (IV.11) balance each other. In the low Reynolds number limit, Brenner and Leal expressed the drag F_D acting on a sphere moving along the interface as

$$F_D = 3\pi\eta_L D U_x f_D \tag{IV.12}$$

where f_D is the drag coefficient which is of order one and depends on the viscosity ratio of the two fluids, the contact angle and the deformation of the interface which in turn depends on the density of the particle. Under these approximations, equations (IV.11) and (IV.12) give

$$0 = 3\pi\eta_L D U_x f_D + \gamma\oint_{CL.}\mathbf{i}\cdot\mathbf{n}_c\,ds. \tag{IV.13}$$

Equation (IV.13) can be solved to obtain the lateral velocity U_x of the particles; U_x is proportional to $\frac{\gamma}{\eta_L}$, the "capillary velocity" scale.

Petkov, Denkov, Danov, Velev, Aust and Durst 1995 used (IV.13) for estimating the drag coefficient for floating spherical particles attracted by a plate. They measured U_x in an experiment and used the analytical expression for the horizontal force obtained by Kralchevsky, Paunov, Denkov, and Nagayama 1994 which is related to the integral term in the above expression. They found that the drag coefficient depends on the viscosities of the upper and lower fluid, as was shown by Brenner and Leal. The experimental values of the drag coefficient for several fluid-particle combinations were found to be of O(1). The drag coefficient was greater than one for heavy particles, since they cause a greater deformation of the interface. They estimated the drag coefficients when the distance between the particle and the plate was greater than 35R, where R is particle radius; for smaller distances (IV.17) is not accurate because the inertial effects are not negligible. The estimate of the lateral capillary force they used is accurate only when the distance between the particle and the plate is large.

Danov, Aust, Durst and Lange 1995 performed numerical simulations to study the dependence of the drag on a spherical particle translating in the interface on the ratio of viscosities. In their simulations, it is assumed that the interface between the two fluids is flat and the particle velocity is constant. They found that the agreement with experiments deteriorates with increasing particle density because interfacial deformation is not negligible.

In this paper we study problems for which inertial effects and time dependent changes in the interface shape in response to particle motion are important. This happens to be the case when the distance between two floating particles is of the order of the particle radius because the interface shape changes continuously and the particles accelerate as they move toward each other.

The buoyant weight of particles is an important quantity in the description of the dynamics of capillary attraction. To see how it enters, we first express gravity as a potential

$$\mathbf{g} = -\mathbf{k}g = -g\nabla z \tag{IV.14}$$

and write

$$\rho\mathbf{g} - \nabla p = -\nabla\hat{p} \tag{IV.15}$$

where

$$\hat{p} = p + \rho g z \tag{IV.16}$$

In (IV.1), the interface is given by

$$z=h(x,y,t) \tag{IV.17}$$

The contact line can be specified by z_c, where h intersects the particle surface. Using (IV.16), we find the pressure force acting on the particle

$$\begin{aligned}\oint p\mathbf{n}dA &= \oint(\hat{p} - \rho g z)\mathbf{n}dA \\ &= \oint\hat{p}\mathbf{n}dA - \rho_U V_U g - \rho_L V_L g \end{aligned} \tag{IV.17}$$

where V_U is the volume of the particle above and V_L is the volume below the contact line and $M=\rho_P g(V_U + V_L)$. We may now write (IV.4) as

$$M\frac{d\mathbf{U}}{dt} = \left[(\rho_P - \rho_U)V_U + (\rho_P - \rho_L)V_L\right]g\,\mathbf{k} + \oint(-\hat{p}\mathbf{I} + \boldsymbol{\sigma}).\mathbf{n}\,dA + \gamma\oint_{C.L.}\mathbf{n}_c\,ds\,. \tag{IV.18}$$

The first term on the right hand side of (IV.18) is only a portion the buoyant weight (see equation (II.3)). For isolated spheres, with a prescribed contact angle, the contact line will be a circle on the sphere, so that the unknowns are V_U, V_L and z_c=h(x,y,t). For the disk hanging on the sharp rim, V_U=0, V_L=V and the contact angle are ψ unknown. Equation (IV.5) can be written as

$$\frac{d(\mathbf{I}_P\,\boldsymbol{\omega})}{dt} = \oint(\mathbf{x}-\mathbf{X})\times\left[((-\hat{p}+\rho gz)\mathbf{I}+\boldsymbol{\sigma}).\mathbf{n}\right]dA + \gamma\oint_{C.L.}(\mathbf{x}-\mathbf{X})\times\mathbf{n}_c\,ds \tag{IV.19}$$

The scaling parameters for equations (IV.1)-(IV.1), (IV.18) and (IV.19) are

[D, U, D/U, η_LU/D, U/D, ρ_L] = [diameter, velocity, time, stress, angular velocity, density]. (IV.20)

Here η_L and ρ_L are the viscosity and density of the lower liquid and D=2R is the diameter of the sphere or disk. The dimensionless equations are then in the form

$$l\left[\frac{\partial\mathbf{u}}{\partial t} + \mathbf{u}.\nabla\,\mathbf{u}\right] = -\nabla\hat{p} + \frac{1}{Re}\nabla.\boldsymbol{\sigma} + \frac{1}{We}\,\kappa\,\delta(\phi)\,\mathbf{n};\ \nabla\cdot\mathbf{u} = 0 \qquad \text{in } \Omega\backslash\overline{P(t)} \tag{IV.21}$$

$$\frac{Re\,l_p}{\beta}\frac{d\mathbf{U}}{dt} = -G\,Re\left((l_P - l_U)V_U + (l_P - 1)V_L\right)\mathbf{k} + \oint(-\hat{p}\mathbf{I} + \boldsymbol{\sigma}).\mathbf{n}\,dS + \frac{1}{Ca}\oint_{C.L.}\mathbf{n}_c\,ds \tag{IV.22}$$

$$\frac{Re\,l_p}{\beta}\,\frac{d\mathbf{I}'_P\,\boldsymbol{\omega}}{dt} = \oint(x-X)\times\left[((-\hat{p} + \frac{\rho gzD}{\eta_L U})\mathbf{I} + \boldsymbol{\sigma}).\mathbf{n}\right]ds + \frac{1}{Ca}\oint_{C.L.}(\mathbf{x}-\mathbf{X})\times\mathbf{n}_c\,ds \tag{IV.23}$$

where **k** is the unit vector along the z-direction. The particle mass $M=\frac{\rho_P D^3}{\beta}$, where $\beta = \frac{6}{\pi}$ for a sphere and $\beta = \frac{4D}{\pi h}$ for a disk with *h* being the disk height. The particle moment of inertia $\mathbf{I}_P = M\,\mathbf{I}'_P D^2$, where $\mathbf{I}'_P$ is the dimensionless moment of inertia. It can be shown that the term proportional to ρgz in (IV.23) vanishes when the particle is a sphere, but does not vanish when the particle is a disk.

The dimensionless parameters which define the motion of particles are

$$[Re, G, Ca] = \left[\frac{\rho_L UD}{\eta_L}, \frac{gD}{U^2}, \frac{\eta_L U}{\gamma}\right]$$

= [Reynolds, gravity, capillary] numbers (IV.24)

and the property ratios

$$[l, l_{\mathrm{p}}, l_{\mathrm{U}}, m]=[\frac{\rho}{\rho_{\mathrm{L}}}, \frac{\rho_{\mathrm{P}}}{\rho_{\mathrm{L}}}, \frac{\rho_{\mathrm{U}}}{\rho_{\mathrm{L}}}, \frac{\eta_{\mathrm{U}}}{\eta_{\mathrm{L}}}] \qquad \text{(IV.25)}$$

where the subscript 'L' refers to the lower liquid and 'U' to the upper liquid. The density parameter l is equal to one in the lower liquid and in the upper fluid it is $\frac{\rho_{\mathrm{U}}}{\rho_{\mathrm{L}}}$ and the Weber number We =Re Ca. In our numerical we use the dimensional equations (IV.1)-(IV.4) where the hydrostatic pressure variation is not removed from the pressure.

The selection of a characteristic velocity U for the definition of the dimensionless parameters in (IV.20) is ambiguous since a characteristic velocity is not prescribed in data. A natural choice for the velocity is the capillary velocity $U=\frac{\gamma}{\eta_{\mathrm{L}}}$, which is suggested by other problems of motion driven by surface tension. With this choice we may compute

$$[\mathrm{Re}, \mathrm{G}, \mathrm{Ca}] = \left[\frac{\rho_{\mathrm{L}}\gamma D}{\eta_{\mathrm{L}}^{2}}, \frac{g\eta_{\mathrm{L}}^{2} D}{\gamma^{2}}, 1\right] \qquad \text{(IV.26)}$$

from the prescribed data.

V. Numerical Method

In this section we will briefly describe the key features of our numerical scheme. A detailed description of the numerical algorithm is included as an appendix.

To perform direct numerical simulation of the motion of rigid particles trapped in a two-fluid interface, we must solve the governing mass and momentum conservation equations for the two fluids, compute the forces acting on the particles and then move them using Newton's equations (IV.4). This is a difficult task because the interface shape changes as the particles move and the capillary force between the two fluids must be computed subject to the constraint that the contact angle is prescribed on a smooth surface and the contact line is prescribed on edges.

In this study we will assume that the dynamic contact angle is the same as the static contact angle. This enforcement of the contact angle on the particle surface causes the contact line to move which may be described as a capillary induced motion of the contact line due to a prescribed contact angle (see Friedrichs and Guceri 1993 and Sussman 2001 and references therein). At sharp edges, the motion of the particles is computed under the constraint that the interface remains pinned to the sharp edges of particles so that the contact angle changes as the motion proceeds. The contact angle can vary within the limits specified by the Gibbs extension of the Young-Dupré law.

In this work the level set method is used to track the interface (see Osher and Sethian 1988, Sussman, Smereka and Osher 1994, Pillapakkam and Singh 2001, Sussman 2001). The level set method works efficiently on a regular fixed grid and is compatible with the distributed Lagrange multiplier method (DLM) which will be used to track the motion of rigid particles (see Glowinski, Pan, Hesla and Joseph 1999 and Singh, Joseph, Hesla, Glowinski and Pan 2000). The DLM method also works efficiently on regular fixed grids. There are several other numerical approaches available for tracking the interface between two immiscible liquids, e.g., the surface tracking method (Unverdi and Tryggvason 1992), the volume of fluid method (Hirt and Nichlos 1981), the moving grid methods (Glowinski, Tallec, Ravachol and Tsikkinis 1992) and the mapping method (Ryskin and Leal 1984) that can be used with the DLM method to study dynamics of floating particles.

In the level set method, the interface position is not explicitly tracked, but is defined to be the zero level set of a smooth function ϕ, which is assumed to be the signed distance from the interface. In order to track the interface, the level set function is advected according to the velocity field. One of the attractive features of this approach is that the method does not require any special treatment when a front splits into two or when two fronts merge.

The key idea in the level-set method is to advect ϕ with the local velocity, i.e.,

$$\frac{\partial \phi}{\partial t} + \mathbf{u}.\nabla \phi = 0\,. \tag{V.1}$$

As ϕ is a smooth function, it is relatively easy to numerically solve the above equation to update the interface position. In our implementation, it is assumed to be negative for the upper fluid, positive for the lower fluid and zero along the interface. The method also allows us to enforce the contact angle on the rigid particle surfaces and it is relatively easy to implement it in both two and three dimensions.

The motion of particles is tracked using a distributed Lagrange multiplier method (DLM). One of the key features of the DLM method is that the fluid-particle system is treated implicitly by using a combined weak formulation where the forces and moments between the particles and fluid cancel, as they are internal to the combined system. The flow inside the particles is forced to be a rigid body motion using the distributed Lagrange multiplier method. This multiplier represents the additional body force per unit volume needed to maintain rigid-body motion inside the particle boundary, and is analogous to the pressure in incompressible fluid flow, whose gradient is the force needed to maintain the constraint of incompressibility.

In our numerical scheme the Marchuk-Yanenko operator splitting technique is used to decouple the difficulties associated with the incompressibility constraint, the nonlinear convection term, the rigid body motion constraint and the interface motion. The operator-splitting gives rise to the following four sub-problems: a L^2 projection problem for the velocity and the pressure; a nonlinear advection-diffusion problem for the velocity; a distributed Lagrange multiplier problem that forces rigid body motion within the particles; and an advection problem for the interface. Details of this method are set down in the appendix.

V.1 Reinitialization of ϕ

The level set function ϕ is reinitialized to be a distance function after each time step by solving the following equation obtained in Sussman, et al. 1994 to the steady state

$$\frac{\partial \phi}{\partial t} + \mathbf{w}.\nabla\phi = S(\phi_0) \qquad \text{(V.2)}$$

where ϕ_0 is the distribution to be reinitialized and

$$\mathbf{w} = S(\phi_0)\frac{\nabla\phi}{|\nabla\phi|}.$$

Here $S(\phi_0)$ is the sign function, i.e., $S(\phi_0) = 1$ if $\phi_0 > 0$ and $S(\phi_0) = -1$ if $\phi_0 < 0$. In order to avoid discontinuities, in our code we use the following smoothed sign function

$$S(\phi_0) = \frac{\phi_0}{\sqrt{\phi_0^2 + h_e^2}},$$

where h_e is equal to one and half times the element size. Equation (V.2) is a first order hyperbolic partial differential equation which is solved using a positive only upwinding scheme described in Singh and Leal 1993. Clearly, the characteristics of (V.2) point in the direction of **w**. Therefore, for the points inside the upper fluid **w** points upwards away from the interface and for the points inside the lower fluid it points downwards. Thus, (V.2) can be solved by specifying the boundary condition $\phi = \phi_0$ at the two-fluid interface $\phi = 0$.

V.2 Variation of fluid properties across the interface

In our finite element scheme the fluid viscosity is assumed to jump across the interface, i.e.,

$$\eta = \begin{cases} \eta_L & \text{if } \phi > 0 \\ 0.5(\eta_L + \eta_U) & \text{if } \phi = 0 \\ \eta_U & \text{if } \phi < 0. \end{cases} \qquad \text{(V.3)}$$

Here η_L and η_U are the viscosities of the lower and upper fluids, respectively. The fluid density, on the other hand, is assumed to vary smoothly across the interface

$$\rho = \begin{cases} \rho_L & \text{if } \phi > h_e \\ \rho_U & \text{if } \phi < -h_e \\ 0.5(\rho_L + \rho_U) + 0.5(\rho_U - \rho_L)\ \sin\left(\dfrac{\pi\phi}{2h_e}\right) & \text{otherwise} \end{cases} \qquad \text{(V.4)}$$

where h_e is equal to one and half times the element size, and ρ_L and ρ_U are the densities of the two fluids, respectively. This smoothing of the density is similar to that used by Sussman, et al. 1994, and is needed for avoiding numerical instabilities when the density ratio ρ_L/ρ_U is large.

The surface tension force is smoothed and acts only on the elements for which ϕ is smaller than h_e. This is done by approximating $\delta(\phi)$ in (IV.1) by a mollified delta function $\delta_{h_e}(\phi)$ using the approach described in Sussman, et al. 1994:

$$\delta_{h_e}(\phi) = \begin{cases} \dfrac{1+\cos(\pi\phi/h_e)}{2h_e} & \text{for } |\phi| < h_e \\ 0 & \text{otherwise} \end{cases} \qquad \text{(V.5)}$$

The error introduced by smoothing of the surface tension force is $O(h_e)$. Equations (V.4) and (V.5) require that ϕ be maintained as a distance function which we do in our implementation by reinitializing ϕ after each time step.

V.3 Contact angle and contact line conditions

The contact angle boundary condition on the particle surface, $\mathbf{n}.\mathbf{n}_\phi = \cos\alpha$, where $\mathbf{n}$ is the unit outer normal on the particle surface and $\mathbf{n}_\phi = \dfrac{\nabla\phi}{|\nabla\phi|}$ is normal to the interface, is enforced using the approach described in Sussman 2001. Sussman used this approach to prescribe the contact angle on a stationary flat wall by extending ϕ to the "outside" of the fluid domain. In this article the same approach is used to prescribe the contact angle of the two-fluid interface on the surface of a moving sphere. Let us define $\mathbf{t}$ and $\mathbf{n}_2$ as

$$\mathbf{t} = \frac{\mathbf{n}_\phi \times \mathbf{n}}{|\mathbf{n}_\phi \times \mathbf{n}|}, \ \mathbf{n}_2 = \frac{\mathbf{t} \times \mathbf{n}}{|\mathbf{t} \times \mathbf{n}|}.$$

Notice that $\mathbf{t}$ is tangent to the contact line, and thus $\mathbf{n}_2$ is orthogonal to the contact line and lies in the tangent plane of the particle surface (see figure V.1a). The next step is to construct a unit vector $\mathbf{u}_{ex}$ which is tangent to the interface with contact angle α, points inwards, and lies in the plane formed by $\mathbf{n}$ and $\mathbf{n}_2$;

$\mathbf{n}_c = -\mathbf{u}_{ex}$ is the unit vector which gives the direction of the action of the capillary force. It is easy to verify that $\mathbf{u}_{ex}$ depends on $c = \mathbf{n}_\phi.\mathbf{n}_2$ and is given by

$$\mathbf{u}_{ex} = \begin{cases} \dfrac{\mathbf{n} - \cot(\pi-\alpha)\,\mathbf{n}_2}{\left|\mathbf{n} - \cot(\pi-\alpha)\,\mathbf{n}_2\right|} & \text{if } c < 0 \\ \dfrac{\mathbf{n} + \cot(\pi-\alpha)\,\mathbf{n}_2}{\left|\mathbf{n} + \cot(\pi-\alpha)\,\mathbf{n}_2\right|} & \text{if } c > 0 \\ \mathbf{n} & \text{if } c = 0 \end{cases} \tag{V.6}$$

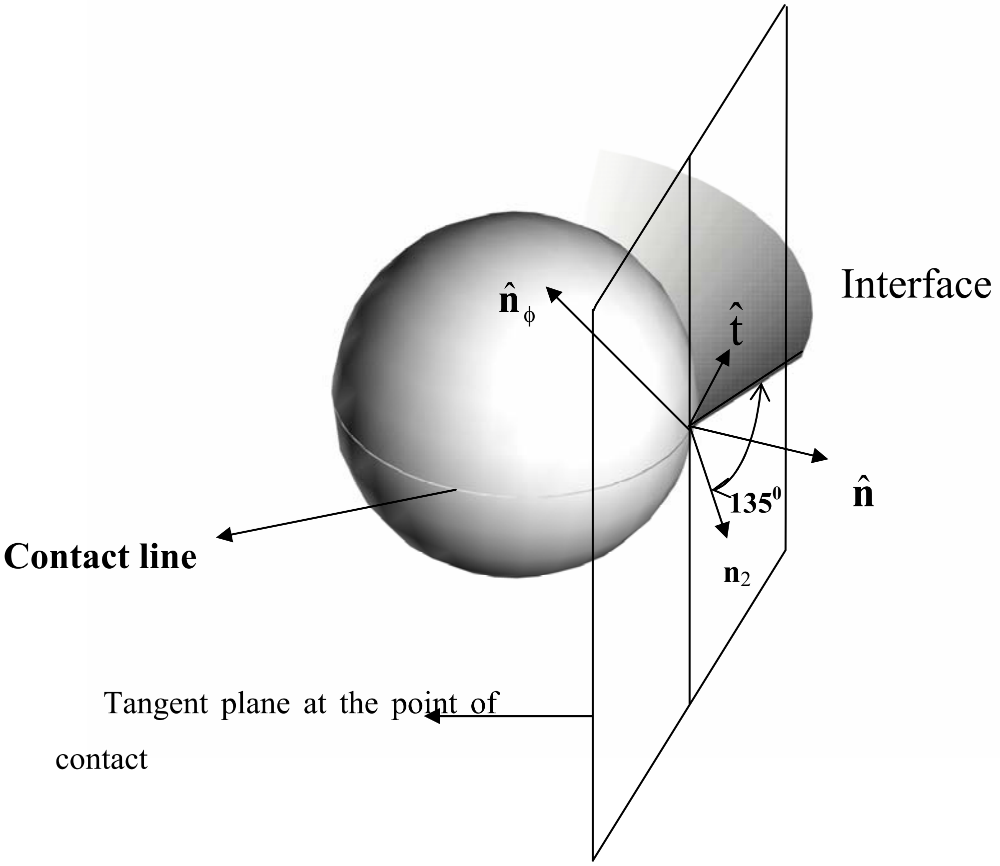

V.1(a)

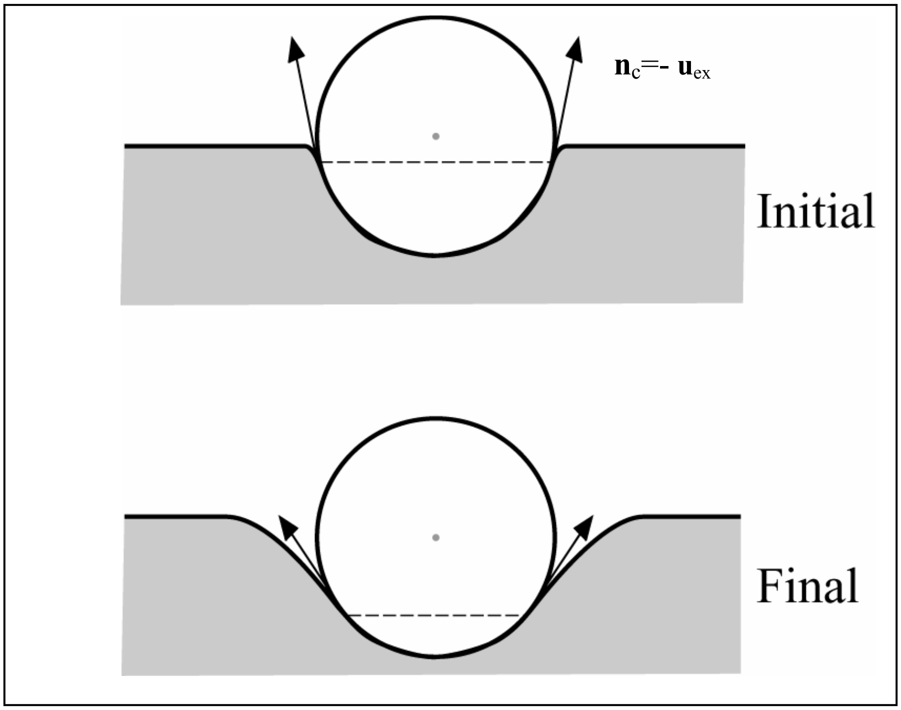

V.1(b)

Figure V.1. (a) The unit normal to the particle surface **n**, *the tangent to the contact line* **t** *and the normal to the interface* $\mathbf{n}_\phi$ *are shown. (b) A schematic of the interface shape and the contact line are shown for the initial and steady states. In simulations the contact angle on the particle surface is prescribed to be 135º which is done by extending the level set function to the inside of the particle. The contact line moves downwards because of the interface deformation near the particle and this decreases the vertical component of capillary force.*

To enforce the prescribed contact angle, ϕ is extended inside particles and on their surfaces by solving

$$\frac{\partial \phi}{\partial t} + \mathbf{u_{ex}}.\nabla\phi = 0\,. \qquad \text{(V.7)}$$

In other words, for all nodes inside and on the particle surface (V.7) is used to modify ϕ. The resulting extended level set function satisfies the contact angle on the particle surface.

The contact line on the particle surface moves when the contact angle is enforced using (V.7). This could be called the capillary induced motion of the contact line due to a prescribed contact angle. This approach has been used in many past numerical studies of problems involving moving contact lines (see Friedrichs and Guceri 1993 and Sussman 2001 and references therein). For example, in the injection molding problems this approach has been used to track the motion of liquid front advancing into empty molds.

Clearly, this motion of the contact line on the particle surface is in conflict with the no slip condition for viscous fluids (see Dussan and Davis 1974, Dussan 1976 and Kistler and Scriven 1993 and references therein). However, if the contact line position on the particle surface is not updated, the contact line cannot move. In the capillary induced motion approach the no slip condition is satisfied before and after the contact line moves; this pragmatic procedure could be called an effective numerical slip. This method of moving the contact line when the contact angle is prescribed has been used by Friedrichs and Guceri 1993 and Sussman 2001. An alternative approach used in some studies is to use a slip condition in a small neighborhood of the contact line to ensure that it moves (see Kamal, Goyal and Chu 1988 and references therein). The slip velocity of the contact line is assumed to be proportional to the shear stress on the wall. This approach however does not ensure that the contact angle remains constant. Another aspect of the floating particle problem not treated here is that the contact angle for advancing and receding contact lines is different which can change the dynamical behavior of floating particles.

VI. Initial value problems for the evolution of floating particles to equilibrium

Here we report results of simulations of initial value problems for sphere and disks which are initially motionless, but not in equilibrium, to an equilibrium in which they are again motionless. The particles are heavier than the heavy liquid below and they float. Initially, the particles are motionless and imbedded in a flat interface; the spheres are centered with their midplane in the interface and the contact angle fixed and held at 135º throughout the simulation. The assumed value of the contact angle is likely to be insensitive to the contact line speed in real experiments, as it is relatively large. Disks are pinned at the sharp edge of the upper rim throughout the simulation.

We do simulations for one sphere, one disk, two and four spheres and two disks. Initially, particles are not in equilibrium because they are heavy and must sink to equilibrium. For all cases, the particles reach an equilibrium in which they are motionless and in a balance between capillary forces and the buoyant weight; for single particles, spheres and disks, the computed values at equilibrium can be computed with the analytical expressions (II.5) and (II.8) and the agreement is satisfactory. The evolution to equilibrium for more than one particle takes place by sinking and capillary attraction; at the end the particles have self assembled.

The conditions under which spheres and disks evolve to equilibrium are different. The interface near the spheres adjusts to meet the contact angle requirement and they sink until the buoyant weight becomes equal to the vertical component of the capillary force. The disks, on the other hand, sink causing the interface to deform and increasing the contact angle and the vertical component of the capillary force. The disks stop sinking when the vertical component of the capillary force becomes equal to the buoyant weight.

An attractive force between floating particles arises because the meniscus between drops in much the same way as a water meniscus will sink in a hydrophobic capillary tube. This dropping of the meniscus inside relative to the outside produces an asymmetry which generates attractive capillary forces.

For spheres, since the contact angle is fixed, the contact line between the spheres drops. For disks, since the contact lines are fixed at the rim, the contact angles between the two disks decrease. In both cases, the asymmetry results in an attractive lateral capillary force to act on the particles.

The domains used in our simulations are box shaped with rectangular cross sections. The coordinate system used throughout this paper is shown in figure VI.1. The x-, y- and z-components of particle velocity will be denoted by u, v and w, respectively.

We will also assume that all dimensional quantities, unless otherwise noted, are in the CGS units. The lower fluid density ρ_L=1.0 gm/cm^3. The viscosity of the lower fluid, and the density and viscosity of the upper fluid are varied. The particle density is assumed to be greater than one. The values of the interfacial tension are selected to ensure that the particle remains suspended in the interface. The acceleration due to gravity g=981.0 cm/s^2 and acts along the negative z-direction. The initial velocities are assumed to be zero everywhere.

The no slip boundary condition is applied on the surface of the box shaped computational domains. The contact angle between the interface and the box boundaries is assumed to be 90^o, the interface near the walls is flat.

We next present the results for floating spheres and disks, to demonstrate that the scheme works correctly, and that it reproduces the expected dynamical behavior and the equilibrium state.

VI.1 Initial value problems for floating spheres

In this subsection, we compute the motion of spheres released in the interface; the contact line intersects the sphere[1] at a place different than one required for equilibrium. The sphere diameter is assumed to be 0.2 cm. The initial interface shape is flat, except near the sphere surface where a contact angle of 135^o is prescribed (see figure V.1). The parameters are in the range for which a sphere trapped on the interface can be in equilibrium. The equilibrium interface shape and the floating height depend on the problem parameters.

VI.1.1 Motion of a single sphere

When a sphere is suddenly released in the interface, the meniscus shape evolves to equilibrium. During this time, the velocity field in the two fluids is non-zero and the capillary force acting on the particle varies; the sphere velocity and its position in the interface change with time. The final equilibrium

---

[1] If the initial particle position was such that the interface did not touch the particle surface, then we would also need to address the problem of an interface coming in contact with a solid surface. This would require us to include additional physics to specify the conditions under which an interface can touch a solid surface. This physics is not included in the current version of our code.

position described by analytical expression (II.5), however, is independent of these transients and can be used to verify the accuracy of numerical results.

We first present results that show that the trajectory of a sphere released in the two-fluid interface is independent of the mesh resolution and the time step. We have used two regular tetrahedral meshes to show that the results converge with mesh refinement. In a tetrahedral element there are seven velocity and four pressure nodes. The rigid body constraint inside particles is enforced using uniformly distributed collocation points. The number of velocity nodes and elements in the first mesh are 117,649 and 13,824, respectively. In the second mesh, referred to as mesh B, there are 274,625 velocity nodes and 32,768 elements. The time step for these simulations is 0.0001, 0.00005 or 0.000025.

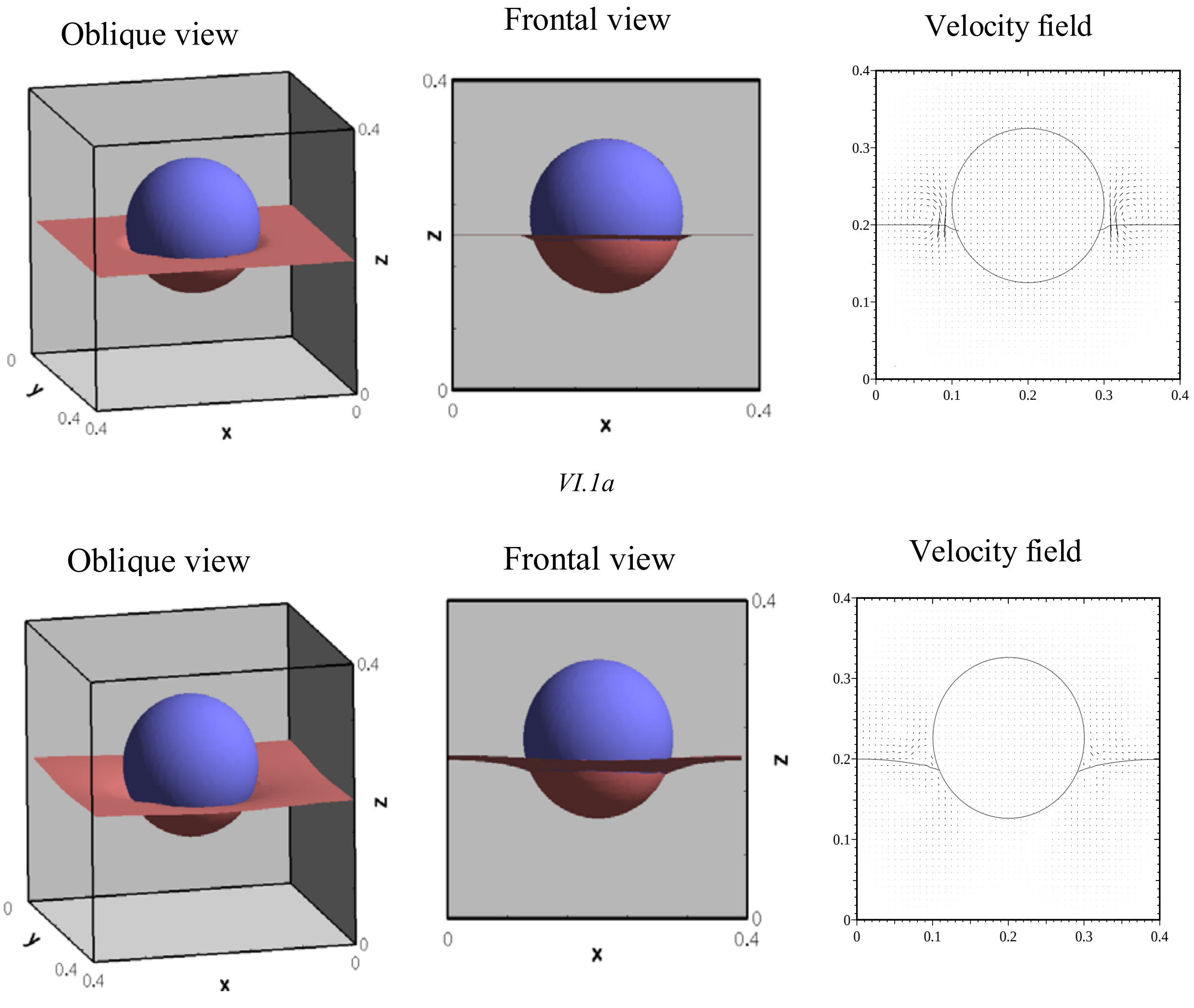

VI.1a

VI.1b

***Figure** VI.1. The particle position and the interface shape and the velocity field in the domain midsection are shown. The length of velocity vectors is magnified 30 times. The length of the velocity vectors in (b) is smaller indicating that the fluid velocity decreases with time. The oblique and side views are shown. (a) t=0.003. The fluid velocity is* *largest near the contact line where the interface curvature is large, (b) t=0.08. The dimensionless parameters based on the maximum particle velocity are (Re=0.064, G=1916.0, Ca=0.02) and based on the capillary velocity are (Re=3.2, G=0.766).*

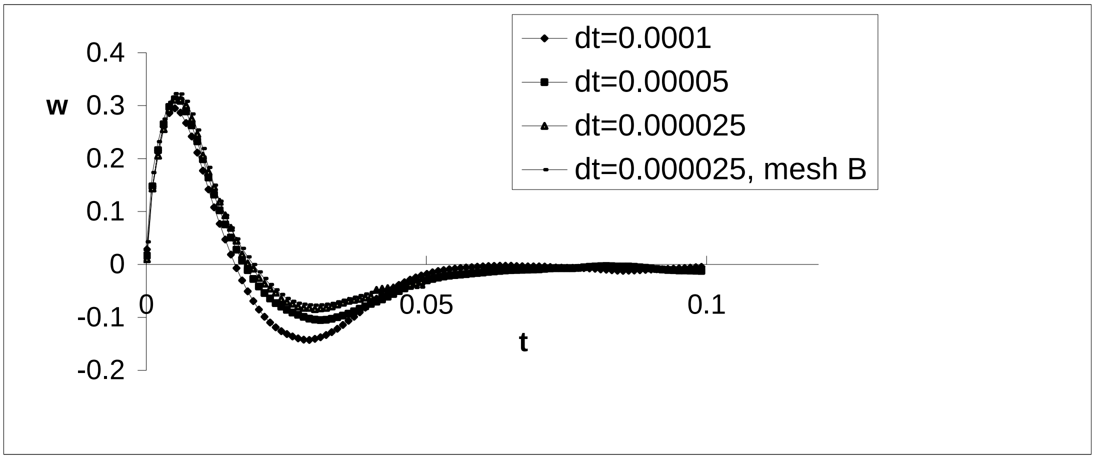

Figure VI.2. The vertical component of sphere velocity w released from rest on the interface is shown as a function of time for three different values of the time step. The curve marked mesh B is for a more refined mesh. The density and viscosity of the lower fluid are 1.0 gm/cm^3 and 1.0 Poise, and those of the upper fluid are 0.1 gm/cm^3 and 0.1 Poise. The interfacial tension is 16.0 dynes/cm and the particle density is 1.05 gm/cm^3.

The sphere density is 1.05 gm/cm^3 and the interfacial tension is 16.0 dynes/cm. For the upper fluid density is 0.1 gm/cm^3 and the viscosity is 0.1 Poise. The initial velocity distribution in the fluid, and the sphere's linear and angular velocities are assumed to be zero. The domain is assumed to cubical with sides 0.4 cm. The sphere center is at a distance of 0.02 cm above the undeformed interface which passes though the domain center.

In figure VI.2, w is plotted as a function of time for three time steps and two mesh resolutions. When the time step is reduced or when the mesh is refined the variation of w with time remains approximately the same. This allows us to conclude that the numerical results converge with both mesh and time step refinements.

Figure VI.2 shows that the vertical component of the sphere velocity w increases for t<~0.005 s and then it starts to decrease; it becomes negative for t=~0.019 s and then increases again and becomes very small and fluctuates around zero for t>~0.06 s. The other components of velocity u and v remain small for all times. We will assume that for t=0.06 s the sphere has reached a state of equilibrium with h_2=0.156R and θ_c=65.26°. The computed values given in table VI.1 are in good agreement with the equilibrium formula (II.5). We may therefore conclude that the state of equilibrium is captured correctly by our code. The dimensionless parameters based on the maximum vertical velocity are: Re=0.064, Ca=0.02, G=1916.0 and We=1.28×10^{-3}.

Table VI.1. *The interfacial deformation h_2/R, the floating height $R \cos\theta_c$ from numerical computation are used to compute the sum of the pressure and vertical component of capillary forces from (II.1) and (II.3) for 5 values of the interfacial tension. The sphere density is 1.05 gm/cm^3 and its weight is 4.315 g cm/s^2. The density of lower fluid is 1.0 gm/cm^3 and that of the upper fluid is 0.1 gm/cm^3. For all five cases, $F_p + F_c$ is approximately equal to the particle weight; we get the correct value of the sphere weight from simulations. As expected, the sphere's floating height increases and the interface deformation decreases with increasing surface tension. The interfacial deformation for these calculations is restricted because the domain size is relatively small. But, we can still compare these values as the same domain is used for all interfacial tension values.*

γ (dynes/cm)	h_2/R	$R \cos\theta_c$ (cm)	θ_c (degrees)	$F_p + F_c$ (g cm/s^2)
10	0.237	0.257	75.00	4.33
14	0.173	0.376	67.95	4.35
16	0.156	0.419	65.26	4.35
20	0.130	0.466	62.28	4.36
25	0.114	0.514	59.07	4.33

To understand the initial increase in w, we notice that the angle θ_c giving the position of the contact line in figure VI.1a is larger than that for the equilibrium state shown in figure VI.1b (also see figure V.1b). Thus, the vertical component of capillary force is initially larger than the final value and as a result the particle moves upwards. This is a consequence of the fact that initially the interface is approximately flat everywhere except near the sphere (see figure VI.1a). The large curvature of the interface near the sphere at early times is reduced by interfacial tension and the interface assumes its equilibrium shape. The contact line moves downwards, reducing the vertical component of the capillary force. The vertical component of the pressure force in figures VI.1a and b are different, but since in the case shown in figure VI.1a the fluid velocity is not small, the pressure force cannot be determined using hydrostatics.

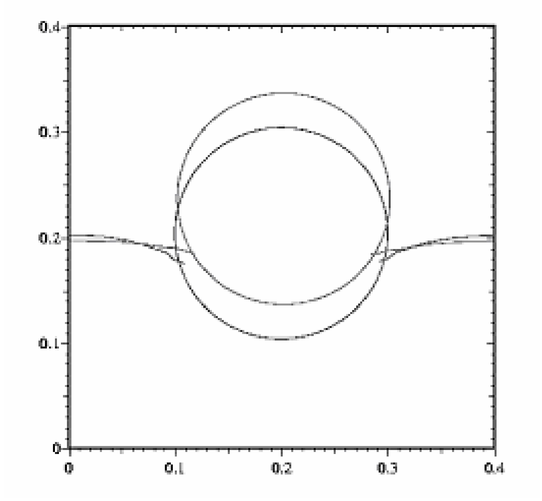

***Figure** VI.3. The sphere position and the corresponding interface shape are shown on the domain midsection. For the bottom sphere (shown as a circle) and the interface shape the surface tension is 10 dynes/cm and for the top sphere and the interface shape it is 25 dynes/cm. The depth to which a sphere sinks into the lower fluid decreases with increasing value of the surface tension.*

To validate our code further, we performed calculations for five different values of interfacial tension γ while keeping the other parameters fixed. Figure VI.3 shows that, as expected, when γ is smaller the particle sinks to a greater depth. In table VI.1 we have listed the floating heights, defined to be the vertical distance of the particle center from the contact line, and the sum of the pressure and vertical component of capillary forces acting on the particle for these five values of the interfacial tension. For all cases in equilibrium, as required, $F_p + F_c$ is approximately equal to the particle's weight. There are small differences due to numerical errors.

***Table VI.2.** The interfacial deformation h_2/R, the floating height $R \cos\theta_c$ and the point of contact θ_c are listed as a function of the upper fluid density. The interfacial tension is 16 dynes/cm. The sphere density is 1.05 g/cm^3 and its weight is 4.315 g cm/s^2. The density of lower fluid is 1.0 g/cm^3 and that of the upper fluid is varied. The floating height increases and the interface deformation decreases with decreasing density of the upper fluid.*

ρ_U (g/cm^3)	h_2/R	$R \cos\theta_c$	θ_c (degrees)
0.1	0.156	0.419	65.26
0.01	0.159	0.417	65.34
0.0016	0.161	0.417	65.37

In table VI.2 we have listed the floating heights for two additional cases where the density of the upper fluids are 0.01 gm/cm^3 and 0.0016 gm/cm^3, and the corresponding viscosities are 0.033 Poise and

0.0166 Poise. The interfacial tension is 16.0 dynes/cm. The time step used for these calculations was $2x10^{-5}$s. It is necessary to use a smaller value of the time step for these simulations because the ratio of lower and upper fluids densities is larger. The time step used is smaller also when the ratio of the lower and upper fluids viscosities is larger. The domain was discretized using mesh B described above. Table VI.2 shows that the floating height slightly decreases when the density of the upper fluid is reduced.

The equilibrium analysis, presented in section II, assumes that the fluid extends to infinity in the x-, y- and z-directions which is not the case for our simulations. This may explain some differences between our simulations and the analytical results. These differences are expected to decrease with increasing box size. We also wish to note that for our simulations the magnitude of fluid velocity decreases as the state of equilibrium is approached, but it does not decrease beyond a certain value which depends on the fluid viscosity, surface tension and the interface curvature. The flow develops steady spurious circulation cells around the interface that are similar to those seen in simulations of drops (Scardovelli and Zaleski (1999)). It has been noted by D.D. Joseph that these circulation cells arise in simulations because the discretized equation for the vorticity, which can be obtained by taking the curl of the momentum equation, contains a non zero contribution from the layer (V.4) representing the delta function in the level set method. This creates vorticity along the discretized interface which diffuses into the domain. The presence of these cells, however, does not seem to affect the overall force balance, discussed in table VI.1, for equilibrium.

VI.1.2. Motion of two spheres

We next present results for the case where two spherical particles are released near each other on the interface at the same vertical height. The initial interface position is assumed to be flat, except near the particle surfaces where a contact angle of 135° is prescribed. The initial vertical height of the spheres is higher than for a single sphere in equilibrium for the same parameter values. The parameters are assumed to be in the range for which a single sphere can be in equilibrium.

For these calculations, the particle density is 1.05 gm/cm^3. The interfacial tension is 16.0 dynes/cm. The upper fluid density is 0.01 gm/cm^3 and viscosity is 0.033 Poise. The initial velocities are assumed to be zero. The domain height is 0.4 cm. The domain width in the x-direction is 0.4 cm and in the y-direction is 0.8 cm. The undeformed interface passes though the domain center and the particle centers are initially at a height of 0.02 cm above the interface. The initial distance between the spheres in the y-direction is 2.6 R or 3.2 R. The mesh resolution is comparable to that for the coarse mesh in section VI.1.1.

We have already noted that when two or more spheres released in the interface are close they move towards each other due to the action of the lateral component of the capillary force associated with the asymmetric deformation of the interface around the particles. Figure VI.4a shows that for t=0.0042 the interface shape is deformed in a small region around the spheres and farther away it is relatively flat; hence there is no lowering of interface. Consequently, at this time, the spheres do not experience any lateral attractive force. But, as for a single sphere, the interface height around the spheres decreases as time increases and, as a result, the contact lines on both spheres move downward. The vertical component of capillary force, which is initially larger than the final value, causes the spheres to move upward, but as the contact lines move downward the vertical capillary force decreases and the vertical velocities become negative. After this initial motion for t<~0.05 s, the vertical velocities become relatively small, but remain negative as the spheres approach each other. These initial transients in the velocities of the spheres could be diminished by setting their initial positions and interface shape closer to those for the equilibrium of an isolated sphere. This would however complicate the problem of prescribing initial conditions and make the problem less realistic.

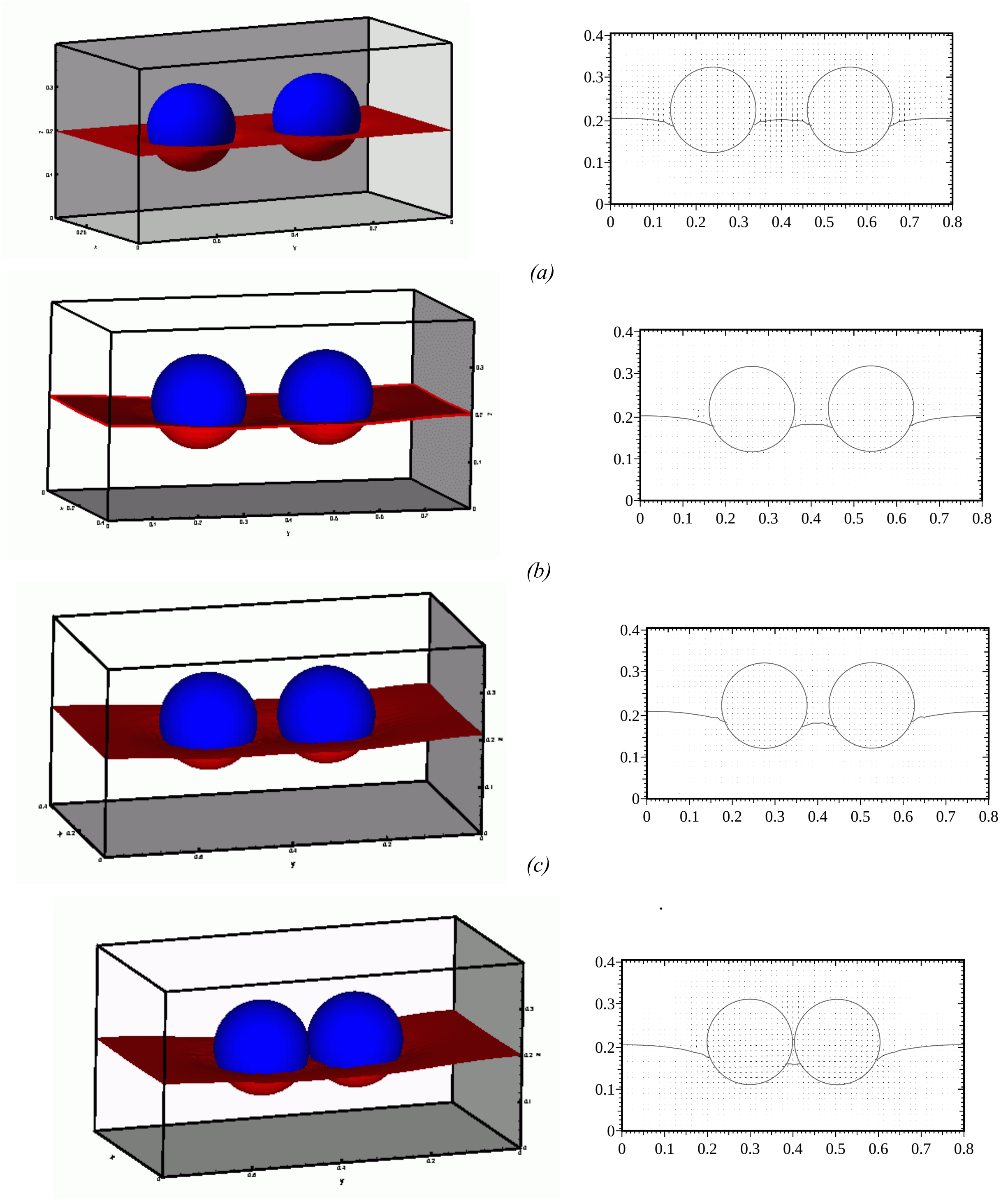

(a)

(b)

(c)

(d)

Figure *VI.4. The positions of two spheres suspended in the two-fluid interface and the velocity distribution at the domain midsection are shown at t=0.0042, 0.175, 0.225 and 0.339. The length of velocity vectors is magnified 50 times. The length of the velocity vectors is the largest in (a) and the smallest in (d) which indicates that the maximum velocity in the domain is decreasing with time. The particles are moving toward each other in the* *interface. The particles are "supported" by the capillary force associated with the deformation of the interface. The surface tension is 16.0 dynes/cm, the particle density is 1.05 g/cm^3 and the density of the top fluid is 0.01 g/cm^3 and that on the bottom is 1.0 g/cm^3. The initial distance between the spheres is 3.2 R. (a) Oblique views, (b) Side view of the velocity field on the domain midsection. The dimensionless parameters based on the maximum particle velocity are (Re=0.028, G=1.0x10^4, Ca=0.00875) and based on the capillary velocity are (Re=3.2, G=0.766).*

Snapshots at t=0.0042, 0.175, 0.225 and 0.399 of the evolution to equilibrium are shown in figure VI.4. At t=0.399 the spheres are close to equilibrium.

The magnitude of the lateral capillary force $F/(\gamma D)$ increases as the distance between the spheres decreases, where F is the y-component of capillary force acting on a sphere (see figure VI.5). This is also seen as an increase in the approach velocity v_2-v_1 plotted as a function of time in figure VI.5. However, the approach velocity begins to decrease due to the lubrication forces when the gap between the spheres is small enough. Simulations also show that when the distance between the spheres is larger, the initial approach velocity is smaller, because the lateral component of capillary force is smaller, and the time needed for the spheres to come together is larger. This is in agreement with (II.17) which implies that the lateral force increases with decreasing distance between the spheres. The dimensionless parameters based on the maximum lateral velocity are (Re=0.028, G=1.0x10^4, Ca=0.00875).

The contact line and the interface shape evolve as the spheres move toward each other. Therefore, the lateral component of the capillary force and the contribution of the pressure to force change as the distance between the spheres decreases. Petkov, et al. 1995 measured the approach velocity of particles and found that when the gap between the particles is smaller than O(30R), which is the case for our simulations, the non linearity of the interface curvature also influences the approach velocity. For the case described in figure VI.4 the simulations were stopped at t=0.339 when the distance between the spheres' surfaces reduced to 0.047 R. The interface shape at this time is shown in figure VI.4d. Notice that the interface height between the spheres in this figure is even lower and the interface shape is flatter. For the case where the initial distance between the spheres' surfaces is 0.6 R the time taken to reach the same separation is ~0.181. The approach velocity remains relatively small for t<~0.04 during which the initial interfacial deformation takes place, which is approximately the time interval in which a single sphere reached equilibrium in section VI.1.1.

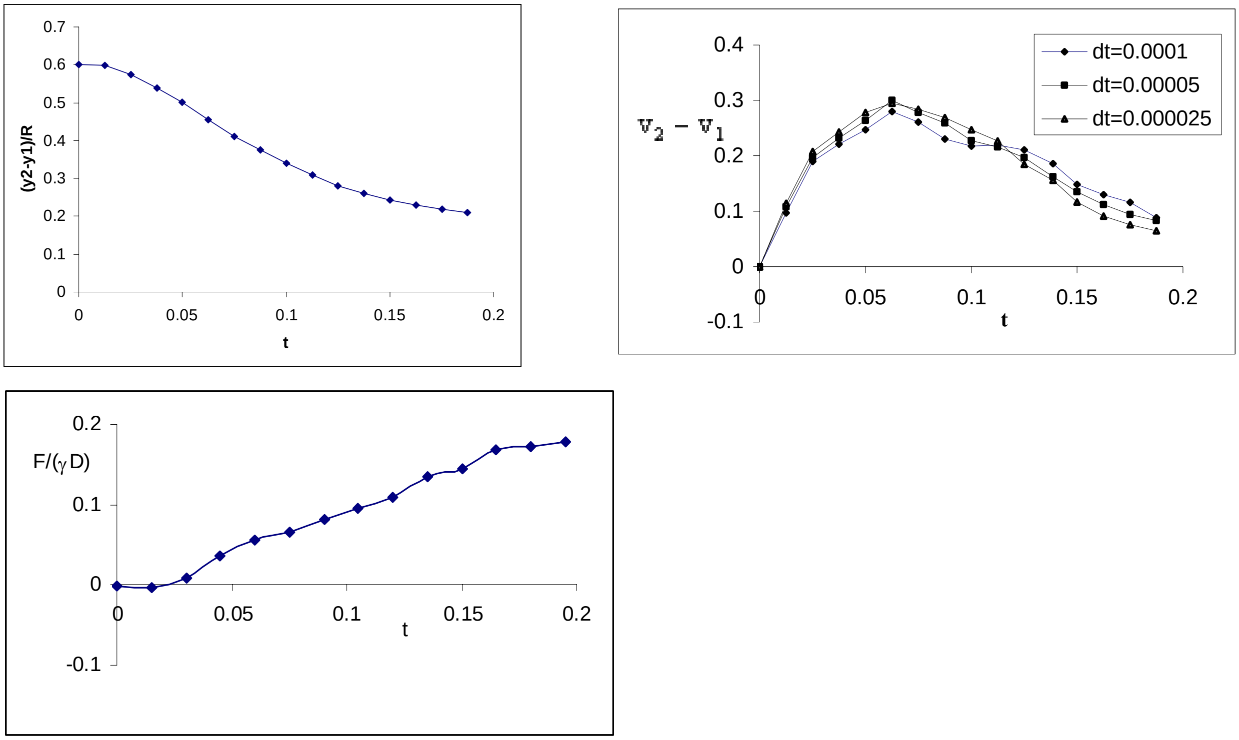

Figure VI.5. *The distance between the surfaces of spheres, the approach velocity v_2-v_1 and the lateral capillary force are plotted as functions of time. The approach velocity v_2-v_1 is shown for three different values of the time step. Notice that the approach velocity initially increases as the interface height between the spheres decreases and then decreases as the gap between the spheres becomes small. The initial distance between the spheres is 2.6R.*

In figure VI.6 the approach velocity and the dimensionless distance between the spheres are shown for five additional parameter values. For these cases, the spheres centers are initially at a height of 0.04 cm above the interface and the initial distance between the spheres in the y-direction is 3.2 R. These figures show that the approach velocity becomes positive after a short time interval and increases as the spheres move toward each other. The approach velocity decreases when the gap between the spheres becomes small due to the lubrication forces. The lateral velocity for small times is negative because when the spheres sink into the lower liquid the hydrodynamic force is repulsive. From these figures we also conclude that the approach velocity increases when the viscosity of the upper or lower liquid is decreased. It also increases when the particle density or the surface tension coefficient is increased. The lateral velocity contains oscillations when the Reynolds number is of order one or larger.

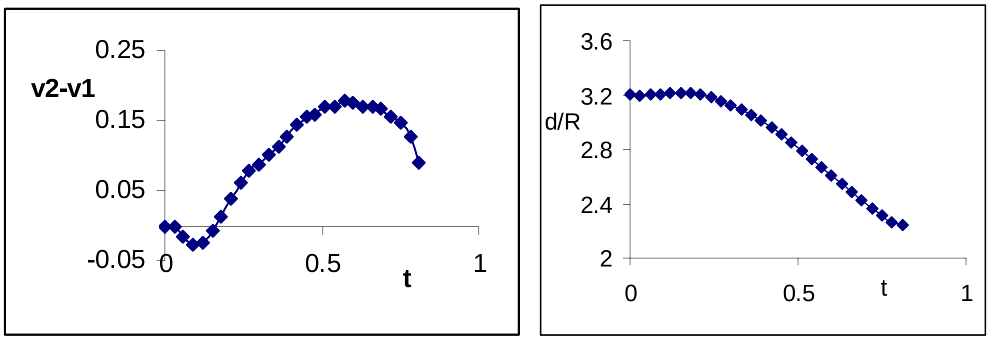

v2-v1
0.25
0.15
0.05
-0.05
0
0.5
1
t
d/R
3.6
3.2
2.8
2.4
2
0
0.5
t
1

(a)

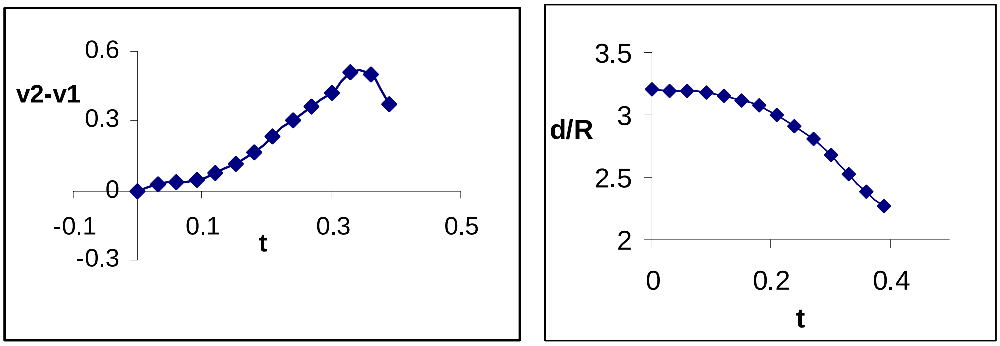

v2-v1
0.6
0.3
0
-0.1
0.1
0.3
0.5
-0.3
t
d/R
3.5
3
2.5
2
0
0.2
0.4
t

(b)

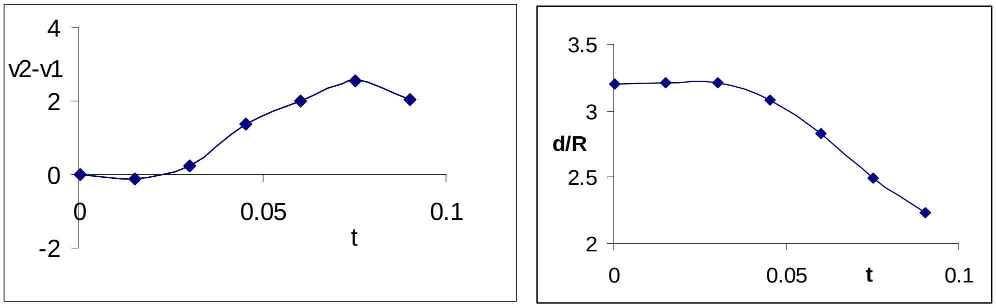

4
v2-v1
2
0
-2
0
0.05
0.1
t
3.5
3
d/R
2.5
2
0
0.05
t
0.1

(c)

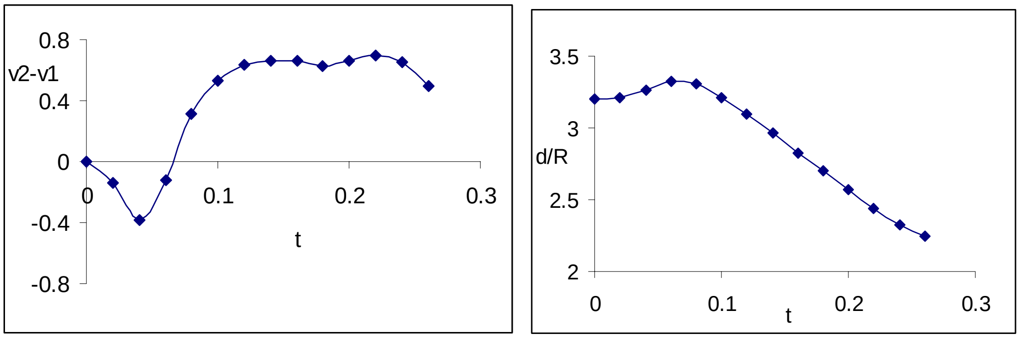

0.8
v2-v1
0.4
0
-0.4
-0.8
0
0.1
0.2
0.3
t
3.5
3
d/R
2.5
2
0
0.1
t
0.2
0.3

(d)

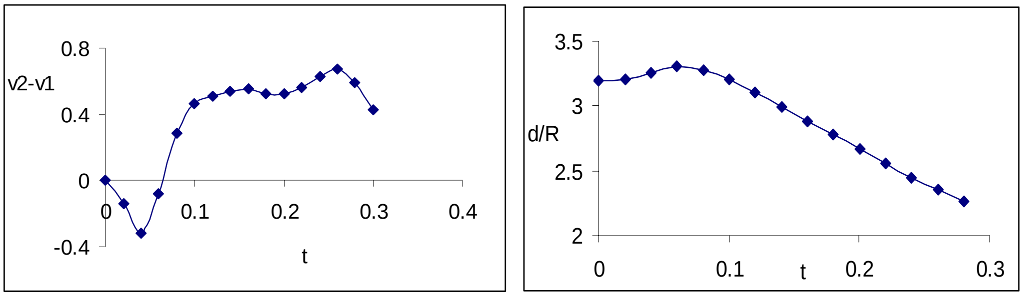

(e)

Figure VI.6. ***.*** *The distance between the spheres and the approach velocity* v_2-v_1 *are plotted as functions of time. Notice that the approach velocity initially increases as the interface height between the spheres decreases and then decreases as the gap between the spheres becomes small. The initial distance between the spheres is 3.2R. (a) The parameters are:* (l_p=1.1, l_U=1.0, m=1.0), η_L *=0.1 Poise and* γ*=2.0 dynes/cm. The dimensionless parameters based on the maximum particle velocity are (Re=0.38, G=*$5.4\text{x}10^3$*, Ca=0.0095) and based on the capillary velocity are (Re=40.0, G=0.491). (b) The parameters are:* (l_p=1.1, l_U=1.0, m=1.0), η_L *=0.01 Poise and* γ*=2.0 dynes/cm. The dimensionless parameters based on the maximum particle velocity are (Re=10.2, G=784.8, Ca=0.0025) and based on the capillary velocity are (Re=4000, G=*$4.9\text{x}10^{-3}$*). (c) The parameters are:* (l_p=1.01, l_U=10.0, m=10.0), η_L *=0.1 Poise and* γ*=16.0 dynes/cm. The dimensionless parameters based on the maximum particle velocity are (Re=5.12, G=29.9, Ca=0.016) and based on the capillary velocity are (Re=320, G=*$7.66\text{x}10^{-3}$*). (d) The parameters are:* (l_p=1.005, l_U=2.0, m=2.0), η_L *=0.1 Poise and* γ*=4.0 dynes/cm. The dimensionless parameters based on the maximum particle velocity are (Re=1.38, G=412.1, Ca=0.017) and based on the capillary velocity are (Re=80, G=0.12). (e) The parameters are:* (l_p=1.005, l_U=2.0, m=1.0), η_L *=0.1 Poise and* γ*=4.0 dynes/cm. The dimensionless parameters based on the maximum particle velocity are (Re=1.26, G=496.3, Ca=0.016) and based on the capillary velocity are (Re=80, G=0.12).*

Another interesting consequence of the lowering of interface height and contact lines between the spheres is a decrease in the vertical component of capillary force. This component of the capillary force acts against gravity and keeps them floating even though they are heavier than both liquids. This decrease causes the floating height of the spheres to decrease slightly (see table VI.3). For example, the height for a single sphere in section VI.1.1 for the same parameters was 0.419, but for the two spheres in figure VI.4d it is 0.375, where they are almost touching. This decrease in the floating height raises the contact line position everywhere except between the spheres so that the vertical component of the capillary force returns to the value required for balancing their buoyant weights (see figure VI.7). When the parameters are such that the sum of the vertical component of the capillary and pressure forces is near its maximum value for an isolated sphere, a decrease in the floating height would actually decrease the vertical component of total force. Therefore, if the spheres are barely floating, a decrease in the floating height will cause them to sink. This suggests that the clusters of spheres are more likely to sink than an isolated sphere.

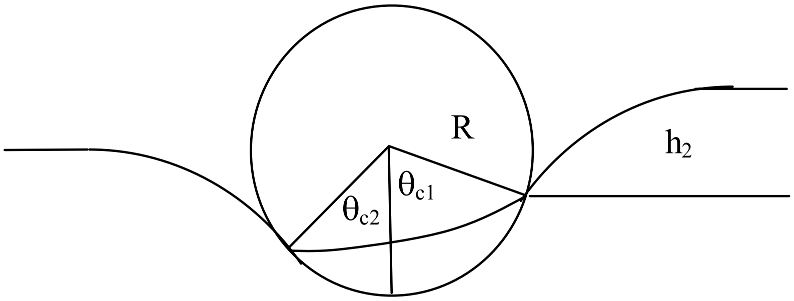

Figure VI.7. *The figure shows the contact line and the interface shape near a floating sphere. The contact line position on the left is lower, i.e., $\theta_{c2}<\theta_{c1}$, as there is another sphere floating to the left (not shown). Figure II.8 shows that the vertical capillary force increases with increasing θ_c only when θ_c is less than 109°* *(which depends on the contact angle). Thus, the vertical capillary force acting on the right side of the sphere is larger than on the left side. But, if θ_{c1} is greater than 109°, this may not be the case.*

Table VI.3. *The floating height R cos θ_c, the point of contact θ_c and the interfacial deformation h_2/R are shown as a function of the distance d between the spheres. The interfacial tension is 16.0 dynes/cm. The sphere density is 1.05 gm/cm^3. The density of the lower fluid is 1.0 gm/cm^3 and that of the upper fluid is 0.1 gm/cm^3. The floating height is computed based on the contact line position on the sphere surface away from the gap. Notice that the floating height of the spheres decreases and the interfacial deformation increases as they come closer. These values should approach the values for an isolated particle when the distance d is large.*

d (cm)	R cos θ_c (cm)	θ_c (degrees)	h_2/R
0.279	0.397	66.60	0.234
0.2493	0.388	67.13	0.289
0.2118	0.375	67.99	0.302

VI.1.3. Motion of four spheres

For these calculations the sphere density is 1.05 gm/cm^3 and the interfacial tension is 16.0 dynes/cm. The upper fluid density is 0.1 gm/cm^3 and the viscosity is 0.1 Poise. The motion starts from rest. The domain height is 0.4 cm. The width along x-direction is 0.8 cm and along y-direction is 0.8 cm. The undeformed interface passes though the domain center. The initial positions of the four spheres are (0.4,0.22,0.22), (0.4,0.58,0.22), (0.23,0.4,0.22) and (0.57,0.4,0.22). The mesh resolution is the same as for the coarse mesh in section VI.1.1.

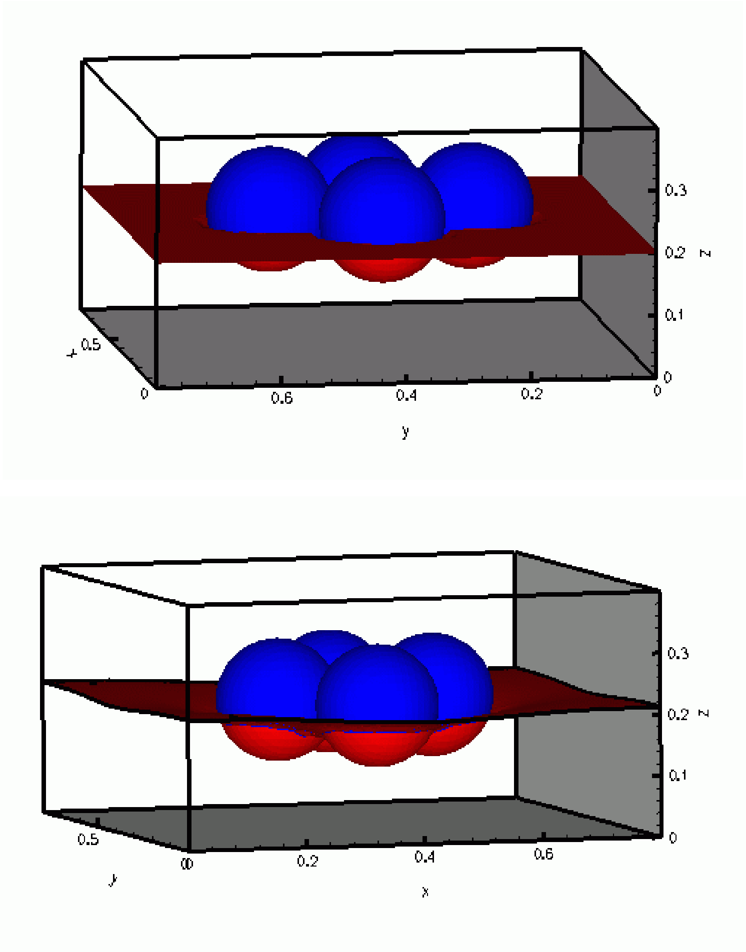

Figure VI.8. Oblique views showing the positions of four rigid spheres suspended in the two-fluid interface at t=0.002 and 0.096. After they are released, they move toward each other. The surface tension is 16.0 dynes/cm, the particle density is 1.05 g/cm^3 and the density of the top fluid is 0.1 g/cm^3 and that on the bottom is 1.0 g/cm^3. The dimensionless parameters based on the maximum particle velocity are (Re=0.032, G=7664.1, Ca=0.01) and based on the capillary velocity are (Re=3.2, G=0.766).

After initial transients have died out, the spheres move toward each other. Their vertical velocity becomes small at t=~0.05 and around this time the interface height between the spheres begins to decrease.

In figures VI.8a and b the spheres and interface shape are shown at t=0.002 and 0.096, respectively. In the first figure, the interface shape between spheres is not significantly deformed and the lateral velocities are small and in the second figure the interface between the spheres is lowered. The interface shape and the contact lines for the spheres are no longer symmetric and thus the lateral component of capillary force acting on the spheres is not zero which causes them to move laterally towards each other.

As spheres approach each other, the vertical component of capillary force decreases due to the lowering of interface height between the spheres and thus the floating heights of the spheres decrease slightly (see figure VI.8b). For example, the height for a single sphere in section 3.1 for the same parameters is 0.419, for the two sphere case it is 0.375, and for the four spheres in figure VI.8b, where they are almost touching, it is 0.355.

VI.2 Initial value problems for floating disks

The disks in our simulations are released with the top plane of the disk in the plane of the undeformed interface. The disk velocity, its position and the interfacial deformation change with time. The final state, described by expression (II.8), is independent of these transients and can be used to verify the accuracy of numerical results. In equilibrium, the interface shape is such that the capillary force is exactly balanced by a jump in the pressure across the interface and therefore no fluid flow is induced. The fluid velocity in simulations is small but nonzero.

VI.2.1. Motion of a single disk

We first discuss results that show that the trajectory of a disk released in the two-fluid interface is independent of the mesh resolution and the time step. We have used two regular tetrahedral meshes to show that the results converge with mesh refinement. The rigid body constraint inside particles is enforced using uniformly distributed collocation points. The number of velocity nodes and elements in the first mesh are 117,649 and 13,824, respectively. In the second mesh, referred to as mesh B, there are 274,625 velocity nodes and 32,768 elements. The time step for these simulations is 0.0001 s or 0.00005 s.

The disk radius is 0.1 cm and its density is 1.5 gm/cm^3. The interfacial tension is 5.0 dynes/cm. The density of the upper fluid is 0.1 gm/cm^3 and its viscosity is 0.1 Poise. Initially, all velocities are zero. The domain is cubical with sides 0.4 cm. The top surface of the disk is in the plane of the undeformed interface which is at z=0.28 cm. The parameters are in the range for which a disk trapped in the interface can be in equilibrium.

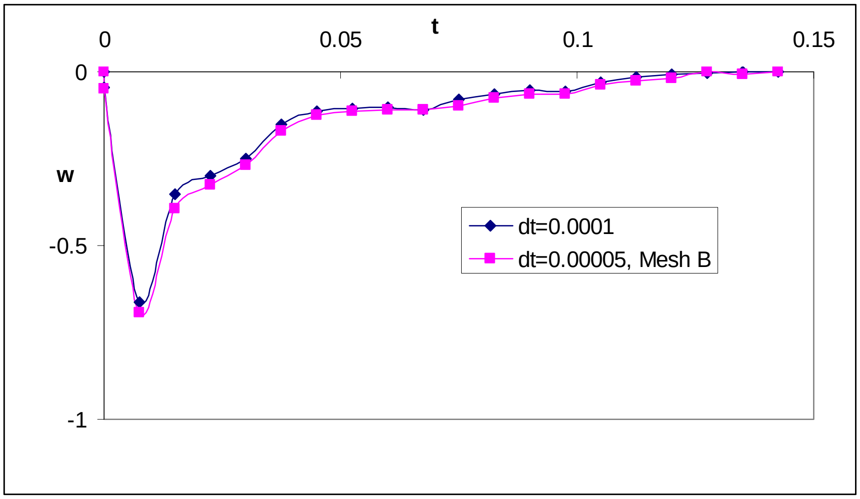

Figure VI.9. *The vertical component of velocity w for a disk released in the interface is shown as a function of time for two different values of the time step. The curve marked mesh B is for a more refined mesh. The density and viscosity of the lower fluid are 1.0 gm/cm^3 and 1.0 Poise and those of the upper fluid are 0.1 gm/cm^3 and 0.1 Poise. The interfacial tension is 5.0 dynes/cm and the particle density is 1.5 gm/cm^3. The dimensionless parameters based on the maximum vertical velocity of the disk are (Re=0.35, G=100.2, Ca=0.014) and based on the capillary velocity are (Re=50, G=0.039).*

Figure VI.9 shows that the numerical results for w vs. t converge with both mesh and time step refinements. Figures VI.9 also shows that the vertical component w of the velocity of the disk decreases for t<~0.02 s. It begins to increase slowly at t=~0.02 s and fluctuates around zero for t>~0.12 s (see figure VI.10). The other components of velocity u and v are negligible for all times. We will assume that for t=0.12 s the particle has reached a state of equilibrium with h_2=0.28R and ψ=45.8º. Table VI.4 shows that these values are in good agreement with the equilibrium requirement (II.8). We may therefore conclude that the state of equilibrium is captured correctly by our code.

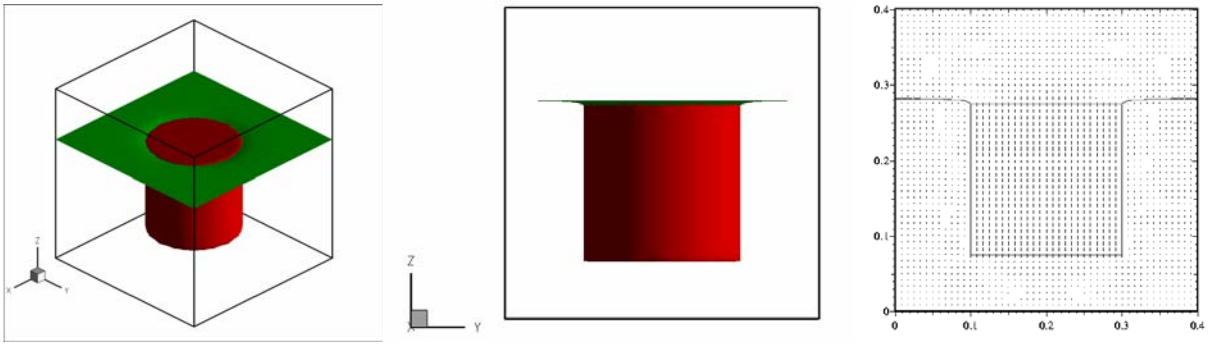

VI.10a

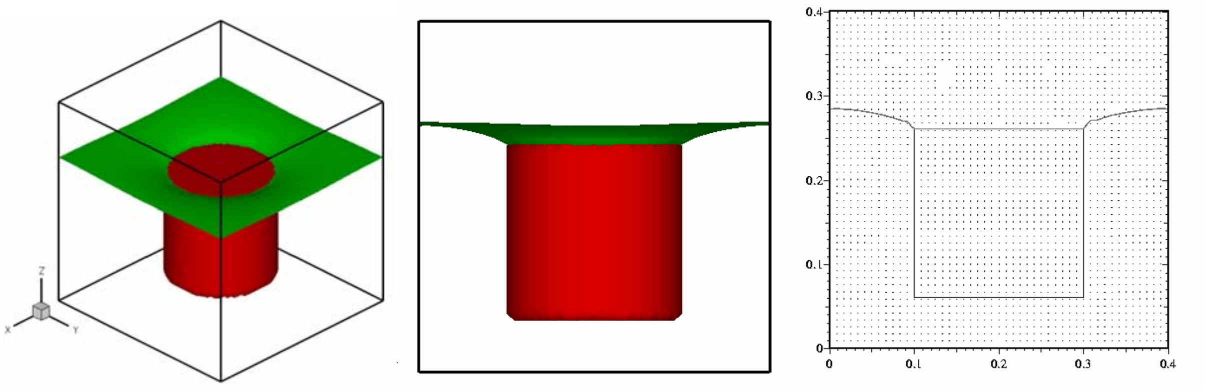

VI.10b

***Figure** VI.10. The disk position, the interface shape and the velocity field in the domain midsection are shown. The length of velocity vectors is magnified 30 times. The oblique and side views are shown. (a) t=0.0125 s, (b) t=0.15 s. The dimensionless parameters based on the maximum vertical velocity of the disk are (Re=0.35, G=100.2, Ca=0.014) and based on the capillary velocity are (Re=50, G=0.039).*

The vertical velocity w decreases initially with time because the disk is denser than the liquid below and the vertical component of the capillary force is zero, as the interface is not deformed. The buoyant weight and the contact angle increase simultaneously as the disk sinks.

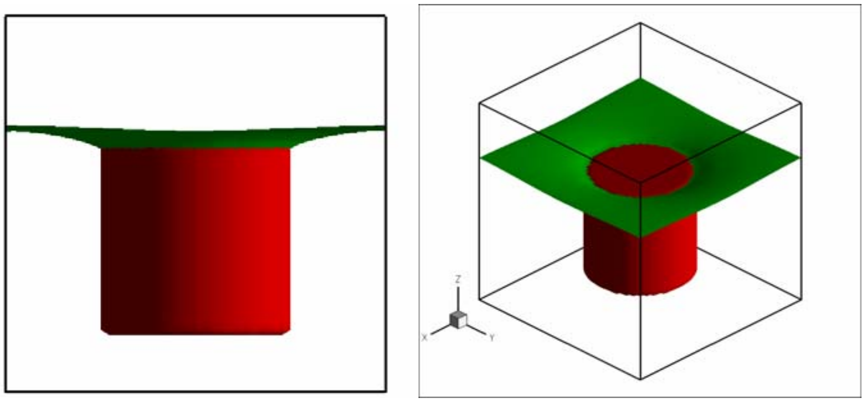

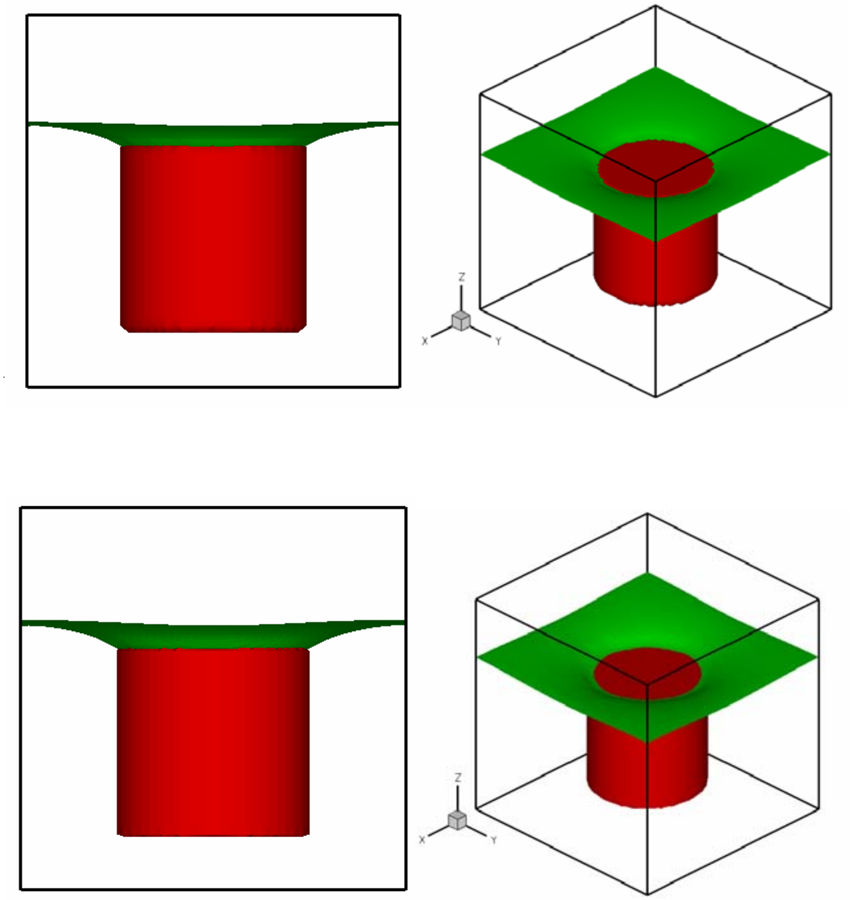

***Figure** VI.11. The oblique and front views of the floating disks and the interface shape are shown. The depth to which a disk sinks into the lower fluid increases with increasing disk density. (a) ρ_p=1.1, (b) ρ_p=1, and (c) ρ_p=1.5.*

We performed calculations for two additional values of the disk density ρ_p while keeping the other parameters fixed. Figure VI.11 shows that heavier disks sink to a greater depth and the contact angle is larger. In table VI.4 we give the computed values of h_2/R and the forces $F_p + F_c$ for the three values of ρ_p. For all cases, the computed values of the force are approximately equal to the weight of the disk. Some small differences are due to numerical errors. The equilibrium analysis of section II assumes that the fluid extends to infinity in the x-, y- and z-directions which is not the case for our simulations. This may explain small differences between our simulations and the analytical results.

***Table VI.4.** The interfacial deformation h_2/R and the sum of the pressure and vertical component of capillary forces obtained using (II.6) and (II.7) are shown as a function of the disk density. The interfacial tension is 5.0 dynes/cm. The density of lower fluid is 1.0 gm/cm^3 and that of the upper fluid is 0.1 gm/cm^3. For all three cases,* $F_p + F_c$ *is* *approximately equal to the disk weight. Also notice that, as expected, the interface deformation increases with increasing particle density.*

ρ (gm/cm^3)	weight (g cm/s^2)	h_2/R	$F_p + F_c$ (g cm/s^2)
1.1	6.78	0.15	6.86
1.2	7.40	0.21	7.38
1.5	9.24	0.28	9.26

VI.2.2 Motion of two disks

We next present results for the case where two disks are released near each other in the interface at the same vertical height. The domain height is 0.4 cm. The domain width along the x-direction is 0.8 cm and along the y-direction is 0.4 cm. The disk diameter is 0.1 cm and the height is 0.1 cm. The undeformed interface is at a distance of 0.23 cm from the bottom. The initial velocities are assumed to be zero. The mesh resolution is comparable to that for the coarse mesh in subsection VI.2.1.

We first describe the case for which the particle density is 1.1 gm/cm^3, the interfacial tension is 3.0 dynes/cm, and the upper fluid density and viscosity are 0.1 gm/cm^3 and 1.0 Poise, respectively. The viscosity of the lower fluid is 10.0 Poise. The two disks are placed at (0.32, 0.2, 0.18) and (0.48, 0.2, 0.18). The initial distance between the disks in the x-direction is 3.2R. Figure VI.12a shows that at t=0.04 the interface is deformed only in a small region around the disks and the disks do not experience a lateral attractive force. When the disks sink the contact angles increase. After this initial motion for t<~0.12 s, the disks sink slowly, as they move toward each other.

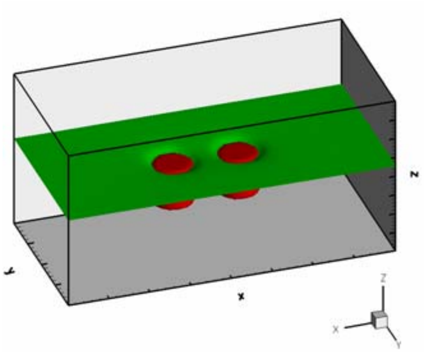
y
x
Z
X
Y

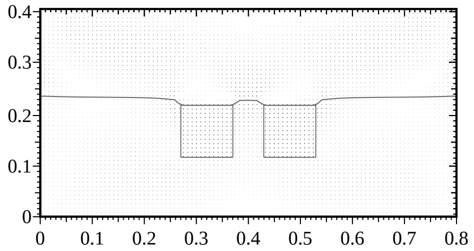
0.4
0.3
0.2
0.1
0
z
0
0.1
0.2
0.3
0.4
0.5
0.6
0.7
0.8

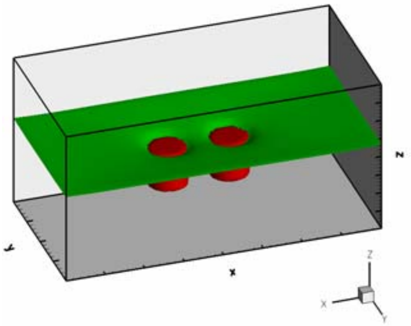
y
x
Z
X
Y

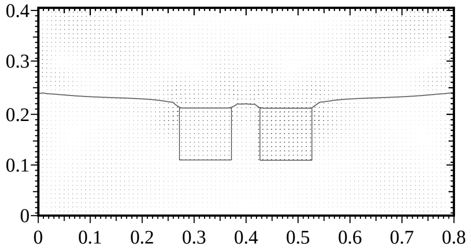
0.4
0.3
0.2
0.1
0
z
0
0.1
0.2
0.3
0.4
0.5
0.6
0.7
0.8

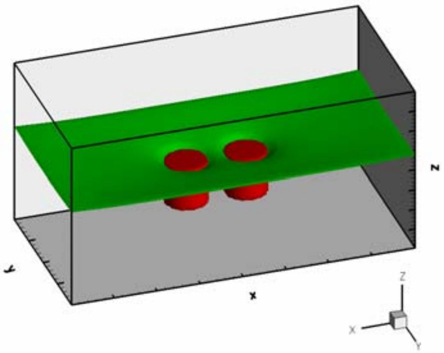
y
x
Z
X
Y

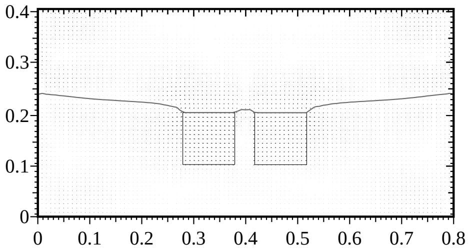
0.4
0.3
0.2
0.1
0
z
0
0.1
0.2
0.3
0.4
0.5
0.6
0.7
0.8

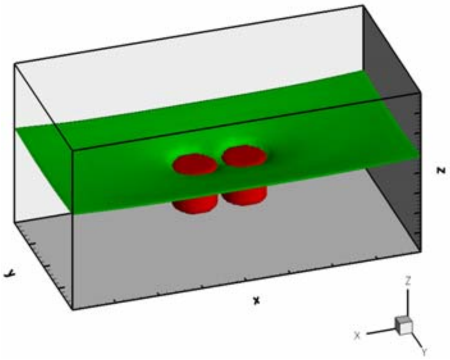
y
x
Z
X
Y

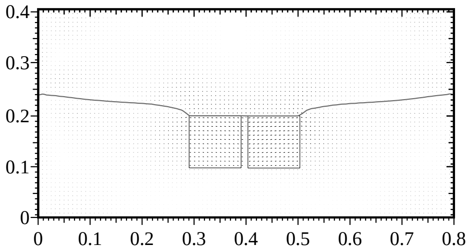
0.4
0.3
0.2
0.1
0
z
0
0.1
0.2
0.3
0.4
0.5
0.6
0.7
0.8

***Figure** VI.12. The positions of two disks suspended on the two-fluid interface and the velocity distribution at the domain midsection are shown at t=0.04, 0.2, 0.5 and 0.8 s. The length of velocity vectors is magnified 50 times. The disks move toward each other in the interface. The surface tension is 3.0 dynes/cm, the particle density is 1.1 g/cm^3 and the density of the top fluid is 0.1 g/cm^3 and that of the bottom fluid is 1.0 g/cm^3. The initial distance between the disks is 3.2 R. The dimensionless parameters based on the maximum velocity of the disk are (Re=0.0023, G=242.0, Ca=1.5) and based on the capillary velocity are (Re=1.5x10^{-3}, G=545.0).*

In figure VI.12b the disks and the interface shape are shown at t=0.2 s. The interface height between the disks in figure VI.12c at t=0.5 s is significantly lower than on the sides. Since the contact angle between the disks is smaller, the lateral capillary force is larger.

Figure VI.13a shows that the approach velocity u_2-u_1 first increases and then decreases with time. The approach velocity increases with time because the lateral component of the capillary force increases as the distance between the disks decreases. This also causes the disks to slightly tilt in the xz-plane. For all cases simulated in this paper it is smaller than 0.5^o. The time taken by the disks to come together increases with the initial distance not only because the distance is larger, but also because the approach velocity decreases with increasing distance. Figure VI.13a also shows that the approach velocity starts to decrease when the gap between disks becomes small compared to the disk radius due to the activation of lubrication forces.

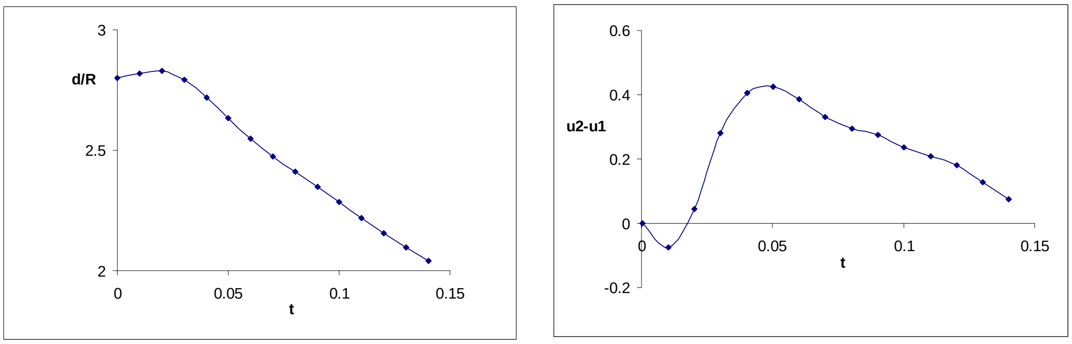

VI.13. (a)

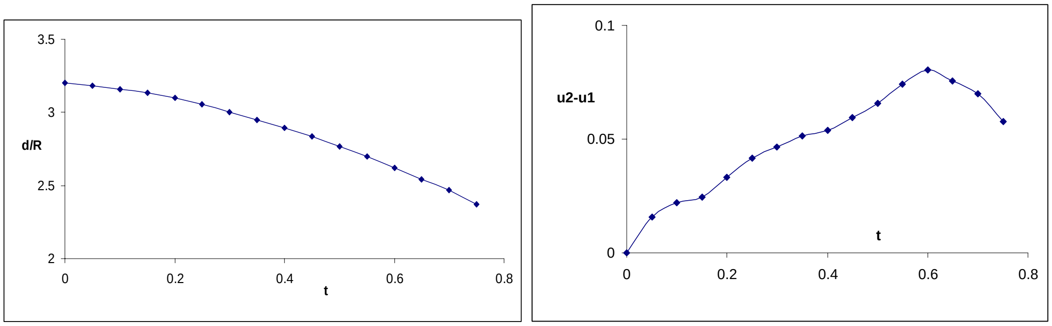

VI.13. (b)

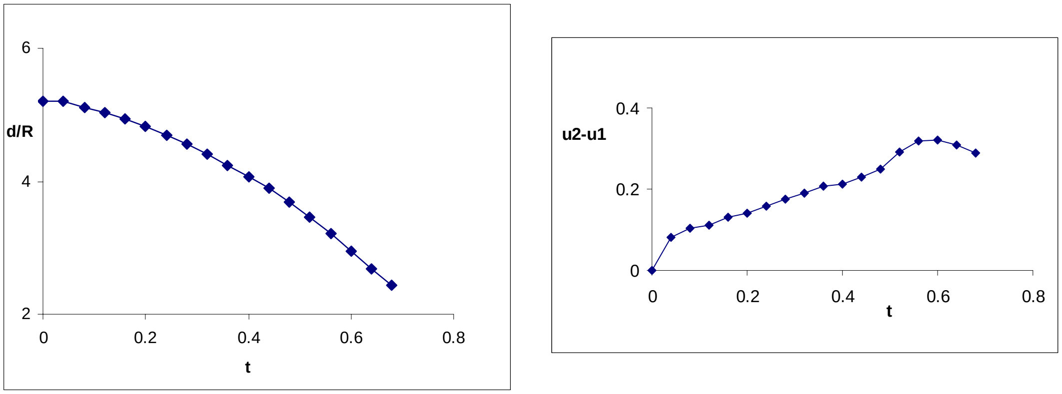

VI.13. (c)

Figure VI.13. *The approach velocity u_2-u_1 and the dimensionless distance d/R between the disks are plotted as functions of time. The approach velocity initially increases as the interface height between the disks decreases and then decreases as the gap between the particles becomes small. (a) The initial distance between the disks is 2.8R and the dimensionless parameters based on the maximum disk velocity are (Re=0.11, G=2224.5, Ca=0.0021), (b) The* *initial d/R=3.2 and the dimensionless parameters are (Re=0.0023, G=242.0, Ca=1.5) (c) The initial d/R= 5.2 and the dimensionless parameters are (Re=0.11, G=2224.5, Ca=0.0021).*

In figure VI.13 we have plotted the separation distance $d/R \geq 2$ and the approach velocity u_2-u_1 as function of time for three initial values of d/R = (2.8, 3.2, 5.2) at t=0. In all cases the approach velocity has a maximum value at a certain time and then decreases. The slow down is due to activation of lubrication force at close approach. The approach velocity in the case of the smallest initial distance d/R=2.8 shown in figure VI.13a is negative for a short period and the particles first disperse and then attract.

The same type of plots are presented for the case in which the viscosity of the lower fluid is reduced tenfold, from 0.1 to 0.01 Poise and d/R=6, larger even than d/R=5.2 in figure VI.13c. The magnitudes of the velocities which develop are larger in the small viscosity fluid even though the initial separation is larger. The approach velocity is not monotonic due to changes in the interface shape away from the disk.

The tendency toward initial repulsion followed by attraction seen in figure IV.1a when the initial separation d/R=6 is small has been observed in experiments. Joseph et al. 2003, say (page 143)

> "We create such dispersions by pouring particles on the liquid, nothing complicated, just like a salt shaker. As soon as the particles hit the liquid surface they disperse radially leading to dispersions like that 3 minutes in figure 4. The dispersion, followed by attraction, is more or less universal and we have not seen it mentioned in the literature."

We expect the limiting value d/R=2 to be achieved asymptotically as $t \to \infty$; this asymptotic result cannot be achieved with the present numerical package which uses a security zone to prevent collisions of particles. In the future we will implement the new scheme of Singh, Hesla and Joseph 2003 which does allow collision and close packing in equilibrium.

Since the computation domain size for our simulations is only 8 R, the interface evolution near the particles is also influenced by the conditions imposed at the domain boundary. On the domain walls, the contact line does not remain flat; its level is lower in the middle of the domain walls and higher in the domain corners. This causes the particles approach velocity to vary, as the lowering on contact lines on the domain walls influences the magnitude of the lateral attractive force, especially when the gap between the disk and a domain wall is comparable to the distance between the disks. This effect, which is due to a finite size of the computational domain, can be diminished by performing simulations in larger domains.

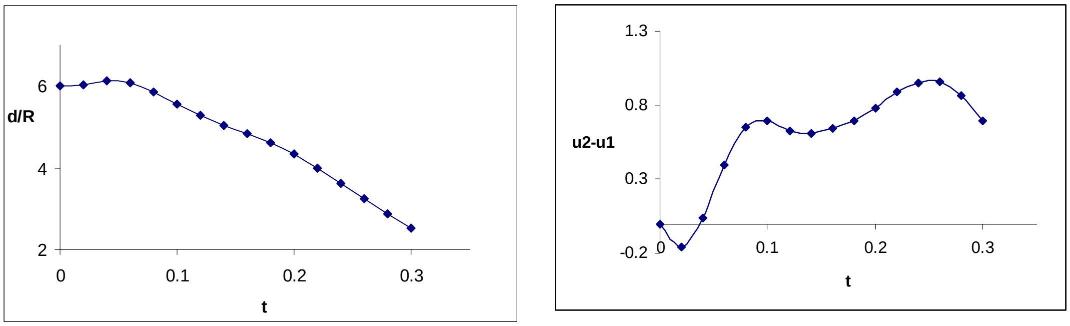

Figure VI.14. *The approach velocity u_2-u_1 and the dimensionless distance d/R between the disks are plotted as functions of time. The approach velocity initially increases as the interface height between the disks decreases and then decreases as the gap between the particles becomes small. The lower fluid viscosity is 0.01 Poise and the initial d/R= 6. The dimensionless parameters based on the maximum disk velocity are (Re=2.4, G=425.8 Ca=0.0024).*

An interesting consequence of the lowering of the interface height between the disks is that the average value of the contact angle around the disk decreases. This decrease reduces the vertical component of capillary force which acts against gravity and keeps the disks floating. A reduction in the vertical capillary force causes the disks to sink slightly increasing the contact angle everywhere except between the disks. After this additional sinking, the buoyant weight again becomes equal to the vertical component of the capillary force. This additional sinking, which also happens when two floating spheres come near each other, suggests that the clusters of disks are more likely to sink than an isolated disk.

VI.2.2.1 Role of the particle density

In table VI.5 we have given results for the approach velocity for different values of the particle density. A denser disk sinks more causing a greater interfacial deformation. The lateral force which arises from the asymmetry is then greater and the velocity with which the disks approach each other is larger.

Table VI.5. *The maximum approach velocity for the disks is listed to show the dependence on their density. The lower fluid viscosity is 0.1 Poise and the density is 1.0 gm/cm^3. The initial distance between the disks is 2.8 R.*

ρ_p	ρ (upper fluid)	η (upper fluid)	γ	$(u_2\text{-}u_1)_{max}$
1.1	1	0.1	10	0.0036
1.5	1	0.1	10	0.0762
1.5	0.1	0.01	10	0.034
2.0	0.1	0.01	10	0.066

VI.2.2.2 Role of the fluid density ratio

In this subsection we show how u_2-u_1 depends on $l_U=\frac{\rho_U}{\rho_L}$. The case of matched densities $\rho_U=\rho_L$ is interesting because the lowering of the interface does not cause an increase in F_p. This case is also interesting because after the motion stops an equilibrium is reached in which the variation of pressure does not depend on the interface shape. This implies that the interface must deform so that there is no pressure jump across it; hence the mean curvature of the deformed interface is zero.

When the density ratio l_U is decreased the disks sink to a lower depth and their lateral approach velocities are smaller. The maximum approach velocities for two cases are listed in table VI.6.

Table VI.6. The maximum approach velocities for the disks are listed to show dependence on the upper fluid density. The lower fluid viscosity is 0.1Poise and the particle density is 1.5 gm/cm^3. The initial distance between the disks is 2.8 R.

ρ_{lower}	ρ (upper fluid)	η (upper fluid)	γ	$(u_2\text{-}u_1)_{max}$
1.0	1	0.1	10	0.0762
1.0	0.1	0.1	10	0.039

VI.2.2.3 Role of the viscosity ratio

We know from analysis of section II that the viscosity does not play a role in determining the equilibrium state of floating particles, but it does alter the velocity. The lateral velocity of the disk decreases with increasing viscosity, but is not so strongly dependent on the viscosity ratio $m=\frac{\eta_U}{\eta_L}$.

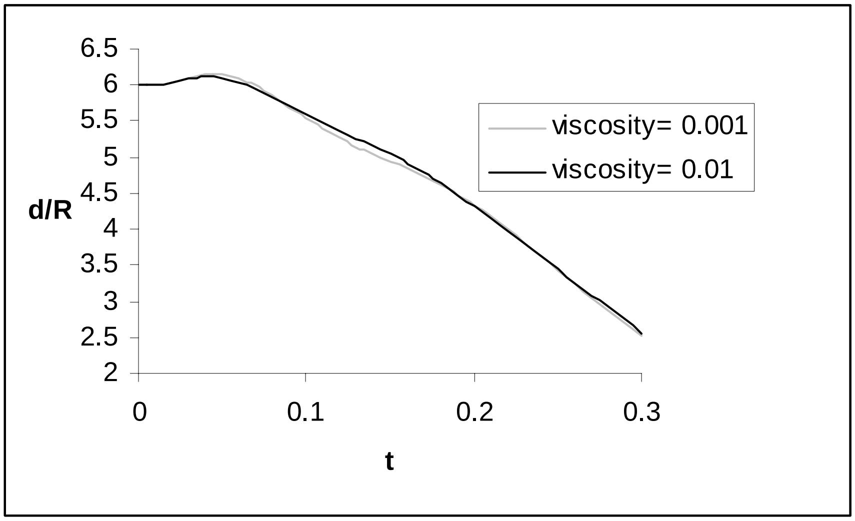

Figure VI.14. The dimensionless gap between the disks is plotted for two different values of the upper fluid viscosity. As the disks are almost completely immersed, the effect of the upper fluid viscosity on the lateral disk velocity is negligible.

In figure VI.14 we have shown results for two different values of $\frac{\eta_U}{\eta_L}$. All other parameters are kept fixed. The approach velocity increases, but only slightly as the viscosity ratio is decreased. These velocities at a fixed distance of 2.7 R for the disks released at the initial distance of 2.8 R. are listed in table VI.7. The velocity increase is due to a decrease in the viscous resistance of the upper fluid. The increase in the velocity is greater for the heavier particles and also for larger values of l_U; in these cases the interfacial deformation is greater.

Table VI.7. The maximum approach velocities for the disks are listed to show the dependence on the upper fluid viscosity. The lower fluid viscosity is 0.1 Poise and the particle density is 2.0 gm/cm^3. The initial distance between the disks is 2.8 R.

ρ_{lower}	ρ (upper fluid)	η (upper fluid)	γ	$(u_2-u_1)_{max}$
1.0	0.01	0.01	10	0.291
1.0	0.01	0.005	10	0.297

VII. Conclusions

This is the first paper on the direct numerical simulation of the motion of solid floating particles. A floating smooth particle, embedded in the interface between two fluids, touches the interface at a fixed contact angle, which at equilibrium is given by the Young-Dupré law. For a floating prismatic particle, on the other hand, the contact line is assumed to be fixed at its sharp edge, provided the contact angle at the edge is within the limits specified by the Gibbs extension to the Young-Dupré law. For example, in our simulations of disks, floating with their axis normal to the interface, the contact line is assumed to be pinned at the top sharp edge of the disk.

The constraint that the contact line remains pinned at a sharp edge of a prismatic particle is different from that for a smooth particle, such as a sphere. For a smooth particle, the contact line can move, but the contact angle is fixed and here is assumed to be that at equilibrium given by the Young-Dupré law. The problem of the motion of the contact line is difficult and unsolved. The problem is that the no slip condition implies that the contact point cannot move which contradicts the behavior seen in experiments (see Dussan and Davis 1974, Dussan 1976 and Kistler and Scriven 1993 and references therein). Several approaches to this problem have been proposed and could be implemented in direct numerical simulations (see Sussman 2001, Friedrichs and Guceri 1993, Kamal, Goyal and Chu 1988, and references therein). Here we look at one approach which could be called capillary induced motion of the contact line due to a prescribed contact angle. In this approach, we let the contact line adjust to the dynamics under the constraint that the contact angle is fixed. The no slip condition is satisfied before and after the contact line moves. In another approach, not implemented here, the contact line is allowed to slip by relaxing the no slip condition by putting the velocity of the contact line proportional to the shear stress there. This approach requires us to relax the prescribed contact angle condition. Another feature, not treated here, which impacts the floating particle problem is the existence of advancing and receding contact angle. The subject is very rich with many possibilities that might be studied in direct simulations.

The Marchuk-Yenenko operator-splitting technique is used to decouple the four primary numerical difficulties of the governing equations: incompressibility constraint, nonlinear convection term, Lagrange multiplier problem that forces rigid body motion within the particles, and the interface advection problem. The resulting four sub-problems are solved efficiently using matrix free approaches. Specifically, the DLM approach is used for enforcing rigid body motion inside the particles, the level set approach for tracking the interface and the conjugate gradient algorithms are used to enforce the incompressibility constraint and to solve the nonlinear convection problem. The contact line is kept at a sharp edge by making the level set function zero along the edge. On smooth surfaces the contact angle is kept fixed by using the technique described above. The code is validated by simulating the time dependent motion of a particle released on a two-fluid interface to steady state.

Our simulations show that the interface shape near a sphere adjusts quickly after it is released to meet the contact angle requirement, but away from the sphere the interface shape takes a much longer time interval to adjust during which the vertical position of particle changes. The computed results are shown to be independent of the mesh resolution as well as the size of time step. The steady state limits of our dynamic simulations agree with the equilibrium results. The time dependent simulations of two or more floating particles lead to capillary attraction and the formation of clusters. The attractive capillary force arises due to the asymmetric interface deformation around the particles. Specifically, the interface height between the particles is lowered giving rise to a lateral attractive force due to capillarity. This lowering of the interface also decreases the net vertical component of the capillary force which causes the floating height of the particles to decrease. These results agree qualitatively with the experimental data as well as the equilibrium analysis.

For floating disks, simulations are started by assuming that the interface is flat and that the top surface of the disk is in the plane of the interface ensuring that the contact line is initially pinned at the sharp rim. The disk assumed to be denser than the liquid sinks into the lower liquid. As it sinks, the contact angle increases which in turn increases the vertical component of the capillary force. The disk stops sinking when its buoyant weight is balanced by the capillary force. The code is validated by simulating the time dependent motion of a disk released on a two-fluid interface to steady state. Simulations show that as the disk sinks, the interface near the disk moves downward, as the contact line is pinned to the edge, but away from the disk the interface shape takes a longer time interval to adjust during which the vertical position of the disk changes. The computed results are independent of the mesh resolution as well as the size of the time step. The steady state limits of our dynamic simulations agree with the equilibrium results.

Simulations also show that the lowering of the interface between disks pinned to the interface at the rim reduces the contact angle between the disks giving rise to the unbalanced attractive capillary force. Two floating spheres also attract, but the mechanism by which the attractive force arises is different. Specifically, the lateral force on two floating spheres arises due to the lowering of the contact line on the surfaces between the two spheres which is a consequence of the constraint that the contact angle is fixed. For floating disks, on the other hand, the contact line is fixed and the lateral force arises due to a decrease in the contact angle between the disks due to the lowering of the interface. The lowering of the interface also decreases the net vertical component of the capillary force which causes the floating height of the particles to decrease.

Though our floating particle code has been optimized in various ways it still runs slowly. Improvements can be made by parallelizing the code for machines with large clusters. The security zone which has been used in previous direct numerical simulation based studies, and this one, does not allow contact between particles and hence is not faithful to the crystal structures which can evolve in problems of self assembly due to capillary attraction. Fortunately, the new collision scheme put forward by Singh, Hesla and Joseph 2003 does allow particle-particle contact and close packing. We will implement this new strategy in our future work.

Acknowledgements

This paper is dedicated to Professor Stan Osher on the occasion of his 60th birthday. This work was partially supported by National Science Foundation KDI Grand Challenge grant (NSF/CTS-98-73236) and a GOALI grant NSF/CTS-0109079, Engineering Research Program of the Office of Basic Energy Science at DOE, a grant from Schlumberger foundation, from STIM-LAB Inc., New Jersey Commission on Science and Technology through the New-Jersey Center for Micro-Flow Control under (Award Number 01-2042-007-25) and the University of Minnesota Supercomputing Institute.

Appendix. Weak form of equations and finite-element discretization

The approach used for obtaining the weak form of the governing equations was described in Glowinski, et al. 1999 and Singh, et al. 2000. In obtaining this weak form, the hydrodynamic forces and torques acting on the particles can be completely eliminated by combining the fluid and particle equations of motion into a single weak equation of motion for the combined fluid-particle system. The hydrodynamic stresses acting at the interface are also completely eliminated. For simplicity, in this section we will assume that there is only one particle. The extension to the many-particle case is straightforward.

The solution and variation are required to satisfy the strong form of the constraint of rigid body motion throughout P(t). In the distributed Lagrange multiplier method this constraint is removed from the velocity space and enforced weakly as a side constraint using a distributed Lagrange multiplier term. It was shown in Glowinski, et al. 1999 that the following weak formulation of the problem holds in the extended domain:

For a.e. t>0, find $\mathbf{u} \in \overline{W}_{u\Gamma}$, $p \in L_0^2(\Omega)$, $\lambda \in \Lambda(t)$, $\mathbf{U} \in \mathbf{R}^3$, $\boldsymbol{\omega} \in \mathbf{R}^3$ and $\phi \in W_\phi$, satisfying

$$\int_\Omega \rho\left(\frac{d\mathbf{u}}{dt} - \mathbf{g}\right)\cdot \mathbf{v}d\mathbf{x} - \int_\Omega p\nabla.\mathbf{v}\,d\mathbf{x} + \int_\Omega 2\eta\mathbf{D}[\mathbf{u}]:\mathbf{D}[\mathbf{v}]d\mathbf{x}$$

$$+\left(1-\frac{\rho}{\rho_d}\right)\left(M\left(\frac{d\mathbf{U}}{dt}-\mathbf{g}\right)\cdot\mathbf{V} + I\frac{d\boldsymbol{\omega}}{dt}\xi\right) - \mathbf{F}'.\mathbf{V} - \int_\Omega \gamma\kappa\delta(\phi)\mathbf{n}\cdot\mathbf{v}\,d\mathbf{x} = \left\langle \boldsymbol{\lambda}, \mathbf{v}-(\mathbf{V}+\xi\times\mathbf{r})\right\rangle_{P(t)}$$

$$\text{for all } \mathbf{v} \in \overline{W}_0,\ \mathbf{V} \in \mathbf{R}^3, \text{ and } \xi \in \mathbf{R}^3, \qquad (1)$$

$$\int_\Omega q\nabla.\mathbf{u}\,d\mathbf{x} = 0 \qquad \text{for all } q \in L^2(\Omega), \qquad (2)$$

$$\left\langle \boldsymbol{\mu}, \mathbf{u}-(\mathbf{U}+\omega\times\mathbf{r})\right\rangle_{P(t)} = 0 \qquad \text{for all } \mu \in \Lambda(t), \qquad (3)$$

$$\mathbf{u}|_{t=0} = \mathbf{u}_o \qquad \text{in } \Omega, \qquad (4)$$

$$\int_\Omega \left(\frac{\partial\phi}{\partial t} + \mathbf{u}\ .\nabla\phi\right) g\ d\mathbf{x} = 0 \text{ for all } g \in W_{\phi 0}, \qquad (5)$$

$$\phi|_{t=0} = \phi_0 \qquad \text{in } \Omega.$$

as well as the kinematic equations and the initial conditions for the particle linear and angular velocities. Here **F'** is the additional body force applied to the particles to limit the extent of overlap (see equation (19) in Glowinski, et al. 1999, λ is the distributed Lagrange multiplier,

$$\overline{W}_{u\Gamma} = \{\mathbf{v} \in H^1(\Omega)^3 \mid \mathbf{v} = \mathbf{u}_\Gamma(t) \quad \text{on} \quad \Gamma\},$$

$$\overline{W}_0 = H_0^1(\Omega)^3,$$

$$L_0^2(\Omega) = \{q \in L^2(\Omega) \mid \int_\Omega q\ d\mathbf{x} = 0\},$$

$$W_\phi = \{\phi \in H^1(\Omega) \mid \phi = \phi_0(t) \quad \text{on} \quad \Gamma^-\},$$

$$W_{\phi 0} = \{\phi \in H^1(\Omega) \mid \phi = 0 \quad \text{on} \quad \Gamma^-\},$$

$$L_0^2(\Omega) = \{q \in L^2(\Omega) \mid \textstyle\int_\Omega q \, d\mathbf{x} = 0\}, \tag{6}$$

where Γ^- is the upstream part of Γ and $\Lambda(t)$ is $L^2(P(t))^3$, with $\langle .,. \rangle_{P(t)}$ denoting the L^2 inner product over the particle. In our simulations, since the velocity and μ are in L^2, we will use the following inner product

$$\langle \boldsymbol{\mu}, \mathbf{v} \rangle_{P(t)} = \textstyle\int_{P(t)} (\boldsymbol{\mu}.\mathbf{v}) \, d\mathbf{x}. \tag{7}$$

In order to solve the above problem numerically, we will discretize the domain using a regular tetrahedral mesh T_h for the velocity, where h is the mesh size, and a regular tetrahedral mesh T_{2h} for the pressure. The following finite dimensional spaces are defined for approximating $\overline{W}_{u\Gamma}$, $\overline{W}_0$, $L^2(\Omega)$, $L_0^2(\Omega)$, W_ϕ and $W_{\phi 0}$:

$$W_{u\Gamma,h} = \{\mathbf{v}_h \in C^0(\overline{\Omega})^3 \mid \mathbf{v}_h|_T \in P_1 \times P_1 \times P_1 \text{ for all } T \in T_h, \mathbf{v}_h = \mathbf{u}_{\Gamma,h} \text{ on } \Gamma\},$$

$$W_{0,h} = \{\mathbf{v}_h \in C^0(\overline{\Omega})^3 \mid \mathbf{v}_h|_T \in P_1 \times P_1 \times P_1 \text{ for all } T \in T_h, \mathbf{v}_h = 0 \text{ on } \Gamma\} \quad ,$$

$$L_h^2 = \{q_h \in C^0(\overline{\Omega}) \mid q_h|_T \in P_1 \text{ for all } T \in T_{2h}\},$$

$$L_{0,h}^2 = \{q_h \in L_h^2 \mid \textstyle\int_\Omega q_h \, d\mathbf{x} = 0\},$$

$$W_{\phi,h}^n = \{g_h \in H^1(\Omega) \mid g_h|_T \in P_1 \text{ for all } T \in T_h, g_h = \phi^n \text{ on } \Gamma^-\}$$

$$W_{\phi 0,h} = \{g_h \in H^1(\Omega) \mid g_h|_T \in P_1 \text{ for all } T \in T_h, g_h = 0 \text{ on } \Gamma^-\}$$

$$W_{\phi R,h} = \{g_h \in H^1(\Omega) \mid g_h|_T \in P_1 \text{ for all } T \in T_h, g_h = 0 \text{ on the interface}\}. \tag{8}$$

The particle inner product terms in (1) and (3) are obtained using the discrete L^2 inner product defined in Glowinski, et al. (1999). Specifically, we choose M points, $\mathbf{x}_1, \ldots, \mathbf{x}_M$ that uniformly cover $\overline{P}(t)$, and define

$$\boldsymbol{\Lambda}_h(t) = \left\{ \boldsymbol{\mu}_h \;\middle|\; \boldsymbol{\mu} = \sum_{i=1}^{M} \boldsymbol{\mu}_{h,i} \, \delta(\mathbf{x} - \mathbf{x}_i), \quad \boldsymbol{\mu}_{h,1}, \ldots, \boldsymbol{\mu}_{h,M} \in \mathbf{R}^3 \right\}.$$

Using these finite dimensional spaces, it is straightforward to discretize equations (1) - (5). Notice that the discrete space $W_{\phi,h}$ assumes that ϕ is known on the upstream portion of the boundary. This is not a problem even when $\phi(t)$ is not known on the upstream boundary in advance because the imposed boundary value can be corrected during the reinitialization step. Since only the zero level set of $\phi(t)$ is physically relevant, we have a lot of freedom in treating $\phi(t)$ away from the interface. In our code, the value from the previous time step is used as the boundary value. The reinitialization space $W_{\phi R,h}$ assumes that ϕ remains zero along the interface which is done by imposing Dirichlet boundary condition, $\phi = 0$, along the interface during reinitialization iterations.

A.1 Strong form

The strong form for the weak formulation can be obtained by integrating the stress term by parts. The resulting equations inside the region occupied by the fluid $\Omega\backslash\overline{P(t)}$ are

$$\rho\left[\frac{\partial \mathbf{u}}{\partial t}+\mathbf{u}.\nabla\mathbf{u}\right] = \rho\mathbf{g} - \nabla p + \nabla.\boldsymbol{\sigma} + \gamma\,\kappa\,\delta(\phi)\,\mathbf{n} \qquad \text{in } \Omega\backslash\overline{P(t)}$$

$$\nabla\cdot\mathbf{u} = 0 \qquad \text{in } \Omega\backslash\overline{P(t)}$$

$$\mathbf{u} = \mathbf{u}_L \qquad \text{on } \Gamma_d$$

$$\mathbf{u} = \mathbf{U} + \omega \text{ x } \mathbf{r} \qquad \text{on } \partial P(t)$$

and the equations inside the region occupied by the particles P(t) are

$$\rho\left[\frac{\partial \mathbf{u}}{\partial t}+\mathbf{u}.\nabla\mathbf{u}\right] = \rho\mathbf{g} - \nabla p + \nabla.(2\eta\mathbf{D}) + \boldsymbol{\lambda} - R^2\nabla^2\boldsymbol{\lambda} \tag{9}$$

$$\mathbf{u} = \mathbf{U}_i + \omega_i \text{ x } \mathbf{r}_i \qquad \text{on } \partial P_i(t)\text{, i=1,\ldots,N,}$$

Here we have used the fact that the rigid body motion satisfies the incompressibility constraint and that **D**(**u**) inside the particles is zero. The boundary condition for λ on the interface between the fluid and particle regions $\partial P(t)$ is

$$\mathbf{n}.(-\sigma_L) = \mathbf{n}.\nabla\boldsymbol{\lambda} \tag{10}$$

where **n** is the normal at the fluid-particle interface, and $\sigma_L = \text{-}p\mathbf{I} + 2\eta\mathbf{D}$ is the stress in the fluid phase, and $\sigma_P = 0$ is the stress inside the particles. For given **U**(t) and ω(t), and the positions X_i(t), i=1,…, N, equation (9) can be written as:

$$\boldsymbol{\lambda} - R^2\nabla^2\boldsymbol{\lambda} = \rho_L\left(\frac{d\mathbf{U}}{dt}+\frac{d\omega}{dt}\times\mathbf{r}+\omega\times(\omega\times\mathbf{r})-\mathbf{g}\right) \tag{11}$$

It is shown in Joseph 2002, chapter IV, that it is possible to completely eliminate the Lagrange multiplier λ from the strong form.

A.2 Time discretization using the Marchuk-Yanenko operator splitting scheme

The discretized initial value problem (1-5) is solved by using the Marchuk-Yanenko operator splitting scheme. This allows us to decouple its four primary difficulties:

1. The incompressibility condition and the related unknown pressure p_h,

2. The nonlinear convection term,
3. The rigid body motion problem inside the particles,
4. The interface problem and the related unknown level set distribution ϕ_h,

The Marchuk-Yanenko operator splitting scheme can be applied to an initial value problem of the form

$$\frac{d\phi}{dt} + A_1(\phi) + A_2(\phi) + A_3(\phi) + A_4(\phi) = f$$

where the operators A_1, A_2, A_3, and A_4 can be multiple-valued.

Let Δt be the time step, and α_1 and α_2 be two constants: $0 \le \alpha_1, \alpha_2 \le 1$ and $\alpha_1 + \alpha_2 = 1$. We use the following version of the Marchuk-Yanenko operator splitting to simulate the motion of particles on two-fluid interfaces:

Set $\mathbf{u}^0 = \mathbf{u}_{0,h}$, and $\phi^0 = \phi_{0,h}$.

For n = 0,1,2,… assuming $\mathbf{u}^n$, and ϕ^n are known, find the values for n+1 using the following:

STEP 1:

Find $\mathbf{u}^{n+1/4} \in W_{u,h}$ and $p^{n+1/4} \in L^2_{0,h}$, by solving

$$\int_\Omega \rho \frac{\mathbf{u}^{n+1/4} - \mathbf{u}^n}{\Delta t} . \mathbf{v}\, d\mathbf{x} - \int_\Omega p^{n+1/4} \nabla . \mathbf{v}\, d\mathbf{x} = \int_\Omega \gamma \kappa \delta(\phi) \mathbf{n} \cdot \mathbf{v}\, d\mathbf{x}$$

$$\text{for all } \mathbf{v} \in W_{0,h},$$

$$\int_\Omega q \nabla . \mathbf{u}^{n+1/4} d\mathbf{x} = 0 \qquad \text{for all } q \in L^2_h, \tag{12}$$

STEP 2:

Find $\mathbf{u}^{n+2/4} \in W_{u,h}$, by solving

$$\int_\Omega \rho \frac{\mathbf{u}^{n+2/4} - \mathbf{u}^{n+1/4}}{\Delta t} . \mathbf{v} d\mathbf{x} + \int_\Omega \rho (\mathbf{u}^{n+2/4} . \nabla \mathbf{u}^{n+2/4}) . \mathbf{v}\, d\mathbf{x} + \alpha_1 \int_\Omega 2\eta \mathbf{D}[\mathbf{u}^{n+2/4}] : \mathbf{D}[\mathbf{v}] d\mathbf{x} = 0$$

$$\text{for all } \mathbf{v} \in W_{0,h}, \tag{13}$$

STEP 3:

Compute $\mathbf{U}^{n+3/4}$ and $\mathbf{X}^{n+3/4}$ using the prediction procedure

Set $\mathbf{U}^{n,0}=\mathbf{U}^{n}$, $\mathbf{X}^{n,0}=\mathbf{X}^{n}$.

Do k=1,K

$$\mathbf{U}^{*n,k}=\mathbf{U}^{n,k\text{-}1}+\left(\mathbf{g}+\left(1-\frac{\rho}{\rho_d}\right)^{-1}M^{-1}F'(X^{n,k-1})\right)\frac{\Delta t}{K}$$

$$\mathbf{X}^{*n,k}=\mathbf{X}^{n,k\text{-}1}+\left(\frac{\mathbf{U}^{n,k-1}+\mathbf{U}^{*n,k}}{2}\right)\frac{\Delta t}{K}$$

$$\mathbf{U}^{n,k}=\mathbf{U}^{n,k\text{-}1}+\left(\mathbf{g}+\left(1-\frac{\rho}{\rho_d}\right)^{-1}M^{-1}\frac{F'(X^{n,k-1})+F'(X^{*n,k-1})}{2}\right)\frac{\Delta t}{K}$$

$$\mathbf{X}^{n,k}=\mathbf{X}^{n,k\text{-}1}+\left(\frac{\mathbf{U}^{n,k-1}+\mathbf{U}^{n,k}}{2}\right)\frac{\Delta t}{K}$$

end do

Set $\mathbf{U}^{n+3/4}=\mathbf{U}^{n,K}$, $\mathbf{X}^{n+3/4}=\mathbf{X}^{n,K}$. (14)

Find $\mathbf{u}^{n+1}\in W^{n+1}_{u\Gamma,h}$, $\boldsymbol{\lambda}^{n+1}\in\Lambda_h((n+2/4)\Delta t)$, $\mathbf{U}^{n+1}\in\mathbf{R}^3$, and $\boldsymbol{\omega}^{n+1}\in\mathbf{R}^3$, satisfying

$$\int_\Omega\rho\frac{\mathbf{u}^{n+1}-\mathbf{u}^{n+2/4}}{\Delta t}.\mathbf{v}\,d\mathbf{x}+\left(1-\frac{\rho}{\rho_d}\right)\left(M\frac{\mathbf{U}^{n+1}-\mathbf{U}^{n+3/4}}{\Delta t}.\mathbf{V}+I\frac{\boldsymbol{\omega}^{n+1}-\boldsymbol{\omega}^{n+3/4}}{\Delta t}\xi\right)+$$
$$\gamma\int_\Omega 2\eta\mathbf{D}[\mathbf{u}^{n+1}]:\mathbf{D}[\mathbf{v}]d\mathbf{x}=\left\langle\boldsymbol{\lambda}^{n+1},\mathbf{v}-(\mathbf{V}+\xi\times\mathbf{r}^{n+3/4})\right\rangle_{P((n+3/4)\Delta t)}$$

for all $\mathbf{v}\in W_{0,h}$, $\mathbf{V}\in\mathbf{R}^3$, and $\xi\in\mathbf{R}^3$

$$\left\langle\boldsymbol{\mu}_h,\mathbf{u}^{n+1}-(\mathbf{U}^{n+1}+\boldsymbol{\omega}^{n+1}\times\mathbf{r})\right\rangle_{P((n+3/4)\Delta t)}=0\qquad\text{for all }\boldsymbol{\mu}_h\in\boldsymbol{\Lambda}((n+3/4)\Delta t),\qquad(15)$$

where the center of particle $P((n+3/4)\Delta t)$ is at $X^{n+3/4}$. For a disk the moment of inertia changes as the disk rotates and so we also keep track of its orientation.

Set $\mathbf{X}^{n+1,0}=\mathbf{X}^{n}$.

Do k=1,K

$$\mathbf{X}^{*n+1,k}=\mathbf{X}^{n+1,k\text{-}1}+\left(\frac{\mathbf{U}^{n}+\mathbf{U}^{n+1}}{2}\right)\frac{\Delta t}{K}$$

$$\mathbf{X}^{n,k}=\mathbf{X}^{*n,k\text{-}1}+\left(1-\frac{\rho}{\rho_d}\right)^{-1}M^{-1}\left(\frac{F'(X^{n+1,k-1})+F'(X^{*n+1,k})}{2}\right)\frac{(\Delta t)^2}{2K}$$

end do

Set $\mathbf{X}^{n+1}=\mathbf{X}^{n+1,K}$.

STEP 4:

Find $\phi^{n+4/4} \in W^n_{\phi,h}$, by solving

$$\int_\Omega \left(\frac{\phi^{n+4/4} - \phi^n}{\Delta t} + \mathbf{u}^{n+1}.\nabla\phi^{n+1} \right) g_h d\mathbf{x} \quad = \quad 0$$

$$\text{for all } g_h \in W_{\phi 0,h}. \tag{16}$$

Set $p^{n+1} = p^{n+1/4}$, $\phi^{n+1} = \phi^{n+4/4}$.

STEP 4.1:

Reinitialize $\phi^{\ n+1}$

Set $\phi^0_R = \phi^{n+1}$

For r = 0, 1, 2, …

$$\mathbf{w}^r = S(\phi^{n+1}) \frac{\nabla\phi^r_R}{\left|\nabla\phi^r_R\right|}$$

Find $\phi^{r+1}_R \in W_{\phi R,h}$, by solving

$$\int_\Omega \left(\frac{\phi^{r+1}_R - \phi^r_R}{\Delta t} + \mathbf{w}^r.\nabla\phi^r_R \right) g_h d\mathbf{x} \quad = \int_{\mathbf{\Omega}} S(\phi^{n+1})\, g_h \, d\mathbf{x}$$

$$\text{for all } g_h \in W_{\phi R,h}. \tag{17}$$

go back to the above for loop.

STEP 4.2:

Modify ϕ^{n+1} inside and on the particle surfaces to enforce contact angle

Set $\phi^0_R = \phi^{n+1}$

For r = 0, 1, 2, …

$$\mathbf{u}^r_{ex} = \begin{cases} 0 & \text{outside particles} \\ \mathbf{u}_{ex} \text{ from (12)} & \text{otherwise} \end{cases}$$

Find $\phi^{r+1}_R \in W_{\phi R,h}$, by solving

$$\int_\Omega \left(\frac{\phi_R^{r+1} - \phi_R^r}{\Delta t} + \mathbf{u_{ex}}^r . \nabla \phi_R^r \right) g_h d\mathbf{x} \quad = 0$$

$$\text{for all } g_h \in W_{\phi R,h}. \tag{18}$$

go back to the above for loop.

Set $\phi^{n+1} = \phi_R^{r+1}$ and go back to the first step.

The decoupled sub-problems can be solved much more efficiently than the original problem (1-5). In our code all of these sub-problems are solved using matrix-free algorithms, which reduces the memory required.

Remarks:

1. The first step gives rise to a L^2 projection problem for the velocity and pressure distributions which is solved by using a conjugate gradient method (Glowinski, Tallec, Ravachol and Tsikkinis 1992 and Glowinski, et al. 1999).

2. The second step is a nonlinear problem for the velocity, which is solved by using a least square conjugate gradient algorithm (Glowinski and Pironneau 1992).

3. In this paper, we will assume that $\alpha_1 =1$, $\alpha_2 = 0$.

4. The fourth step is a hyperbolic problem for the scalar level set function ϕ. This problem is solved by using a upwinding scheme where the advection term is discretized using a third order scheme (Glowinski and Pironneau 1992 and Pillapakkam and Singh 2001).

5. After advecting ϕ according to (16), we reinitialize ϕ to be a distance function near the interface by performing one or two iterations of (17) using a fast algorithm developed in Pillaipakkam and Singh 2001. The interface position $\phi(t) = 0$ does not change during these reinitialization iterations. It is necessary to re-initialize ϕ to ensure that the scheme accurately conserves mass.

6. The level set function is extended inside and on the surface of the particles such that the contact angle is 135° by performing one or two iterations of (18).

5. References

1. Bowden, N., I.S. Choi, B.A. Grzybowski, G.M. Whitesides, Mesoscale self-assembly of hexagonal plates using lateral capillary forces: synthesis using the “capillary bond”, *J. Am. Chem. Soc.* **121**, 5373-5391 (1999).

2. Bowden, N., A. Terfort, J. Carbeck, G.M. Whitesides, Self-assembly of mesoscale objects into ordered two-dimensional arrays, Science, **276**, 233-235 (1997).
3. Brenner, H. and L.G. Leal. A micromechanical derivation of Fick's law for interfacial diffusion of surfactant molecules, *J. Colloid Interface Sci.* **65**, 191 (1978).
4. Brenner, H. and L.G. Leal. Conservation and constitutive equations for adsorbed species undergoing surface diffusion and convection at a fluid-fluid interface, *J. Colloid Interface Sci.*, **88**, 136 (1982).
5. Bristeau, M.O., R. Glowinski & J. Periaux. Numerical methods for Navier-Stokes equations. Application to the simulation of compressible and incompressible flows, *Computer Physics Reports,* **6**, 73 (1987).
6. Chan, D.Y.C., J.D. Henry Jr. and L.R. White. The interaction of colloidal particles collected at the fluid interface, *J. Colloid Interface Sci*. **79**, 410 (1981).
7. Danov, K.D., R. Aust, F. Durst and U. Lange. Influence of the surface viscosity on the hydrodynamic resistance and surface diffusivity of a large Brownian particle, *J. Colloid and Interface Science*, **175**, 36-45 (1995).
8. Dussan V., E.B. and S.H. Davis. On the motion of a fluif-fluid interface along a solid surface. *J. Fluid Mech.* **65**, 71 (1974).
9. Dussan V., E.B. The moving contact line: the slip boundary condition. *J. Fluid Mech.* **77**, 665-684 (1976).
10. Fortes, M.A. Attraction and repulsion of floating particles, *Can. J. Chem.* **60,** 2889 (1982).
11. Friedrichs, B. and S.I.Guceri. A novel hybrid numerical technique to model 3-D fountain flow in injection molding processes, *J. Non-Newtonian Fluid Mech.* **49**, 141-173 (1993).
12. Gerson, D.F., Zaijc, J.E. and Ouchi, M.D. Chemistry for energy, Ed. M. Tomlinson, ACS symposium series, 90, American Chemical Society, Washington DC, 66 (1979)
13. Gifford, W.A. and L.E. Scriven. On the attraction of floating particles, *Chem. Engrg. Sci.* **26**, 287-297 (1971).
14. Glowinski, R., T.W. Pan, T.I. Hesla & D.D. Joseph. A distributed Lagrange multiplier/fictitious domain method for particulate flows, *Int. J. Multiphase Flows* **25(5)**, 755 (1999).
15. Glowinski, R. and O. Pironneau. Finite element methods for Navier-Stokes equations, *Annu. Rev. Fluid Mech*. **24**, 167 (1992).
16. Glowinski, R., P. Tallec, M. Ravachol & V. Tsikkinis. Chap. 7 in *Finite Elements in Fluids, Vol 8*, Ed. T.J. Chung, Hemisphere Publishing Corp., Washington DC (1992).
17. Goldman, A.J., R.G. Cox and H. Brenner. Slow viscous motion of a sphere parallel to a plane wall—I Motion through a quiescent fluid, *Chem. Eng. Sci*. **22**, 637-653 (1967).
18. Grzybowski, B.A., N. Bowden, F. Arias, H. Yang, G.M. Whitesides, Modeling of menisci and capillary forces from the millimeter to the micrometer size range, *J. Phys. Chem. B* 105, 404-412. (2001).
19. Hesla, T.I. and D.D. Joseph, The maximum contact angle at the rim of a heavy floating disk, submitted to *J. Colloid and Interface Science (2003).*
20. Hirt, C.W. and B.D. Nichols, Volume of fluid (VOF) methods for the dynamics of free boundaries, *J. Comput. Phys*. **39**, 201 (1981).
21. Joseph, D.D., Interrogations of Direct Numerical Simulation of Solid-Liquid Flows, Web based book: http://www.efluids.com/efluids/books/efluids_books.htm, (2002).
22. Joseph, D.D., J. Wang, R. Bai, B.H. Yang and H.H. Hu, Particle motion in a liquid film rimming the inside of a rotating cylinder. *J. Fluid Mech.*, **496**, 139-163 (2003).
23. Kamal, M.R., S.K. Goyal and E. Chu. Simulation of injection mold filling of viscoelastic polymer with fountain flow, *AIChE Journal*, **34**, 94-106 (1988).

24. Katoh, K., H. Fujita and E. Imazu. Motion of a particle floating on a liquid meniscus surface, *J. Fluids Engrg.*, **114**, 411 (1992).
25. Keller, J.B., Surface tension force on a partly submerged body, *Physics of Fluids*, **10**, 3009-3010 (1998).
26. Kistler, S.F. and L.E. Scriven. The teaplot effect: sheet-forming flows with deflection, wetting and hysteresis, *J. Fluid Mech.* **263**, 19-62 (1994).
27. Kralchevsky, P.A., V.N. Paunov, N.D. Denkov, I.B. Ivanov and K. Nagayama. Energetical and force approaches to the capillary interactions between particles attached to a liquid-fluid interface, *J. Colloid and Interface Sci.* **155**, 420-437 (1993).
28. Kralchevsky, P.A., V.N. Paunov, N.D. Denkov, and K. Nagayama., *J. Colloid and Interface Sci.* **167**, 47 (1994).
29. Kralchevsky, P.A., V.N.Paunov, I.B.Ivanov and K.Nagayama, "Capillary Meniscus Interactions between Colloidal Particles Attached to a Liquid - Fluid Interface", *J. Colloid Interface Sci.* **151** 79 - 94 (1992).
30. Kralchevsky, P. A. and K. Nagayama, "Capillary interactions between particles bound to interfaces, liquid films and biomembranes", Advances in Colloid and Interface Science, **85**, 145-192 (2000).
31. Manon, V.B. and D.T. Wasan. Particle-fluid interactions with application to solid-stabilized emulsions. Part 1, The effect of asphaltene adsorption. *Colloids Surf.* **19**, 89-105 (1986).
32. Marchuk, G.I. Splitting and alternate direction methods. *Handbook of Numerical Analysis*, P.G. Ciarlet and J.L. Lions (Eds.), Volume I, 197-462. Amsterdam: North-Holland (1990).
33. Nicolson, M.M. The interaction between floating particles, *Proc. Cambridge Philosophical Soc.,* **45**, 288 (1949).
34. Osher, S. and J.A. Sethian. Fronts propagating with curvature-dependent speed: Algorithms based on Hamilton-Jacobi formulations, *J. Comput. Phys.* **83**, 12 (1988).
35. Petkov, J.T., N.D Denkov, K.D Danov, O.D. Velev, R. Aust and F Durst. Measurement of the drag coefficient of spherical particles attached to fluid interfaces, *J. Colloid and Interface Science,* **172**, 147-154 (1995).
36. Pillapakkam, S.B. and P. Singh. A Level Set Method for computing solutions to viscoelastic two-phase flow, *J. Computational Physics,* **174**, 552-578 (2001).
37. Poynting, J.H. and J.J. Thompson. *A Text-book of Physics: Vol. 1, Properties of Matter*, C. Griffith & Co. Ltd, London, 153-155 (1913).
38. Princen, H.M. Equilibrium shape of interfaces, drops and bubbles. Rigid and deformable particles at interfaces, *Surface and Colloid Science*, E. Matijevie, ed., Interscience, New York, Vol. 2, p.1 (1969).
39. Rapacchietta A.V. and A.W. Neumann. Force and free-energy analyses of small particles at fluid interfaces: II. Spheres, *J. Colloid and Interface Sci.*, **59**(3), 555-567 (1977).
40. Redoev, B., M. Nedjalkov and V. Djakovich. Brownian motion at liquid-gas interfaces. I. Diffusion coefficients of maroparticles at pure interfaces, *Langmuir,* **8**, 2962 (1992).
41. Ryskin, G. & L.G. Leal. Numerical solution of free-boundary problems in fluid mechanics. Part 1: The finite-difference technique, *J. Fluid Mech*. **148**, 1 (1984).
42. Saif, T.A. On the capillary interaction between solid plates forming menisci on the surface of a liquid, J. Fluid Mech., **453**, 321-347 (2002).
43. Scardovelli, R. and Zaleski, S., Direct Simulation of Free-surface and interfacial flow, *Annu. Re. Of Fluid Mech.* 1999 **31**: 567-603.
44. Schneider, Y.C., M.E. O'Neill, and H. Brenner. On the slow viscous rotation of a body straddling the interface between two immiscible semi-infinite fluids, *Mathematika,* **20**, 175 (1973).

45. Singh, P. and T.I. Hesla, Torque due to interfacial tension on a floating sphere, http://web.njit.edu/~singhp/ research/publication.html (2003).
46. Singh, P., T.I. Hesla and D.D. Joseph, A Modified Distributed Lagrange Multiplier/Fictitious Domain Method for Particulate Flows with Collisions, *Int. J. of Multiphase Flows,* **29**, 495-509 (2003).
47. Singh, P., D.D. Joseph, T.I. Hesla, R. Glowinski & T.W. Pan. A distributed Lagrange multiplier/fictitious domain method for viscoelastic particulate flows, *J. Non-Newtonian Fluid Mech.* **91**, 165 (2000).
48. Singh, P. and L.G. Leal. Finite element simulation of the start-up problem for a viscoelastic problem in an eccentric cylinder geometry using third-order upwind scheme, *Theoret. Comput. Fluid Dynamics*, **5,** 107-137 (1993).
49. Sussman, M. An Adaptive Mesh Algorithm for Free Surface Flows in General Geometries, Adaptive Method of lines, Editors, A. Vande Wouwer, Ph. Saucez and W.E. Scheisser, Chapman and Hall/CRC, 207-227 (2001).
50. Sussman, M., P. Smereka & S. Osher. A level set approach for computing solutions to incompressible two-phase flow, *J. Comput. Phys.* **114**, 146 (1994).
51. Unverdi, S.O. & G. Tryggvason. A front-tracking method for viscous, incompressible, multi-fluid flows, *J. Comput. Phys.* **100**, 25 (1992).
52. Wakiya, S. Niigata Univ. College of Engng. Res. Rept. 6, Nagoaka, Japan (March 30, 1957).
53. Wang, J., R. Bai, and D.D. Joseph, to be submitted (2004).
54. Yan N. and J.H. Masliyah. Absorption and desorption of clay particles at the oil-water interface. *J. Colloid and Interface Science*, **168**, 386-392 (1994).